UNIVERSITY OF CALIFORNIA,

IRVINE

Experimental and Numerical Studies of Seismic Soil Pressures on Non-rigid Subsurface Structures

DISSERTATION

submitted in partial satisfaction of the requirements

for the degree of

DOCTOR OF PHILOSOPHY

in Civil Engineering

by

Lohrasb Keykhosropour

Dissertation Committee:

Associate Professor Anne Lemnitzer, Chair

Associate Professor Farzin Zareian

Professor Scott J. Brandenberg

2019

DEDICATION

to

my wife, Shirin, for her continuous support and patience

and

my beloved parents and family

Table of Contents

List of Figures

List of Tables

Acknowledgments

I am sincerely and extremely grateful to my doctoral advisor, Professor Anne Lemnitzer, for her invaluable guidance and support throughout the course of my studies and for providing me the opportunity to pursue the research presented in this dissertation. It has been an honor and a pleasure to work under her mentorship.

I would also like to thank my committee members, Professor Scott Brandenberg and Professor Farzin Zareian for their invested time and excellent advice and suggestions.

Dr. Eric Ahlberg, Dr. Sergio Carnalla, and Professor Lisa Star are gratefully acknowledged for their helps regarding pressure cell calibrations and their valuable technical advice.

Importantly, I was extremely fortunate to have the friendship and support of a number of fellow Ph.D. students such as Luis Herrera, Camilla Favaretti, Rabie Farrag, Susana Anacleto, Siavash Zare, Ali Morshedifard, and Jawad Fayaz. I thank all of them for listening, offering me advice, and for supporting me through this period.

Nobody has been more important to me in the pursuit of this project than the members of my family. I would like to thank my parents, who have sacrificed much to make sure that I follow my dreams and I owe everything that I have ever done and will ever do. Most importantly, I want to thank my loving and supportive wife, Shirin, who has been with me every step of this way. Her strength and love made me strong and her trust in my abilities supported me through difficult times. This work wouldn't have been possible without her.

Curriculum Vitae

Lohrasb Keykhosropour

2007	B.S. in Civil Engineering, Isfahan University of Technology, Isfahan, Iran
2011	M.S. in Geotechnical Engineering, Amirkabir University of Technology, Tehran, Iran
2015-19	Research and Teaching Assistant, University of California, Irvine, CA
2019	Ph.D. in Geotechnical Engineering, University of California, Irvine, CA Dissertation: "Experimental and Numerical Studies of Seismic Soil Pressures on Non-rigid Subsurface Structures" Professor Anne Lemnitzer, Chair

PUBLICATIONS

Journal Papers

Keykhosropour, L., and Lemnitzer, A. (2019). "Experimental Studies of Seismic Soil Pressures on Vertical Flexible, Underground Structures and Analytical Comparisons." *Soil Dynamics and Earthquake Engineering*, Vol. 118, 166-178.

Keykhosropour, L., Lemnitzer, A., Star, L., Marinucci, A., Keowen, S. (2019). "Closure to discussion of implementation of soil pressure sensors in large-scale soil structure interaction studies." *ASTM Geotechnical Testing Journal*, Vol. 42, No. 5.

Keykhosropour, L., Lemnitzer, A., Star, L., Marinucci, A., Keowen, S. (2018). "Implementation of Soil Pressure Sensors in Large-scale Soil Structure Interaction Studies." *ASTM Geotechnical Testing Journal*, Vol. 41, No. 4, 730-746.

Lemnitzer, A., Keykhosropour, L., Kawamata, Y., and Towhata, I. (2017). "Dynamic Response of Underground Structures in Sand: Experimental Data." *Earthquake Spectra*, Vol. 33, No. 1, 347-372.

Keykhosropour, L., Soroush, A., and Imam, R. (2012). "3D Numerical Analyses of Geosynthetic Encased Stone Columns." *Geotextiles and Geomembranes*, Vol. 35, 61-68.

Conference Papers

Keykhosropour, L., Lemnitzer, A. (2018). "Comparison of Measurements and Limit State Solutions for Soil Pressures on Deep Flexible Underground Structures." *International Foundation Congress and Equipment Expo*, Orlando, Florida.

Lemnitzer, A., Keykhosropour, L., Marinucci, A., and Keowen, S. (2018). "Large Diameter Soil

Pressure Sensors: Design, Development and Sample Application." *International Foundation Congress and Equipment Expo*, Orlando, Florida.

Lemnitzer, A., Keykhosropour, L. (2018). "Experimental Study of Seismic Soil Pressures on Vertical Flexible Hollow Shafts." *5th Geotechnical Earthquake Engineering and Soil Dynamics Conference*, Austin, Texas.

Lemnitzer, A., Star, L., Keykhosropour, L., Marinucci, A., and Keowen, S. (2018). "Large Diameter Pressure Sensors Employed in Dynamic Shallow Foundation Testing." *Geoshanghai International Conference*, Shanghai, China.

Keykhosropour, L., Soroush, A., Imam, R. (2011). "A Study on the Behavior of a Geosynthetic Encased Stone Column Group Using 3D Numerical Analyses." *Pan-Am CGS Geotechnical Conference*, Toronto, Canada.

Abstract of the Dissertation

Experimental and Numerical Studies of Seismic Soil Pressures on Non-rigid Subsurface Structures

by

Lohrasb Keykhosropour

Doctor of Philosophy in Civil Engineering

University of California, Irvine, 2019

Professor Anne Lemnitzer, Chair

Reliable seismic design of earth retention structures and substructure components necessitates the accurate evaluation of magnitude and distribution of earthquake induced soil pressures. Many experimental, analytical, and numerical studies have been conducted to further our understanding of the complex of the soil-structure interaction (SSI) between an underground component and its surrounding soil, hereby considering the wide range of assumptions inherent to soil and structural properties (e.g., structural stiffness, embedment depth, and nonlinear behavior of the soil material). This thesis research aims to further our understanding of the distribution and magnitude of seismic soil pressures induced on sub-surface structures through a combination of experimental, analytical, and numerical studies.

Large-scale shake table tests performed on underground structures at the E-Defense facility in Miki, Japan serve as experimental platform for this research. A densely instrumented system of

large-scale underground structures consisting of two vertical shafts, connected through a cut-and-cover tunnel, and two independent shield tunnels was installed in an 8 m-diameter laminar soil box. The system was subjected to step-sine sweeps and scaled ground motion records of the Kobe (1995) earthquake. The underground structures were embedded in a two-layer soil system. The specimen instrumentation consisted of over 800 sensors, including strain gauges, accelerometers, displacement transducers, bender elements, and pressure sensors. Experimental results, including a dynamic system characterization, site response analyses, pressure time histories, and seismic pressure distribution profiles provided critical benchmark data for the subsequent analytical and numerical sections of this research.

Dynamic soil pressure measurements along the vertical shafts served as reference data to examine the suitability of different analytical methods proposed in literature, such as traditional and recently developed limit-state and elastic approaches for both, cohesionless and cohesive (c-φ) soils, in predicting the seismically induced earth pressures on flexible underground structures. Comparative results suggest that, despite the unique shaft geometry, analytical methods accounting for the structural flexibility were able to closely predict the experimental soil pressures, while methodologies derived for rigid subsurface elements can only serve as rough preliminary estimate and should not be employed in performance-based geotechnical analyses. Moreover, none of the analytical solutions included in this thesis work consider the 3D effects of the system, the nonlinear soil-structure interaction, or elastic-plastic behavior of the soil material. These aspects might not be controlling parameters for the behavior of shallow embedded structures, however, their influence becomes significant for deep non-rigid underground structures and should be taken into account.

Results obtained from the shake-table experiments were then used to calibrate a three-dimensional, nonlinear, finite element (FE) model built in ABAQUS. Good agreement was observed between the computed results and experimental data which deemed the reliability of the FE model suitable for the subsequent parametric investigation. By preserving the configuration of the original test system, a selected set of parametric studies was performed, which focused on the (1) the effects of the soil parameters (i.e., cohesion, and friction angle) and (2) the structural flexibility/ stiffness of the subsurface elements.

In the last section of this research, a simplified 3D soil-structure model was developed and influences of the most important parameters on the seismic soil pressures, including the retained soil mechanical parameters, structure and its base flexibilities, amplitude of the ground motion's acceleration, and geometry of the wall were examined through an extensive set of parametric studies. Results of these parametric studies, including the seismic soil pressure distribution and variations of seismic forces and their corresponding moments against each of the studied parameters were presented as normalized graphs and tables, which could be used in the preliminary analysis and design stage of deep embedded structures.

Chapter 1

Introduction and background

1.1. Introduction

The accurate prediction of the magnitude and distribution of seismic soil pressures is critical to the proper design of the earth retaining and substructure components. The complexity of the dynamic soil-structure interaction, nonlinear behavior of the soil material and different structural properties (e.g., flexural stiffness, torsional rigidity, degrees of freedom) result in significant uncertainty in the prediction of seismically induced soil pressures and have sparked a widespread research interest in this field. The dynamic behavior of earth retaining structures in terms of seismic soil pressures has been the subject of numerous analytical, experimental and numerical studies (e.g., Okabe, 1924, Mononobe and Matsuo, 1929, Kapila 1962, Prakash and Basavanna 1968, Seed and Whitman 1970, Wood 1973, Steedman and Zeng 1990, and Veletsos and Younan 1997). Moreover, with the fast development of cities and reduction of above-ground real estate, underground structures such as tunnels, culverts, and, vertical shafts have become key elements of urban infrastructure. The design and analysis of these structures have received increasing research interest over the past decade (e.g., Moss and Crosariol 2013, Tsinidis et al. 2016, Hushmand et al. 2016), which in turn resulted in the development of several analytical methods for prediction of seismic soil pressures. Simultaneously, advancements in testing and instrumentation have improved the accuracy of analytical methods. However, even state-of-the-art models provide solutions for idealized conditions, (e.g., perfectly plastic or visco-elastic soil material, full rigid structures) and depending on their initial assumptions, different methods may produce

contradicting results for each specific problem. As a result, there remains a lack of general consensus in designing the above-mentioned structures for seismic loading demands. Furthermore, a large majority of the existing analytical models fall short in considering important factors which are believed to affect the distribution and magnitude of seismic soil pressures. These are, for example, 3D effects, nonlinear behavior of the retaining soil, flexibility of the structure relative to the retained soil, and stiffness of the layer overlain by the structure. These aspects, when ignored, might not be controlling parameters for the design of shallow embedded structures, however their influence can become significant for deep underground structures and should be taken into account.

The remainder of this chapter provides a detailed state of the art review of experimental, analytical, and numerical methodologies found in literature and utilized for the assessment of the magnitude and distribution of lateral seismic soil pressures on retaining structures. The scope and objectives of this study, concludes the chapter.

1.2. Experimental studies

Investigation of seismic soil pressures on retaining walls and underground structures has been the subject of many experimental studies. These experimental studies are divided into two main groups: shake table tests and scaled centrifuge models. Compared to shake table tests, dynamic centrifuge experiments are relatively recent and less common. Numerous shake table tests have been performed during the past decades to study the behavior of retaining structures in terms of seismic soil pressures. Mononobe and Matsuo (1929) were the first researchers who studied this issue through shake table tests. Results of their experiments along with the analytical work by

Okabe (1924) led to the development of the well-known Mononobe-Okabe method, M-O, (Equations 1 and 2).

In 1939, Jacobson performed a series of shake table tests on a 3 ft high wall with dry sand backfill subjected to harmonic motions. The maximum pressures magnitudes measured in Jacobson's experiments were in good agreement with the M-O method for accelerations up to 0.4g, but contrary to the M-O method, Jacobson found the location of the resultant of dynamic soil pressures acting at the 2/3 of the wall's height above its base. The same result was also observed by Matsuo, (1941). Later in 1960, by using a shake table about 4 m (13 ft) long, 2.1 m (7 ft) wide and 0.6 m (2 ft) deep, Ishii, Arai and, Tsuchida did a comprehensive investigation of lateral seismic soil pressures. Ishii et al. concluded that the magnitude of the maximum seismic pressures was almost equal to the computed values by the M-O method, but suggested the location of the resultant force to be between 0.33h to 0.4H above the base of the wall, where H is the height of the wall. Another important conclusion of their work was that the residual stresses remaining after stopping the motions were higher compared to the initial static stresses. Murphy (1960), Niwa (1960), Ohara (1960), Kurata, Arai and, Yokoi (1965) were other researchers who performed shake table tests on small-scale retaining structures and obtained results in agreement with the theoretical predictions (i.e., M-O method).

Nandkumaran (1973) performed a set of shake table tests on rigid and flexible walls (1 m high flexible wall, 1 m and 2 m high rigid walls) which were later reported by Prakash and Nandkumaran (1979). Based on this study, the horizontal seismic coefficient, k_h, was recommended to be: $k_h = \frac{V_{max} \cdot 2\pi}{g}$, in which V_{max} is the peak ground velocity, f is the frequency corresponding to an arbitrarily selected period of the ground motion to match the experimental results, and g is the gravity. It was also suggested that the point of application of the resultant of

dynamic soil pressures is at 0.55H above the base for flexible walls and 0.45H for rigid walls. Other 1-g shake table tests which were performed later (e.g., Bolton and Steedman 1982, Sherif et al. 1982, Klapperich 1983, Sherif and Fang 1984, and Ishibashi and Fang 1987) also led to the results in agreement with the M-O method. A full list of these studies and their results could be found in Whitman (1991).

Shake table tests have a number of limitations such as difficulties in scaling of stiffnesses and stresses under 1-g conditions. However, the most critical problem pertaining to shake table testing are boundary conditions, which for instance, at the base of the shake table can only simulate the condition of the rigid bedrock (i.e., underground structures located on a compliant layer cannot be modeled). Therefore, as an alternative, centrifuge model experiments were also used by some investigators to study the distribution and magnitude of seismically induced soil pressures on retaining walls and embedded structures. Dynamic centrifuge tests performed on cantilever walls by Steedman (1984), and Bolton and Steedman (1985) could be named. Later in 1996, Stadler performed centrifuge tests on cantilever walls backfilled with dry medium dense sand and observed that the total dynamic soil pressure profile to be generally triangular but the distribution of the dynamic pressure increment to vary between triangular and rectangular shapes. Dewoolkar et al. (2001), performed a series of centrifuge tests on fixed-end cantilever walls supporting saturated liquefiable sand and investigated the effects of the base motion magnitude and wall flexural stiffness on the seismic soil pressures through parametric studies. Dewoolkar et al. (2001) concluded that excess pore pressure generation in the backfill contributes significantly to lateral seismic pressures but the wall stiffness does not influence the seismic soil pressures. It was also observed that the distribution of dynamic soil pressures varied from triangular to inverted

triangular and line of action of the resultant dynamic force oscillated between 0.6H to 0.8H from the top of the wall (~0.3H from the base).

Nakamura (2006) conducted a set of centrifuge tests on gravity retaining walls and concluded that the M-O method does not properly express the real behavior of the gravity walls during earthquakes. According to the results of this study, part of the backfill which follows the displacement of the wall, deforms plastically and does not remain rigid; secondly, there is a phase difference between the motion of the wall and the backfill which is opposite of the assumption of the M-O method; finally, the distribution of dynamic pressures behind the wall is not triangular and varies with time. Al-Atik and Sitar (2010), performed dynamic centrifuge tests and evaluated the magnitude and distribution of seismic earth pressures on open channel structures with stiff and flexible cantilever walls and a rigid base placed in a dry medium dense sand. Al-Atik and Sitar (2010) concluded that dynamic earth pressures increase linearly with depth and can be approximated by a triangular distribution. The resultant dynamic force was observed at H/3 above from the base of the wall. The authors suggested the M-O method to overestimate the dynamic earth pressures and concluded that seismic earth pressures on cantilever retaining walls can be ignored at accelerations below 0.4g.

Graili Mikola and Sitar (2013) conducted similar centrifuge tests to Al-Atik and Sitar (2010) on three different types of retaining structures in cohesionless soils: (1) a cross-braced (basement) structure (flexible and rigid), (2) a stiff non-displacing U-shaped cantilever wall, and (3) a flexible free-standing cantilever wall. They concluded that dynamic earth pressures increase with depth and the resultant force acts near 0.33H from the base. According to their findings, the Seed and Whitman method, S-W, produced a reasonable upper bound for the value of seismic soil pressures for non-displacing structures but obtained seismic soil pressures were significantly smaller than

those predicted by this method for the free-standing wall. It should be noted that due to the performance characteristics of the utilized tactile pressure sensors in their experiments, the dynamic soil pressures could not be captured at high frequencies of the applied motions and were approximated using the strain gages installed on the walls.

Using shake table tests, Wilson and Elgamal (2015) investigated the influence of soil cohesion and wall movements on the magnitude and distribution of seismic earth pressures. The authors conducted ten shake table tests with different base acceleration magnitudes (0.13g to 1.20g) on a short (1.7 m) reinforced concrete cantilever wall retaining a dense sand backfill with 7% silt (c-φ soil). Wilson and Elgamal (2015) concluded that for motions with peak accelerations less than the yield acceleration (i.e., the lateral acceleration which leads to the factor of safety, FS, of 1 against failure for the vertical backfill without any supporting wall), the backfill has sufficient strength to prevent the formation of an active failure wedge and the resultant dynamic force is zero. However, for accelerations beyond the yield value, wall movements are sufficient to provide the active state and recorded peak dynamic forces are bounded between limit-equilibrium predictions using the peak and residual backfill soil strength parameters (i.e., cohesion and friction angle). It was also observed that limit-equilibrium methods which ignore the backfill cohesion significantly over-predict the soil pressures.

Wagner and Sitar (2016) executed a set of centrifuge tests on a very stiff braced deep wall (13.3m deep, founded on 5.5m of medium dense sand in prototype dimensions). Pressure sensors were installed for the measurement of dynamic soil pressures, but due to the inability of the utilized pressure sensors in providing reliable absolute values, three rows of load cells installed on the braces were used to measure the dynamic earth pressures. According to Wagner and Sitar (2016) results, for this type of underground structures, seismic earth pressures increase from the ground

surface to a depth of 0.3H and then decrease to a small fraction of the corresponding static pressure at each depth. Moreover, it was concluded that M-O and S-W methods provide a reasonable upper bound prediction for seismic loads on retaining structures.

Hushmand et al. (2016) reported the results of a series of dynamic centrifuge tests on underground reservoir structures embedded in medium dense, dry sand which were categorized by the researchers as stiff-unyielding structures. The main conclusions of this study with respect to the seismic pressures were: a) distribution of lateral seismic soil pressures depends on the flexibility of the structure, b) more flexible structures experience a triangular shaped distribution similar to the M-O method while stiffer structures undergo under higher order polynomial pressure distribution, c) dynamic earth pressure coefficients, ΔK_{AE} are close to or smaller than those suggested by the S-W method for flexible structures but are higher than S-W values for stiffer walls, and d) the estimated point of application of the resultant dynamic increment for stiff structures is close to the M-O predictions and generally falls between those predicted by M-O, S-W, and Wood (1973) methods.

1.3. Detailed review of analytical methods

Two core analysis approaches are often used to assess the magnitude and distribution of lateral seismic soil pressures on retaining systems: limit-state methods and elastic solutions. For structures differing from retaining systems, it is also possible to evaluate the response behavior via spring formulations, borrowing from principles of soil-structure interaction of pile foundations. FEMA 750 (2009), classifies the retaining structures based on their relative movement to the soil into two groups: “yielding” and “non-yielding”. If the movement of the tip of the retaining structure –either rigid or flexible- exceeds 0.002 times the structure height, the condition for the development of

minimum active pressures is provided and the wall is called yielding; non-yielding walls do not satisfy this criterion. Despite widely recognized limitations, limit-state methods, typically known through the famous Mononobe-Okabe approach (Mononobe and Matsuo 1929, and Okabe 1924) and its modified version by Seed-Whitman (Seed and Whitman, 1970), remain the most commonly employed methods for the analysis of seismic soil pressures on a variety of underground and retaining systems (i.e., yielding retaining structures) in geotechnical practice to date. Elastic-based methods provide an alternative to limit-state methods and are predominantly used for the analysis of rigid systems, where no rotation or deflection is expected (i.e., non-yielding retaining structures). A detailed review of limit-state methods and elastic solutions is provided to familiarize the reader with the fundamental assumptions inherent to the two analysis categories. Both approaches will then be used for consecutive comparative experimental-analytical studies.

1.3.1. Limit-state methods for cohesionless soils

The limit-state approach uses a pseudo-static analysis and considers the soil to be perfectly plastic. Solutions of the problem are categorized into two groups: stress solutions and kinematic solutions (Mylonakis et al., 2007). The stress solutions, which are based on classical Rankine equations, utilize the stress state to satisfy the field equations of equilibrium and boundary conditions and comply with a predefined failure criterion, i.e., Mohr-Coulomb. The stress solution for cohesionless soils in seismic conditions was only implemented by Mylonakis et al. (2007).

Coulomb's theory (Coulomb, 1776) for calculating static lateral earth pressures is the basis of the kinematic solution. Mononobe and Matsuo (1929) and Okabe (1924), where the first researchers who translated Coulomb's original formulations into an approach suitable for determining dynamic lateral earth pressures on retaining structures. In this approach, the earthquake loading is applied to the soil through pseudo-static horizontal $k_h g$ and vertical $k_v g$

accelerations, where k_h and k_v are the horizontal and vertical seismic earth pressure coefficients, respectively, and g is the gravitational acceleration ($9.81\ m/s^2$). The total seismic active thrust, P_{AE}, which includes both static and seismic force increments is calculated based on the Coulomb wedge theory and is equal to:

$$P_{AE} = 0.5\gamma H^2(1 - k_v)K_{AE} \quad (1)$$

where

$$K_{AE} = \frac{\cos^2(\varphi - \theta - \beta)}{\cos\theta\cos^2\beta\cos(\delta + \beta + \theta)\left[1 + \sqrt{\frac{\sin(\varphi + \delta)\sin(\varphi - \theta - i)}{\cos(\delta + \beta + \theta)\cos(i - \beta)}}\right]^2} \quad (2)$$

In the above equation, γ is the unit weight of the soil, H is the height of the wall, ϕ is the soil friction angle, δ is the angle of wall friction, i is the slope of ground surface behind the wall, β is slope of the back of the wall to vertical, and $\theta = \tan^{-1}\left(\frac{k_h}{1 - k_v}\right)$. The M-O method does not provide the distribution of seismic stresses and similar to Coulomb, it is only intended to estimate the total (resulting) seismic force acting on the wall. Mononobe and Okabe suggested the location of P_{AE} to be at the same position as the static active force, i.e., at $H/3$ from the base of the wall. A limiting problem with the M-O method is Eq. 2, which does not converge in cases when $\theta < \phi - \beta$. For common soil friction angles, (i.e., $\phi \geq 35°$), this issue becomes problematic when accelerations exceed $0.7g$ (Sitar et al., 2012). Kapila (1962) used the same general approach as Mononobe and Okabe and proposed a set of similar equations for the passive seismic force on the structure.

Shortly after, Prakash and Basavanna (1968) conducted theoretical analyses of walls under seismic motions and proposed the location of the resultant force to be at a distance h_a from the base of the wall, where $h_a = C_{ha} \times H/3$. C_{ha} is a constant bigger than 1 and is dependent on k_h.

After analyzing a variety of shake table experiments and conducting accompanying parametric studies, Seed and Whitman (1970) suggested that the increase of lateral pressure due to the base excitation is higher near the top of the wall and the resultant seismic increment acts between $0.5H$ to $0.67H$ above the base. Based on this conclusion, and in order to solve the convergence problem of Eq. 2, Seed and Whitman modified the M-O method by separating the total force into static, P_A, and dynamic, $\Delta P_{AE} = 1/2\gamma H^2 \Delta K_{AE}$, components, where $\Delta K_{AE} \sim \frac{3}{4} k_h$ for horizontal backfills with angle of friction equal to about 35°. Seed and Whitman also introduced the term "inverted triangle' to characterize the distribution of dynamic pressures by recommending that the resultant of the dynamic increment be applied at $0.6H$ from the base of the wall. Due to the short duration of the peak acceleration and its insufficient effect to cause significant wall movements, Seed and Whitman suggested the use of 85% of the peak seismic acceleration when designing retaining walls; however this recommendation was opposed by NEHRP (FEMA 750, 2009).

Based on the results of a series of centrifuge tests, Steedman and Zeng (1990) developed a simple pseudo-dynamic method which considers the shear wave velocity of the backfill and frequency of the applied motion. The magnitude of the total earth pressure is similar to M-O, but the point of application of the dynamic thrust is higher than $H/3$ above the base, and depends on the motion's frequency, and soil properties (Steedman and Zeng, 1990).

Mylonakis et al. (2007) developed a closed-form stress solution for gravitational and seismic induced earth pressures on retaining walls with cohesionless backfills for both active and passive conditions. The authors divided the backfill into two regions with different stress fields; one region

close to the soil surface and the second one close to the wall. In both conditions, the soil is assumed to resist against yielding (Mohr-Coulomb criterion) under combined action of gravity and seismic forces. Wall-soil interface friction is neglected. Resultant lateral forces in static and dynamic cases are treated separately and the dynamic force increment is determined as their difference. This approach is mathematically correct but its physical meaning is limited because the stress fields and their corresponding failure surfaces are different in gravitational and seismic problems. The lateral earth pressure distribution is assumed to be linear, and in absence of a surcharge load, the point of application of the resultant force is located at $H/3$ above the base. The contribution of the vertical seismic acceleration is neglected.

1.3.2. Limit-state methods for cohesive soils

Forty years after the M-O method was introduced, Prakash and Saran (1966) and Saran and Parakash (1968) developed a general solution for seismic pressures on retaining walls supporting $c-\varphi$ soils. In their method, the vertical component of the earthquake acceleration was ignored. Consecutive studies by Richards and Shi (1994) proposed a solution to predict seismic stresses in the free field due to inertial forces. This solution included both, horizontal and vertical accelerations, and is applicable to homogenous backfills of Coulomb-type material. Normal and shear surface tractions are considered and the general framework is applicable to both active and passive cases. The equations can be extended to compute lateral seismic stresses on retaining walls. The Coulomb method was further extended by Saran and Gupta (2003), Ghosh and Saran (2007), and Ghosh et al. (2008) to analyze $c-\varphi$ soils. In all of the above methods, the adhesion between the wall and the soil, c_a, was considered equal to the backfill cohesion. Shukla et al. (2009) advanced the M-O concept for $c-\varphi$ soils in a way to get a single critical failure wedge surface, disregarding friction and adhesion between the wall and the retaining backfill. Shukla and Bathurst

(2012) later presented an analytical expression to calculate the dynamic active thrust from $c-\varphi$ soils while considering all influencing factors including tension cracks in the backfill, surcharge at the backfill surface, horizontal and vertical seismic acceleration components, and wall adhesion and friction. The dynamic active thrust P_{AE} is computed by solving the force equilibrium around the failure wedge. The maximum dynamic resultant force acts on the critical failure wedge at an inclination of α_c and can be found through $\frac{\partial P_{AE}}{\partial \alpha}=0$. Since this method uses the kinematic solution, the distribution of lateral soil pressures cannot be obtained directly and earth pressures are assumed to distribute linearly across the wall height, with the resultant force located at $H/3$ from the base of the wall.

In 2013, Iskander et al. extended the classic Rankine solution to predict seismic active earth pressures behind inclined rigid walls supporting sloped $c-\varphi$ backfills. The effect of the inertial forces is accounted for by altering the static gravity acceleration. This method accounts for the wall inclination and backfill slope, and contrary to kinematic solutions (e.g., Prakash and Saran 1966, Shukla 2012), is capable of providing the distribution of lateral seismic stresses behind the wall as well as the tension crack length. However, this method ignores the soil-wall adhesion and assumes that the stress state adjacent to the wall is the same as the free field. The soil-wall friction angle is simply computed based on the equilibrium of soil elements near the wall, which according to Iskander et al. (2013) yields erroneous results, but is ignored by the authors for simplicity. Shamsabadi et al. (2013) proposed a Log-Spiral-Rankine (LSR) model with a composite failure surface including a logarithmic spiral curve and a linear section (Rankine) to evaluate active and passive seismic soil pressures in $c-\varphi$ soils. The geometry of the curvilinear failure surface was obtained based on three different stress states in two different zones: the logarithmic spiral region and the Rankine zone. In 2015, Xu et al. improved the aforementioned model. According to

independent studies by the authors of this manuscript, Xu et al. method is only suitable for analyzing problems with maximum horizontal acceleration of $k_h = 0.3535$ g.

1.3.3. Elastic-based methods

Elastic-based methods model the soil as a visco-elastic continuum and utilize the theory of elasticity to analyze seismic soil pressures on yielding and non-yielding walls. Proper boundary conditions are considered to model the interaction of the soil and the wall. Early studies by Matsuo and O-hara (1960) proposed an approximate solution for predicting seismic soil pressures on a rigid wall retaining a semi-infinite soil medium excited by harmonic dynamic base motions. Shortly after, Scott (1973) used a simple 1-D model consisting of a shear beam connected to the wall through Winkler springs to evaluate the dynamic response of semi-infinite and bounded backfills. This method was later shown to be inaccurate by Veletsos and Younan (1994). At the same time, Wood (1973) derived an exact solution for non-yielding rigid walls retaining soil backfills with finite length by analyzing an elastic soil layer in a container with rigid walls and rigid base subjected to harmonic base motions. Due to the complexity of this method and its inherent limitations for general use in engineering practice, Wood provided an approximate static solution to predict the maximum seismic thrust on non-yielding rigid walls. The solution was formulated based on harmonic motions with negligible dynamic amplification effects in the system. Wood (1973) showed that motions with frequency ratios $\Omega = f/f_s$ of less than 0.5, have negligible dynamic amplification effects (where f is the frequency of the motion and f_s is the fundamental frequency of the backfill). This method is still widely used in practice and recommended by FEMA 750 (2009). About twenty years later, Veletsos and Younan (1994) provided a solution for rigid walls with semi-infinite soil backfills that considers the rotation of the rigid wall. Shortly after, Veletsos and Younan (1997) included the effect of wall flexibility in

their analysis and proved that neglecting this parameter results in unrealistic high seismic soil pressures. Veletsos and Younan (1997) consider the soil material to be a uniform, infinitely extending, visco-elastic layer. Structural parameters included in this solution are the wall's thickness t_w, mass per unit of surface area μ_w, structural modulus of elasticity E_w, Poisson's ratio ν_w, and material damping ratio ζ. The method assumes that no vertical stresses develop in the soil medium when shaken horizontally, and complete bonding exists between the wall and the soil. The parameters which control the seismic response of the wall are the relative flexibility of the wall and retained backfill d_w, and the relative flexibility of the rotational base constraint and retained soil d_θ according to Eq. 3 – 5:

$$d_w = \frac{GH^3}{D_w} \quad (3),$$ where D_w is the flexural rigidity per unit length of the wall:

$$D_w = \frac{E_w t_w^3}{12(1-\nu_w^2)} \quad (4)$$

$$d_\theta = \frac{GH^2}{R_\theta} \quad (5)$$

Veletsos and Younan presented their solution for excitations with very small dominant frequencies compared to the fundamental frequency of the soil-wall system (pseudo-static case). The dynamic response of the system due to harmonic or transient excitations is obtained by multiplying the pseudo-static response with an amplification or de-amplification factor. Accordingly, for the low-natural periods and stiff strata, the amplification factor is unity in transient motions. In 1999, Wu and Finn provided design charts for seismic thrusts against rigid walls under earthquake excitations for uniform and non-uniform soil backfills. In their numerical

analyses three soil profiles were inherently studied by modeling a uniform, linear and parabolic variation of the shear modulus G with depth.

In 2004, Ostadan suggested the dynamic characteristics of the dynamic earth pressure magnitudes for partially embedded structures (e.g., basement walls) to be similar to those of a single-degree-of-freedom (SDOF) system. Based on this assumption, Ostadan (2004) proposed a method for estimating the magnitude and distribution of dynamic earth pressures on non-yielding building walls, resting on firm foundations. This assumption eliminates the rocking motion of the wall. The input motion is modeled as vertical propagating shear waves and the frequency content of the design motion is included in the analysis. The shape of the soil pressure distribution is assumed to be independent of the input motion's dynamic characteristics and is provided through a normalized 5^{th} degree polynomial function.

In order to explain and justify the differences in magnitude and distribution of lateral seismic soil pressures obtained from different analytical methods (i.e., limit-state and elastic-based), Brandenberg et al. (2015) developed a dynamic framework to define seismic earth pressures on infinitely long and rigid U-shaped walls with a rigid base. The authors suggest that seismic soil pressures are inherent to inertial forces applied to the wall and evaluate seismic soil pressures from kinematic interactions as a function of the ratio of earthquake wavelength to wall height. Hence, induced seismic stresses at different levels of the wall, z, are attributed to the relative displacement between the free-field motion, $u_g(z)$, and the wall displacement $u_w(z)$. This method assumes that the embedded structure is excited by horizontally coherent, vertically propagating shear waves and full bonding exists between the soil and the structure. The soil-wall interaction is defined by stiffness intensity terms, k_y^i, and k_z^i and the soil-foundation interaction is defined by stiffness parameters, K_y and K_{xx}, in translation and rotation, respectively. Kinematic wall pressures and

their resultant force, P_E (Eq. 6), and moment, M_E (Eq. 7), are generated due to the incompatibility in displacement of the rigid wall and the free field soil-column and could be calculated through multiplying this differential wall/soil displacements and the wall-soil stiffness:

$$P_E = \int_0^H k_y^i \left[u_{g0} \cos kz - u_w(z)\right] dz \quad (6)$$

$$M_E = \int_0^H k_y^i (H - z) \left[u_{g0} \cos kz - u_w(z)\right] dz \quad (7)$$

where the superscript i denotes the stiffness intensity measured in units of F/L^3. $k = 2\pi/\lambda$ is wave number, and λ is the wavelength of the vertically propagating shear wave. For a rigid wall and foundation system, the wall displacement, $u_w(z)$, is:

$$u_w(z) = u_{FIM} + \theta_{FIM}(H - z) \quad (8)$$

where u_{FIM} and θ_{FIM} are base slab translation and rotation, respectively. For soil supports with infinite stiffness (i.e., rigid base), θ_{FIM} should be zero and u_{FIM} must be equal to the free-field displacement at the level of the base of the wall (i.e., $u_{FIM} = u_{g0} \cos kH$). Thus, the soil pressure distribution can be obtained as:

$$p_E(z) = k_y^i [u_{g0} \cos kz - u_{g0} \cos kH] \quad (9)$$

In 2017, Brandenberg et al., extended this solution to rigid walls with inhomogeneous backfill soils (i.e., soil layers with a smooth variation of shear modulus with depth) resting on a rigid base.

By characterizing the vertical variation of horizontal displacements in a free-field soil column, Brandenberg et al., developed a solution for single walls and a pair of walls spaced at a finite distance. The assumption of a rigid wall founded on a rigid base does not correspond to a typical configuration of retaining walls and leads to an overestimation of seismic earth pressures. Therefore, the authors present a Winkler stiffness density relationship based on the relative displacement between the soil and the wall which can be used to extend the applicability of the method to more realistic geometric conditions. Later in 2018, Durante et al., investigated the Winkler stiffness intensity for flexible elastic walls located on a rigid base through a series of numerical modeling using the pseudo-static approach. They presented a correction factor for evaluation of Winkler stiffness intensity for this type of walls relative to rigid walls. Extended analytical solutions for flexible wall systems that release rigid base condition are currently underway but not available for publication yet (personal communication).

1.4. Numerical studies

Numerical methods have been used by many researchers to investigate the dynamic behavior of retaining walls and embedded structures and along with experimental and analytical studies have provided additional valuable insights into the seismic soil pressures problem (e.g., Wood 1975, Alampalli and Elgamal 1990).

Richards et al. (1990) adopted a kinematic model with the soil material simulated through spring elements and suggested the point of application of the resultant of seismic soil pressures to be a function of the wall's movement.

Al-Homoud and Whitman (1999) used a finite element numerical model to analyze rigid abutment walls retaining and founded on dry sand. The researchers compared the results with those of dynamic

centrifuge tests and observed that there was a good agreement between both methods for wall displacement.

In 2005, Psarropoulos et al. investigated the accuracy and applicability of the analytical solution proposed by Veletsos and Younan, (1997) through the 2D numerical modeling and developed a more general finite-element method of this solution.

Jung and Bobet, (2008), numerically expanded the results obtained by Veletsos and Younan (1997), by adding vertical and horizontal translational springs to the base of the initial model proposed by Veletsos and Younan (1997). After performing a set of parametric studies, they found out that the wall rotational, bending, and translational flexibilities significantly affect the magnitude and distribution of the dynamic pressure. Moreover, Jung and Bobet (2008) concluded that the dynamic earth pressure behind a rigid wall with a stiff foundation is larger than that for a flexible wall with a soft foundation.

In addition to performing dynamic centrifuge experiments and analyzing the experimental results, Al-Atik and Sitar (2010), Geraili Mikola and Sitar (2013), and Wagner and Sitar (2016) utilized the 2D numerical modeling approach for further investigation of their experiments, and all reported good agreements between their numerical and experimental results.

1.5. Objectives and scope

The accurate evaluation of seismic soil pressures is an essential component of the structural design of retaining walls and embedded structures. As it was discussed earlier, the existing analytical approaches used for the analysis of seismic soil pressures (i.e., limit-state and elastic-based methods) have been initially developed for two extreme cases of soil-wall systems (i.e., yielding, and non-yielding). The examples of these two extreme cases are sparse in practice, and

the seismic behavior of most of the retaining walls and embedded structures is different from either of these two cases. Moreover, using different assumptions even different methods of the same approach for a specific retaining structure may provide contradicting results, and thus, there is not a general consensus on the seismic design methodology of this type of structures. Comparing to shallow 2D retaining walls, deep underground structures experience 3D load effects and the influence of the important parameters which are usually ignored by the analytical methods (e.g., the soil nonlinearity, flexibility of the structure relative to the retained soil, and stiffness of the layer overlain by the structure) becomes more pronounced for them. Thus, a reliable method for evaluation of seismic performance and lateral earth pressure distribution on deep flexible understructures is missing in the field of earthquake engineering. Utilizing the results of a series of large-scale shake table tests performed on underground structures, the main aim of this study is to work towards shedding light into the complex seismic soil-structure interaction phenomena through numerical and analytical studies and derive simple graphical solutions for prediction of seismically induced soil pressures on deep underground structures. Large-scale shake table testing of an underground structure system with two vertical shafts, two shield tunnels, and one cut-and-cover tunnel were executed at the E-Defense facility in Miki, Japan (Lemnitzer et al., 2017, Kawamata et al. 2016). These tests will serve as the experimental reference for this study. A number of novel, large-area soil pressure sensors, recently developed by our group, were utilized to experimentally assess seismic soil pressures on underground structures during various earthquake motions. The sensor development and sensor calibration represent a unique instrumentation contribution of this study.

A detailed review of the performed shake table tests is presented in chapter 2. Different aspects of the tests including the experimental setup, material characterization, construction procedure, instrumentation, and applied motions are explained comprehensively in this chapter.

Chapter 3 of this dissertation is dedicated to the design, development, and calibration of the pressure cells developed by our research group. First, a summary of the most common devices used for the measurement of contact soil pressures, their applications, advantages, and limitations are summarized. Then, different aspects of the newly developed sensors including their design, static and dynamic calibration procedures are thoroughly described.

In chapter 4, experimental results of the performed shake table tests (e.g., dynamic system characterization, site response analysis, seismic soil pressure time histories and, pressure distribution profiles) is presented. The accuracy of the different elastic-based and limit-state methods in the prediction of the distribution and magnitude of seismic soil pressures on deep underground structures is then studied through comparison with the recorded seismic soil pressures.

After analyzing the experimental results and comparing them with the analytical approaches, the seismic behavior of deep underground structures was further studied through the 3D finite element modeling approach. A detailed description of the numerical models' development, calibration, and results are presented in chapter 5. The numerical approach was first verified and calibrated against the executed shake table tests. By keeping the configuration of the shake table tests consistent, the calibrated models were then used in a limited set of parametric studies to investigate the effects of the structure's adjacent soil parameters (i.e., cohesion, and friction angle) and the flexibility of the structure on the resulting soil pressures. In order to obtain a better understanding of the behavior of deep underground structures under seismic motions, a simplified

3D soil-structure model was then developed, and the influences of the most important parameters on the seismic soil pressures were studied through an extensive set of parametric studies. Results of these analyses are summarized as a series of normalized graphs which could serve as preliminary estimate in the design of deeply embedded retaining structures. It should be noted that the results of chapters 2 to 4 of this dissertation, have been previously published as stand-alone papers (Lemintzer et al. 2017, Keykhosropour et al. 2018, and Keykhosropour and Lemnitzer 2019).

Chapter 6 provides a summary of this research and concludes the dissertation.

Chapter 2

Experimental setup

2.1. Introduction

With the aim of understanding of the dynamic response and interaction of underground structures in densely constructed urban areas, a series of large-scale shake table tests were performed at the E-Defense facility in Miki, Japan which is owned by the Hyogo Earthquake Engineering Research Center of the National Research Institute for Earth Science and Disaster Resilience (NIED). To date, the E-Defense shake table is the largest shake table in the world with dimensions of 15 m in width and 20 m in length. The table's payload is 12 MN and was originally designed to simulate the demands posed by records of the 1995 Kobe Earthquake. A recent upgrade in 2013 allows the table to replicate long duration earthquakes as observed in the 2011 East Japan event. A system of 10 horizontal and 14 vertical actuators is able to produce table accelerations of > 900 cm/s^2 (0.92 g) in the x and y directions, and accelerations of > 1500 cm/s^2 (1.53 g) in the z direction. Maximum applicable displacements are ±100 cm in each horizontal and ±50 cm in the vertical direction (Ohtani et al. 2003). Several soil-structure interaction experiments have been conducted on the shake table in the past (e.g., Tokimatsu et al. 2007, Suzuki et al. 2008) and investigated the dynamic responses of superstructures supported by pile groups in dry and liquefiable sand.

The objective of this chapter is to present the experimental framework and the generated data sets of the "E-Defense shake table tests of underground structures in sand" project and, to feature the potential reuse of recorded measurements by the earthquake engineering research community.

Two systems of horizontal and vertical underground structures were installed in a laminar soil container with a diameter of 8.0 m and a height of 6.5 m. The soil container consisted of 40 laminar rings which are made of hollow, rectangular steel sections and connected through roller bearings to allow flexible, bi-directional movement of the soil fill.

This study complements and expands upon current knowledge in that it benefits from the scaling of the structural components and extensive instrumentation (> 800 sensors) while challenging investigators with the complexity of a dense structural configuration inside the soil container.

Testing described in this chapter was conducted from 23-28 February 2012. A U.S.-Japanese collaboration was established for the instrumentation of one vertical shaft with 20 large diameter pressure sensors to investigate the seismic soil pressures on an elastic structural element (Lemnitzer and Lu, 2013). This collaboration was funded by the National Science Foundation under grant # RAPID US: NSF-NEESR CMMI-1203212. All other instrumentation was provided by the Japanese research team, funded by a Management Expenses Grants of NIED, Japan. Since 2015, response data of the entire system are publically available (upon request) to researchers in compliance with the E-Defense data regulation and proprietary agreements; that is, data are reserved for a minimum of two years for the principal investigators only. Relevant test data obtained from the comprehensive instrumentation are stored at the DesignSafe Data Depot developed through NSF's Natural Hazard Engineering Research Infrastructure (NHERI) program and can be directly accessed in the Public Data at the Data Depot or via a generic DOI search at http://www.doi.org, using10.17603/DS21C78 (Lemnitzer et al. 2016).

This chapter describes the general test setup, model materials, model instrumentation, and data acquisition, as well as data processing and organization at NHERI's DesignSafe Data Depot

platform. Except for the structural modification of the joint connections upon completion of the first large ground motion applied to the system (namely, the Kobe shake at 50% scaled acceleration), the test setup and geometries stayed identical between all shaking experiments. A detailed analysis of the results, regarding the obtained seismic soil pressures, as well as the evaluation of different aspects of the dynamic response of the system, are presented in the next chapters; several component studies such as the evaluation of the cut-and-cover tunnel or the performance of the structural joints can be found in Towhata et al. (2014) and Kawamata et al. (2016).

2.2. Experimental setup

The general test setup is depicted in Figures 2.1 and 2.2. While no specific prototype was followed for this experiment, the selection of the structural components was motivated by typical underground structures and subsurface infrastructure components in dense urban areas in Japan (e.g., Metro systems and underground utility tunnels in Tokyo or Osaka), which are similar to urban underground systems worldwide. With the objective to mimic the system's in-situ behavior as closely as possible, while maximizing the component scaling and minimizing the influences of the container boundaries, five underground structures were installed inside the laminar container. The underground structures consisted of aluminum model structures scaled to 1/20 of their corresponding prototype size and overall bending stiffness, and maintained typical geometric shapes of subsurface structures in urban construction. Two hollow, vertical shafts with dimensions of 0.8m square, 12 mm in thickness and 7.0 m in total height were spaced 4.80 m apart (center to center) and connected through a horizontal cut-and-cover tunnel with dimensions of 0.6 m in width and 0.3 m in height. The horizontal tunnel was installed at an elevation of 5.3 m from the container

bottom and was covered by a 0.4 m layer of soil fill (thickness to ground elevation at 6.0 m). The connections between the vertical shafts and the cut-and-cover tunnel were constructed as rigid and flexible joints, to study the localized damage development for both connection types between the coupled underground structures.

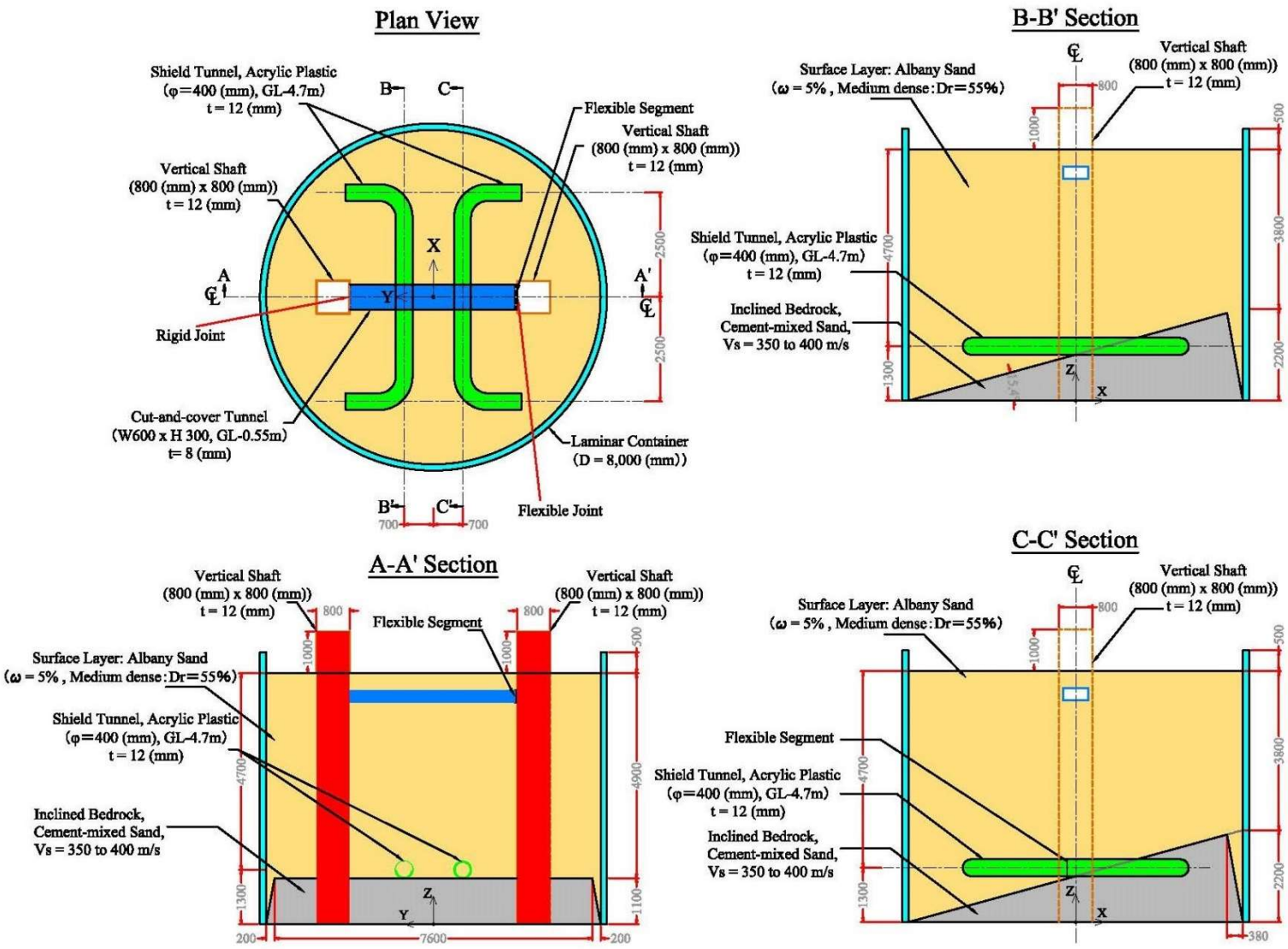

Figure 2.1. Test specimen plan and section views

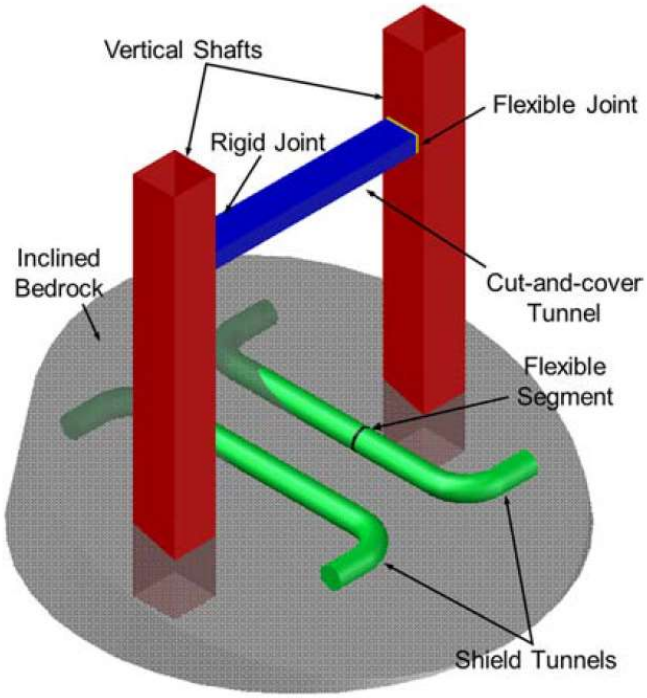

Figure 2.2. 3D model of the test specimen

Joint flexibility was accomplished by installing rubber sheeting between the cut-and-cover tunnel and the vertical shaft connection. Five sheets of 10 mm thick rubber and four plates of 1.2 mm thick steel were laminated with high tensile adhesive to form a seismic isolation pad. The rigid joint was simulated by fixing the cut-and-cover tunnel to the vertical shaft through stainless steel bolts. Two independent, U-shaped shield tunnels with dimensions of 0.4 m in diameter, 12 mm in thickness and 5.0 m in total length were installed at an elevation of 1.1 m from the container bottom (Figure 2.1). The shield tunnels were spaced 1.4 m center-to-center and placed in between the two vertical shafts. No significant interaction between the vertical and horizontal elements was expected, as the clear spacing between the shield tunnels and vertical shafts was 1.1 m. Both shield tunnels were fabricated from acrylic plastic and assembled with a glue that has a higher bond strength than acrylic plastic to replicate the flexibility of this type of structure. The particular

arrangement of the structures inside the laminar soil box was motivated by the following objectives: (1) to simulate a dense, yet realistic substructure system in which horizontal and vertical elements intersect and interact, (2) to maximize the element size within the available container space to obtain a "reduced prototype geometry," rather than a "model-scale" system (as found in centrifuge testing), (3) to capture the structural and SSI behavior in similar way as found in the in-situ elements. Hereby of primary interest was to preserve a bending-type behavior in the vertical shafts. A scaling factory of 20 worked well in converting a typical in-situ system into a small prototype, while maintaining the inherent system behavior.

Figure 2.1 indicates a two-layer soil stratum in the container. The two significantly different strata were used to study the localized impedance effects of the soil on the structural elements and observe possible interface damage development in the horizontal and vertical structures. The upper layer consisted of sand with an average thickness of 4.9 m, while the lower, stiffer soil stratum consisted of cemented sand. The stiff soil was sloped at a 15.4 degree angle and reached a maximum layer height of 2.2 m. This soil stratum did not touch the outside container walls to preserve flexible container movement (see Figure 2.1). The vertical shafts were attached to the container base by welding 1.0 m square aluminum plates to the shaft bottom, followed by strengthening the aluminum section with steel plates and bolting the combined cross section to steel channels welded on the bottom of the container. Additional fixity of the vertical shafts against rotation and translation was assumed to be provided by the cemented soil layer (Kawamata et al. 2014). The available horizontal soil space between the vertical shafts and the laminar box walls was 1.2 m for each shaft. The minimum radial clearance between the shield tunnels and the container wall was 0.6 m, as shown in Figure 2.1.

2.3. Model construction and load application

2.3.1. Construction procedure

The construction of the test specimen was performed in six stages as illustrated in Figures 2.3a-f. Due to constraints related to the shake table availability, the specimen assembly began off-site and the soil container was moved at a 30% assembly level on the table, where construction was completed.

Construction stage one consisted of placing and fixing the vertical shafts in the empty container (Figure 2.3a). Vertical shafts were surveyed to maintain their position throughout the remaining construction process. In a second step, the cemented soil material and the moist Albany silica sand were placed between the base of the container and the elevation of the shield tunnels, followed by the installation of the shield tunnels and the soil placement around such (step 3). The soil was compacted via vibratory plate compaction. Soil placement and compaction continued hereafter in successive layers of approximately 25 cm in thickness until the elevation of the cut-and-cover tunnel was reached (step 4). Step 5 consisted of installing the cut-and-cover tunnel between the two vertical shafts via flexible and rigid joint connections. Construction of the flexible joint was assisted by chains that supported the dead weight of the tunnel. Remaining soil filled the model up to an elevation of 6.0 m from the container bottom (step 6).

Structural instrumentation such as strain gauges and pressure sensors attached to the vertical shafts and tunnel sections were installed prior to placement of the structural elements inside the laminar container. Soil instrumentation such as accelerometers, bender elements, and displacement transducers were installed concurrently with soil placement. After completion of the construction, external instrumentation consisting of displacement transducers, laser transducers, high speed

video cameras and visual targets were installed at the model surface. A rigid frame system was used to mount all external appliances (Figure 2.3f).

Figure 2.3. Assembly stages of the test specimen

2.3.2. Loading

Table 2.1 summarizes the base excitations applied to the container model. The peak base acceleration was determined using four accelerometers installed at the surface of the container table along the circumference of the soil container and averaged by time. Given the rigid connection of the container table (i.e., base plate) and the stiffness of the table itself, shake table and container table accelerations are assumed to be equal. The organization of data into experiments, trials, and repetition follows the data storage requirements of the former NEES project warehouse. Hereby, an experiment describes as the overall configuration to be tested, a trial represents the various load applications and a repetition indicates a simple repeat of the same loading to improve the data quality or to record changes. As the experimental setup remained essentially the same during the course of this project, the various applied motions and intermediate recording of the system data are only distinguished as trials, that is, Trials 1–13. Of particular interest to the research community are Trials 12 and 16, which document the response to the applied earthquake loading and the sine sweep/step functions for system identification analyses. The applied motions include: (1) 50% and 80% scaled ground motions measured during the 1995 Kobe earthquake at the JR Takatori Station (N34.651339, E135.135203; Nakamura et al. 1996), and (2) step sine sweeps over a frequency range of 1–20 Hz intended to characterize the dynamic response of the model at various acceleration levels, that is, 0.1 m/s^2, 0.3 m/s^2, and 0.5 m/s^2. The step sine motion was applied via two cycles per frequency, with frequencies gradually increasing from 1 to 20 Hz. In the frequency range between 9 and 17 Hz increments increased in 1/8 Hz steps, at all other frequency ranges loading increments increased in 1/4 Hz steps. Via pre-test prediction studies, the fundamental period of the model was estimated to be around 13 Hz (Kawamata et al., 2012). Additional modes were predicted in the range of 9-17 Hz.

The Kobe earthquake represents one of the most characteristic earthquake records for Japan and is readily available in the E-Defense shake table input catalog. Its selection as experimental input motion was motivated by the record's capability of generating large ground displacements (as observed in 1995), and the associated deformation demand that this motion would post on the soil-structure assembly in the container. Pre-test prediction studies suggested that the 80% Kobe motion would suffice to generate failure in the structural system. In addition, this limit was also helpful in preventing damage to the shake table equipment, as small damage at the container bearings was observed at the end of Trial 16, suggesting the 80% scaled input motion to be an upper limit for future SSI studies using the laminar soil box. The east-west component of the Takatori motion was input in the model's x-direction, while the north-south component was chosen for the y-direction. The selection thereof was based on the orientation of the cut-and cover tunnel and its rotational demands. Peak base accelerations (PBA) at the table in x and y directions were recorded as 3.77 and 3.12 m/s^2 for the 50% EQ, and 6.76 and 5.68 m/s^2 for the 80% EQ, respectively. No vertical motion was applied to the model; however, small vertical accelerations with magnitudes of 4–6% of the horizontal accelerations were recorded indicating table rocking during the load application. The target input motions and measured table motions were observed to be in good agreement in the low and medium frequency range, small discrepancies between the input and target motion at low frequencies were observed. This difference can be attributed to the table-specimen interaction and the noise in the hydraulic system.

Table 2.1. Overview of loading parameters

Trial	Date	Time	Name	Properties	Max. input acc. [m/s^2]	PBA [%g] (container bottom)	CSV File Name
-	23-Feb	6:56 AM	Before Shaking		-		
-			Balance[1)]				
1		1:24 PM	Step Sine 0 Degree (x-axis)	1-20 Hz	0.1	1.02	StepSine-10Gal-0Deg.csv
2		1:39 PM	Step Sine 90 Degree (y-axis)	1-20 Hz	0.1	1.02	StepSine-10Gal-90Deg.csv
3		1:59 PM	Step Sine 0 Degree (x-axis)	1-20 Hz	0.3	3.06	StepSine-30Gal-0Deg.csv
4		2:20 PM	Step Sine 90 Degree (y-axis)	1-20 Hz	0.3	3.06	StepSine-30Gal-90Deg.csv
5		2:39 PM	Step Sine 30 Degree	1-20 Hz	0.3	3.06	StepSine-30Gal-30Deg.csv
6		2:59 PM	Step Sine 45 Degree	1-20 Hz	0.3	3.06	StepSine-30Gal-45Deg.csv
7		4:04 PM	Step Sine 135 Degree	1-20 Hz	0.3	3.06	StepSine-30Gal-135Deg.csv
8	24-Feb	7:37 AM	Record Residual		-		Residual-1.csv
-			Balance[1)]				
-		9:13 AM	After Balance		-		
-		1:05 PM	Before Shaking		-		
-			Balance[1)]				
9		1:29 PM	Step Sine 90 Degree (y-axis)	1-20 Hz	0.3	3.06	StepSine-30Gal-90Deg-2.csv
10		1:59 PM	Step Sine 0 Degree (x-axis)	1-20 Hz	0.5	5.10	StepSine-50Gal-0Deg-2.csv
11		2:29 PM	Step Sine 90 Degree (y-axis)	1-20 Hz	0.5	5.10	StepSine-50Gal-90Deg-2.csv
12		3:01 PM	JR Takatori @ 1995 Kobe EQ	50% scale	3.77 (x) 3.12 (y)	38.43 (x) 31.80 (y)	JRTakatori-50%.csv
13	27-Feb	7:55 PM	Record Residual		-		Residual-2.csv
-			Balance[1)]				
-	28-Feb	8:34 AM	Record Residual		-		
-			Balance[1)]		-		
-		9:02 AM	After Balance		-		
-		11:38 AM	Before Shaking		-		
-			Balance[1)]				
14		12:02 PM	Step Sine 90 Degree (y-axis)	1-20 Hz	0.3	3.06	StepSine-30Gal-90Deg-3.csv
15		12:45 PM	Step Sine 0 Degree (x-axis)	1-20 Hz	0.3	3.06	StepSine-30Gal-0Deg-3.csv
16		2:00 PM	JR Takatori @ 1995 Kobe EQ	80% scale	6.76 (x) 5.68 (y)	68.91 (x) 57.90 (y)	JRTakatori-80%.csv

1) Balancing means zeroing all sensors

2.4. Instrumentation

To characterize the structural and geotechnical response of the model, 848 sensors were installed. Instrumentation consisted of earth pressure sensors, strain gauges, accelerometers, and displacement transducers to capture the dynamic response of the model.

Figures 2.4 and 2.5 exemplarily depict the instrumentation types and locations on the vertical shafts. VSR and VSF in Figure 2.4 and 2.5 denote the sensors at the Vertical Shaft with Rigid or Flexible joint connections to the cut and cover tunnel, respectively. A, P, D, and S represent the respective sensor type, that is, Accelerometers, Pressure sensors, Displacement transducers and Strain gauges. The depth below ground surface (in mm) as well as the shaft side (1, 2, 3, or 4) or recording direction (x, y, z) are indicated for each sensor coordinate. Similarly detailed instrumentation drawings are available for the cut and cover tunnel and the shield tunnels at the DesignSafe Data Depot. The two vertical shafts were equipped with 20 accelerometers (ASW 5A/Kyowa Electronic Instruments) each, attached to the inside of the shaft and vertically spaced at approximately 0.7-1.0 m. As shown in Figure 2.4, each accelerometer set consisted of two sensors measuring x and y accelerations; four of the accelerometer sets recorded z accelerations also.

Figure 2.4 also depicts the earth pressure sensors installed along the shafts. The VSF shaft (depicted on the right side of Figure 2.4) was instrumented with a total of 12 strain gauge-based, commercially available earth pressure sensors (BEN-A-500KP/Kyowa Electronic Instruments) with a maximum pressure capacity of 500 kPa. This sensor is a dual diaphragm sensor with the pressure medium sealed between the pressure-sensing surface and strain gauge bonded diaphragm). The sensors were installed in predrilled, sealed holes on all four shaft sides at elevations -0.1 m, -3.0 m, and -4.50 m below ground surface.

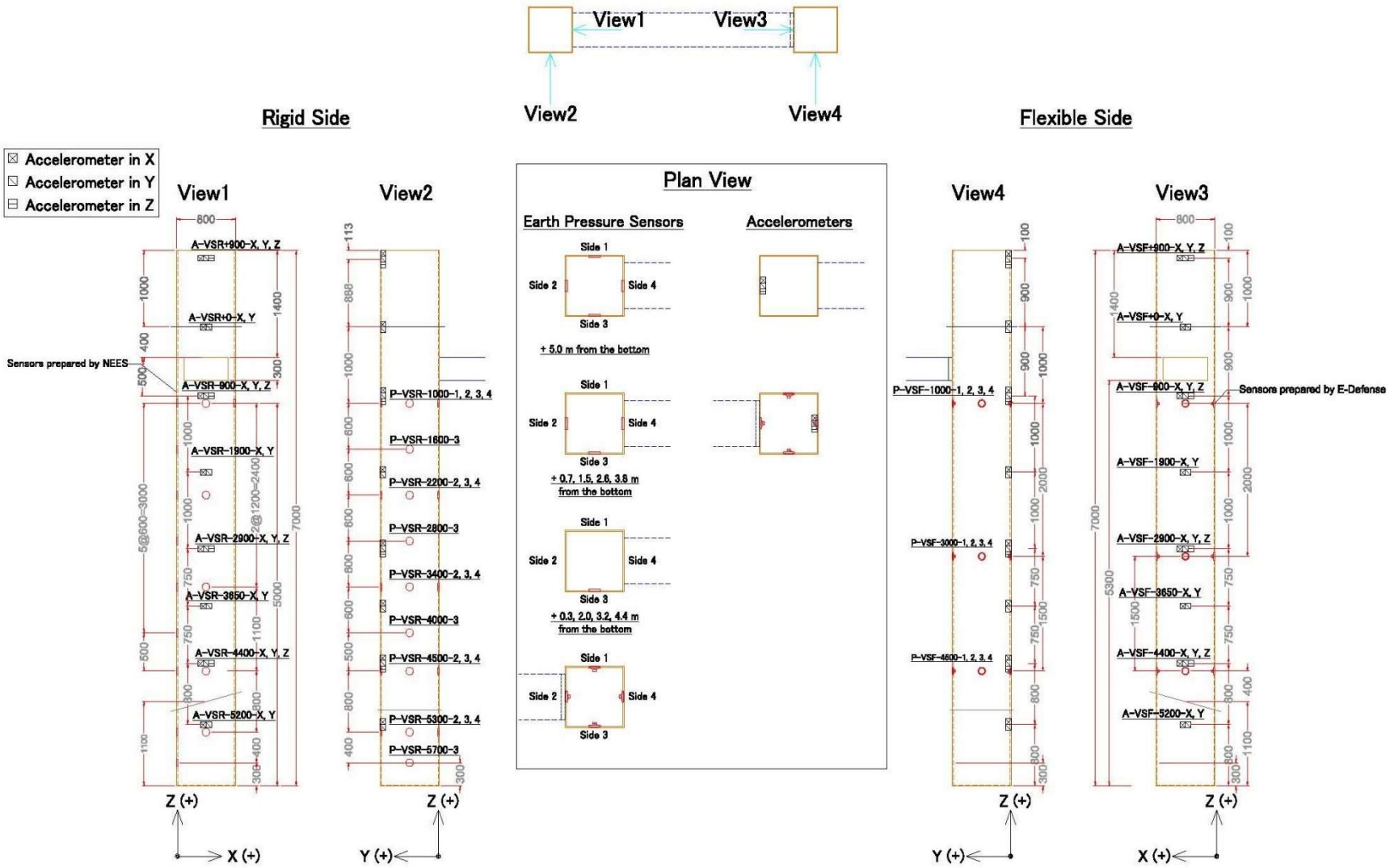

Figure 2.4. Accelerometer and pressure sensor instrumentation on the vertical shafts

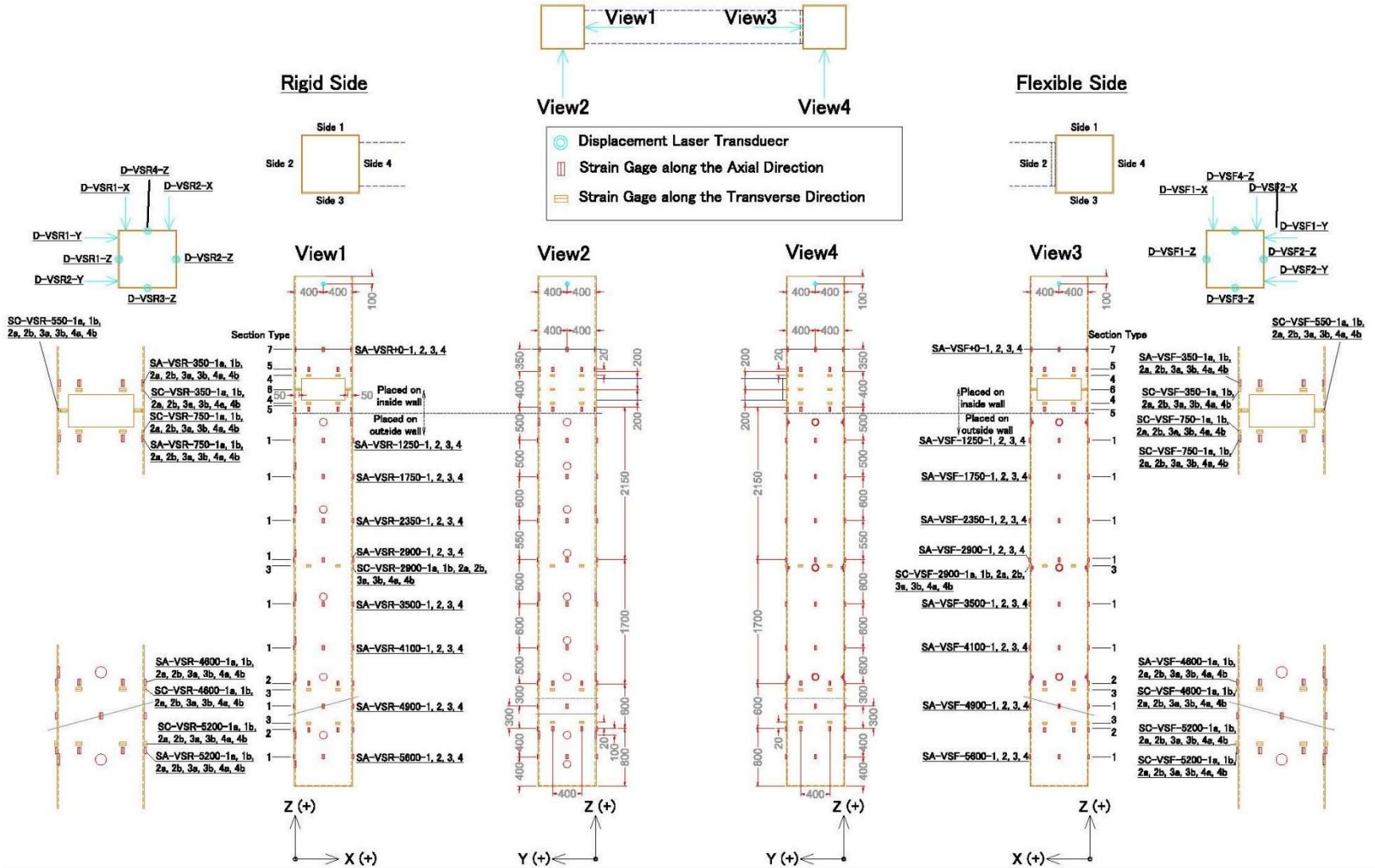

Figure 2.5. Strain gauge instrumentation on the vertical shafts

The installation of load-cell based earth pressure sensors on the VSR shaft was enabled through the U.S.-Japanese collaboration. Four earth pressure sensors with a capacity of 288 kPa were installed in the cemented soil layer at an elevation of 0.3 m from the container bottom. 16 additional sensors with a maximum capacity of 144 kPa were spaced vertically (approx. 0.6 m on average) over the remaining height of the vertical shaft. The earth pressure sensors were 10 cm in diameter and manufactured with aluminum cases to comply with the stiffness of the vertical shaft material. The sensor surface and the vertical shaft surface formed a flush pressure area in order to minimize localization effects around the sensors. Similar in-house pressure sensors with different material and pressure capacities were successfully manufactured and implemented in previous static abutment testing by Lemnitzer et al. (2012) and Stewart et al. (2011) and lent to dynamic testing of shallow foundations by Star et al. (2015) and retaining walls by Fox et al. (2015).

A total of 232 strain gauges (Single-element/FLA-10-11/Tokyo Sokki Kenkyujo) were installed in both shafts in axial and transverse direction. Gauges near the shaft ends and their mid-section were installed on the outside, while sensors at the top portion of the shafts were attached on the inside. Figure 2.5 describes the exact elevation and direction of each strain gauge set. Eight laser displacement transducers (LK-500/Keyence) were added at the top of the vertical shaft (outside the soil) to record shaft displacement and rotations in x, y, and z directions. Visual targets were attached on the inside of the flexible joint connection and displacements were recorded using laser transducers.

Identical instrumentation as described above (i.e., strain gauges, accelerometers and earth pressure sensors) were installed at the cut-and-cover tunnel (60 × S, 9 × A, 12 × P) as well as the shield tunnels (96 × S, 18 × A, 8 × P, each tunnel). In addition, laser displacement transducers

(IL-100, LK-G500, and LK-G80/Keyence) and high speed cameras were placed in both tunnel structures to measure joint deformation and rotations internally.

The instrumentation of the soil fill and the external instrumentation of the container walls are depicted in Figure 2.6. The laminar container (LC) was instrumented with (60) accelerometers labeled A-LC and (22) displacement laser transducers labeled D-LCS as indicated in the cross-sectional views of Figure 2.6. Data records were used to identify the overall system deformations. Instrumentation of the soil fill consisted of accelerometers arranged along four vertical arrays (labeled Array 1-4) and bender elements (not shown in Figure 2.6) to capture the soil properties before and after shaking. Laser displacement transducers (LK-500/Keyence) were used to measure displacement of the ground surface.

Settlements of the upper soil layer at different depths were estimated using wire-type displacement sensors as shown in Figure 2.7. Plastic plates with aluminum rods were placed at depths of -1 m, -2 m, -3 m, and -4 m below ground surface, while the top of the rods extended above the ground surface. To eliminate effects of friction around, the rods were covered with vinyl chloride pipes. Wire-type displacement transducers (DP-500D/Tokyo Sokki Kenkyujo) were fixed on the rigid frame and connected to the tops of the rods with steel wires. It is noted that displacement records of these sensors during the duration of load application are a combination of lateral and vertical soil displacements, while residual measurements can be approximated as closer to being only vertical settlements.

The “instrumentation” folder at the DesignSafe Data Depot includes a comprehensive set of files that include lists of sensor coordinates (based on the global coordinate system) in pdf and excel format, sensor types, as well as instrumentation plans in jpeg format for each structural element.

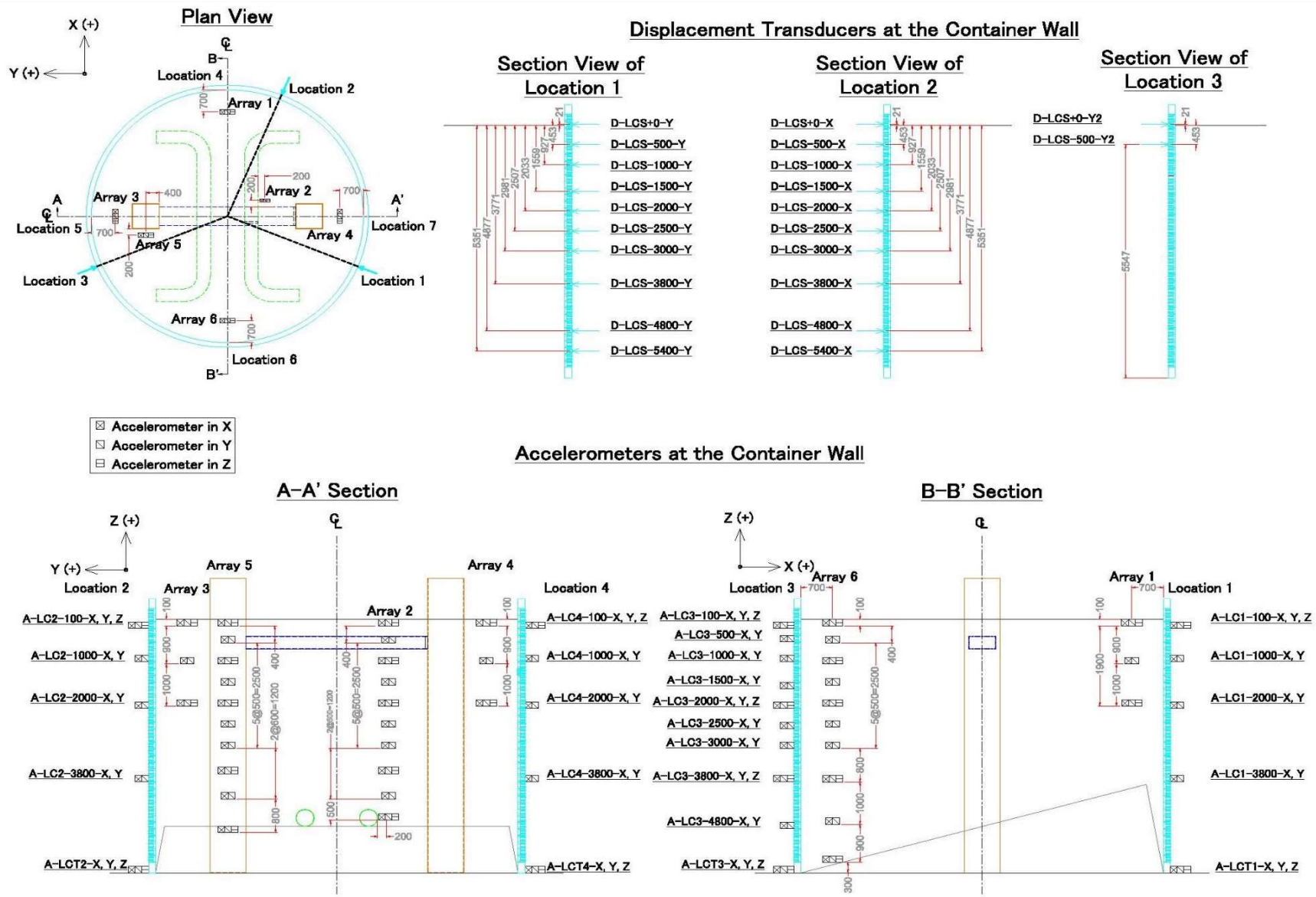

Figure 2.6. Instrumentation on the laminar container and inside the soil material

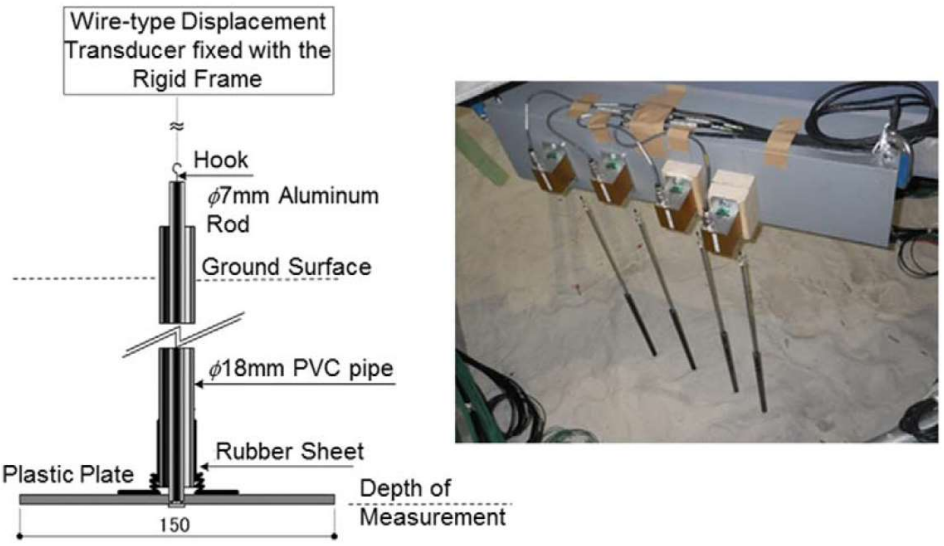

Figure 2.7. Displacement transducer at various soil depths to estimate ground settlements

2.5. Material characterization

2.5.1. Structural components

The structural components (shafts, tunnels) were fabricated using standard aluminum and acrylic plastic materials. This material choice was guided by the construction cost, the ease and safety of construction and assembly, as well as a good match with the overall target bending stiffness of the system. While overall system scaling complied with scaling laws in terms of bending, sectional stiffness and corresponding sectional deformations only approximated its prototype. Specifically, the scaling factor of 1/20 enabled proper geometric and stiffness scaling to assimilate the stiffness of an overall underground structure system when constructed with reinforced concrete, yet cross-sectional deformations within individual elements, are an approximation of its actual behavior. For instance, the wall thickness of the vertical shafts was in accordance with scaling laws, however, at some locations element thicknesses had to be increased to maintain structural stability during shaft erection and construction and proper scaling compliances could not be warranted at all times. Tensile testing of the aluminum and the acrylic

plastic materials revealed an E-modulus of 70.1 GPa and 3.3 GPa, respectively. The vertical shafts and the cut-and-cover tunnel were coated with a very thin layer of silica sand-cement paste to better represent in-situ concrete-soil friction.

2.5.2. Soil materials

The soil material was taken from the E-Defense facility's on-site storage, where approximately 1,000 tons of #48 Albany silica sand are stockpiled for geotechnical investigations.

Mechanical properties of the soil materials were obtained through laboratory and in-situ testing (e.g., Dutch cone penetration testing and shear wave velocity measurements). In addition, a site response type of analysis was performed using the sine sweep loading. Depending on the analytical approaches used for comparison between analytical and experimental results (i.e., limit-state or elastic-based), and in preparation for numerical studies, a thorough soil characterization was conducted to determine two sets of mechanical properties for each layer: (1) the shear modulus G, poisson's ratio ν, and damping ratio ζ (presented in chapter 4), and (2), the cohesion c and friction angle φ.

Consolidated undrained triaxial shear test (CU) responses of the Albany sand at relative densities, D_r of 40%, 60%, and 80% are depicted in Figure 2.8a-c. Each test set was conducted at three different confining pressures (i.e., 50, 100, and 150 kPa). The corresponding combination of friction angle φ and cohesion c for each sample density, i.e., 40, 60, and 80% were measured to be $\varphi = 31°$ and $c = 32$ kPa, $\varphi = 35.5°$ and $c = 17$ kPa, and 37.6° and 48 kPa, respectively.

Skempton's pore pressure parameter was kept above 95% during the entire triaxial testing procedure, hence the specimens were assumed to be fully saturated. For a given average relative density of $D_r = 54.05\%$ in the upper sand strata, it was decided to use the cohesion and friction angle obtained from the (CU) test at $D_r = 60\%$ (i.e., c = 17 kPa and $\varphi = 35.5°$). These results are

based on a linear approximation of the shear failure envelope. These tangent parameters are valid over a limited range of normal stresses corresponding to the CU tests, and it remains questionable whether the high amount of cohesion shall be considered apparent cohesion. By analyzing the triaxial test results using the secant method (i.e., assuming zero cohesion), a friction angle of $\varphi = 36°$ was obtained for the sand layer. Subsequent analyses will omit the presence of any cohesion and utilize the above-mentioned friction angle of 36°.

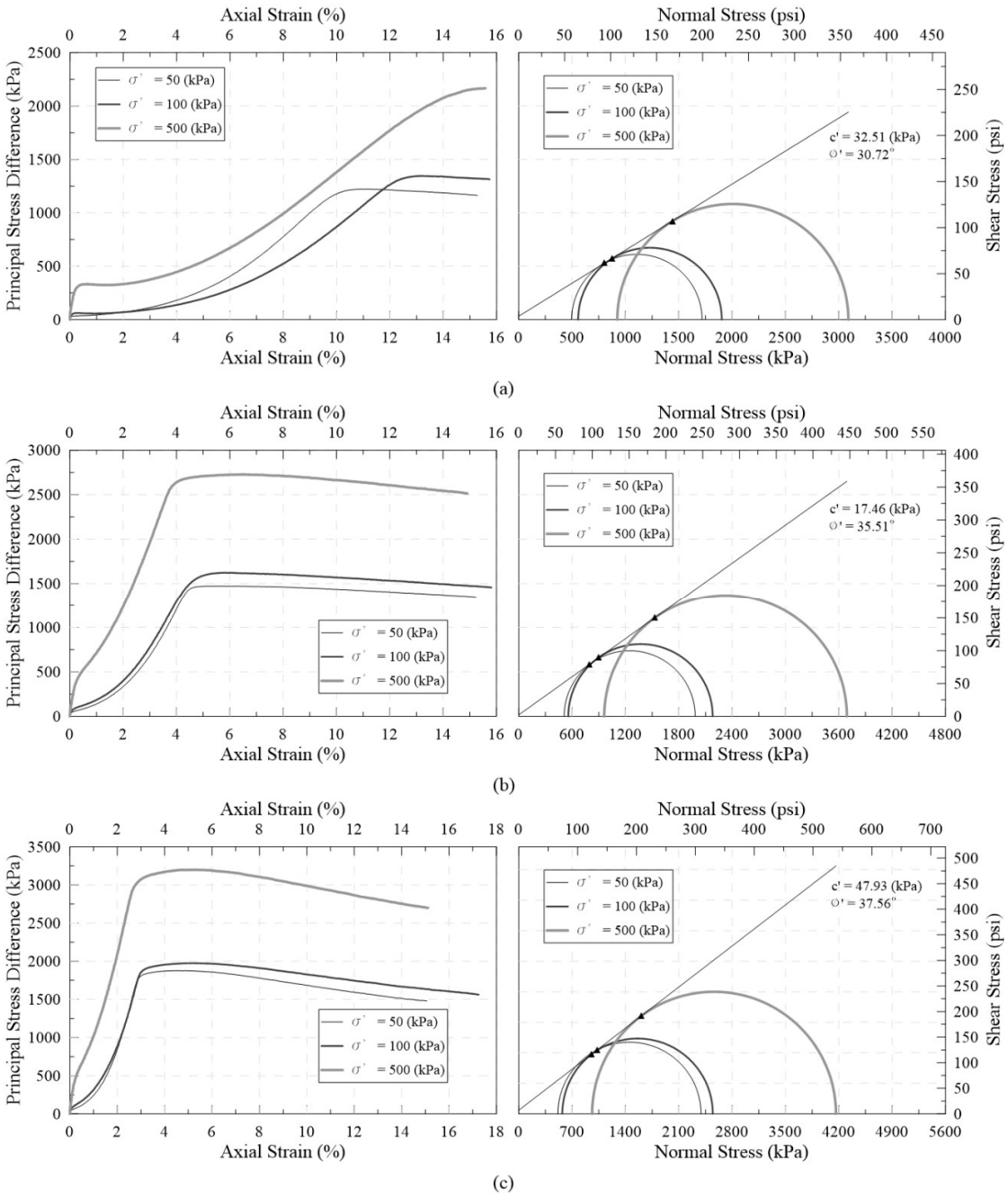

Figure 2.8. Triaxial test results for soil samples with different relative densities (a) 40%, (b) 60%, and (c) 80%

The inclined, stiff layer at the model base aimed to replicate a bedrock layer and was constructed as a mixture of silica sand, cement and water with a ratio of 100:7:12 by weight, respectively. A study by Maalej et al., 2007, suggested that mixing sand with cement does not

significantly alter the frictional angle but modifies the amount of cohesion to be proportional to the volume fraction of the cement in the mixture. Therefore, the frictional angle of the cemented layer was assumed to be 36° and the cohesion was determined by formulating the Mohr-Coulomb failure criterion in terms of unconfined compressive strength:

$$c = \frac{(1-\sin\ )\cdot UCS}{2\cos} = 334.19 \text{ kPa} \quad (1)$$

Properties of the silica sand before and after testing are summarized in Table 2.2 and Figure 2.9. The pre-shaking relative density was estimated using weight/volume data recorded during soil placement in the container, supported by laboratory test data of water contents and maximum/minimum densities. Post-shake densities were found to increase by 18% in average. Shear wave velocity (V_S) measurements were taken using bender elements installed at various heights throughout the soil layer.

The shear modulus G_{max} was computed using the average shear wave velocities of the respective layers (i.e., soil or rock) following NIST 2012 recommendations. $V_{s,ave}$ and G_{max} were approximated to be 175 m/s and 52 MPa, as well as 385 m/s and 311 MPa, for the sand fill and cemented layer, respectively. The average unit weight of the top layer was 16.59 kN/m^3. The unit weight of the bedrock (20.59 kN/m^3) was determined using the relationship proposed by Mayne (2007):

$$\gamma = 4.17 \ln(V_{s1}) - 4.03 \quad (2)$$

where $V_{s1} = V_s \left(\frac{p_a}{\sigma'_{v0}}\right)^{0.25}$ [m/s], σ'_{v0} is the in-situ effective vertical stress, and p_a = atmospheric pressure in the same units as σ'_{v0}.

Table 2.2. Properties of the surface layer

Soil Particle Density, (g/cm^3)	2.643
Maximum Void Ratio (e_{max})	0.796
Minimum Void Ratio (e_{min})	0.500
Average Water Content (w) Before the Tests, (%)	4.52
Average Water Content (w) After the Tests, (%)	4.28
Average Unit Weight (γ) Before the Tests, (g/cm^3)	1.692
Average Unit Weight (γ) After the Tests, (g/cm^3)	1.731
Average Relative Density (D_r) Before the Tests, (%)	54.05
Average Relative Density (D_r) After the Tests, (%)	71.95

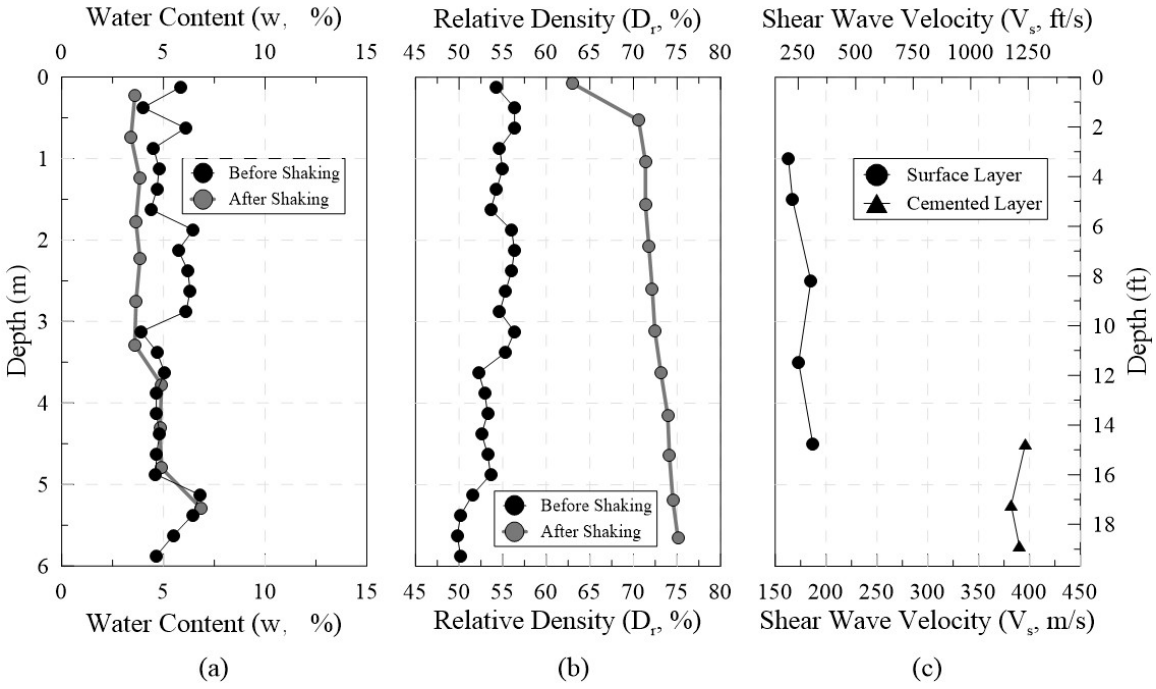

Figure 2.9. Soil properties

2.6. Data processing and archiving at the NHERI Data Depot

The DesignSafe Data Depot allows the user to choose the format and organization of data upload per researcher's preference. The data organization follows the layout depicted in Figure 2.10. The user can reach the data set via the Research Workbench → Data Depot → Public Data. Inside the project folder E-Defense Shake Table Tests of Underground Structures in Sand, Experiments, and Project Description subfolders are available that split the available information as shown in Figure 2.10. The Project Description folder stores experiment descriptions, publications and general information.

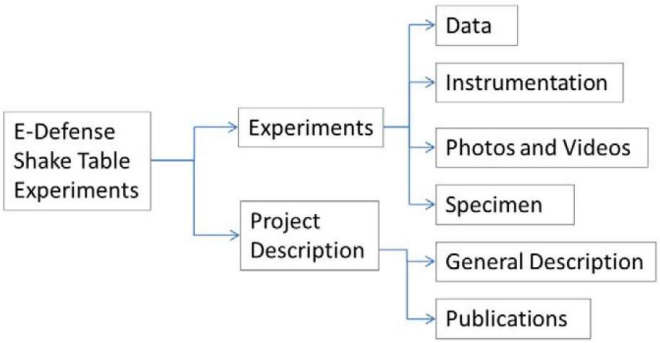

Figure 2.10. Data organization at the DesignSafe Data Depot

Data: The Data folder includes all sensor recordings as .csv files, organized in Trials per Table 2.1. Each Trial (i.e., each load application) folder includes a "readme" file that explains to the user the organization of the data records. This data organization follows the data format proposed by the former NEES project warehouse. Due to the complexity of the available measurements, the 848 sensor records are split in 14 data files. The readme file explains the user which sensor data are stored in which .csv file. Data files are organized by sensor types, and channel numbers, which were dictated by the organization of the E-Defense instrumentation engineers on-site. The files names are in accordance with the respective load application as shown in Table 2.1. All data were recorded at a sampling frequency of 200 Hz and stored in engineering units. Initial offsets

pertaining to initial sensor reading upon start of recording were removed. No filtering was applied and the user is encouraged to filter the data as desired. Data files labeled BeforeShaking, Balance, AfterBalance, etc. contain data related to zeroing the data acquisition system prior or after the load application or shake table balancing and instrumentation reset. These data are not beneficial for the user as they do not include static measurements of the system. The files are available upon request but were omitted in any of the data upload to avoid confusion. Sine wave and ground motion data files only contain dynamic data (i.e., only the dynamic response was measured, as all sensors were zeroed prior to load application). Sign conventions were selected in a manner to comply with the global coordinate system of the test specimen which can be found in Figure 2.1. To comply with E-Defense data regulation and sharing policies, researchers are requested to notify E-Defense (edef@bosai.go.jp) with the subject line "E-Defense test: soil-underground structures" when interested in using this data set and establish a collegial collaborative relationship as well as to obtain permission for official usage and reproduction of Figures and other results. Proper acknowledgements of the project's governmental funding obtained in Japan and the E-Defense research facility is appreciated. Assistance in accessing and using the data set will also be provided by the first author if desired.

Instrumentation: The Instrumentation folder holds all information related to the sensors installed around the specimen. Its general layout (i.e., description of location with respect to a global coordinate system) follows the former NEES project warehouse format. 25 instrumentation plans in jpeg format for each individual element (including subsections thereof) are stored in the Sensor layouts sub-folder.

Photos and Videos: The Photos and Videos folder contains a variety of visual tools depicting the shake table, the test setup, construction, structural elements, instrumentation, specimen damage and a series of shaking videos recorded during the event.

Specimen: The Specimen folder stores information about the test specimen and the specimen materials. For this experiment, a description of the soil properties is included.

2.7. Summary

This chapter presents a large-scale shake table testing program of vertical and horizontal underground structures embedded in a two-layer soil system. Load applications include the JR Takatori motion scaled to 50% and 80% acceleration magnitude. An important set of test data are archived at the NHERI Design Safe Data Depot, and can be found under DOI:10.17603/DS21C78 (Lemnitzer et al. 2016). The objective of this test is to provide data that help our understanding of soil-structure interaction mechanism among densely configured subsurface structures and publicize data records for implementation beyond the initial use and interpretation by the project team. The following list, presents the various aspects of the performed experiments which have been studied through different research projects (e.g., Towhata et al. 2014, Kawamata et. al. 2016, Keykhosropour and Lemnitzer 2019):

1. Study the overall dynamic performance of the structural components in the container. This includes global and local damage observed around the test specimens, that is, non-ductile deformations, rotations (e.g., cut and cover tunnel), soil-settlement induced gapping and local yielding at joints, component failure, and connection failure (e.g., bolt and weld failure).

2. Evaluation of the effectiveness of joint flexibility in reducing stress demands on connecting structures, by evaluating the strain and displacement measurements around the connection interface.

3. Assessment of the effects of impedance at the rock/soil interface on the performance of tunnel elements in comparison with the observed damage following the load application.

4. Evaluation and analysis of the seismic soil pressure records during the ground motion application and comparison with existing analytical models used in prediction of seismic soil pressures (presented in chapter 4 of this dissertation).

Chapter 3

Implementation of soil pressure sensors in large-scale soil-structure interaction studies

3.1. Introduction and review of existing geotechnical instrumentation

As technological capabilities have advanced, the instrumentation used in geotechnical applications and testing has also improved. Various devices have been developed by practitioners and researchers to measure contact pressures, many of them still being used today (Ahmed and Meguid, 2009). These devices range from stiff pressure cells, which measure contact stresses at specific locations, to tactile sensors, which measure soil stresses against structure across a continuous surface area. Fiber optic sensors have also been implemented in pressure measurements (Legge et al., 2006; Correia et al., 2009), but a full discussion is beyond the scope of this manuscript. Descriptions and applications of two different types of available and currently used contact pressure instrumentation in geotechnical applications are summarized below.

3.1.1. Soil pressure sensors

Soil pressure cells (SPC) are commonly used to measure stresses within a soil mass or at the face of structural elements using embedded or contact SPCs, respectively. SPCs commonly contain a sensing face against which the pressure is applied and an internal sensing mechanism that translates the differential change of the recorded units into corresponding pressures. Two major groups of SPCs are commonly distinguished: load cells using the force-balance principle (i.e., hydraulic and pneumatic cells) and diaphragm pressure cells (i.e., electric transducers that use the resistance strain gauge or vibrating wire principles) which are more commonly used in

geotechnical applications. Figure 3.1a depicts a schematic of the simple principle behind the diaphragm load cell (strain gauge and vibrating wire based).

Although contact SPCs still experience limitations associated with typical load cell type of instrumentation, the technical literature particularly highlights the complexity of embedment cells. According to Hvorslev (1976), Selig (1964), Weiler and Kulhawy (1982), and Dunnicliff (1988), the soil-to-cell stiffness and aspect ratio are two major issues that affect the measurements of embedment pressure cells and may cause under-registration (active arching) or over-registration (passive arching) of the cell. When the modulus of the pressure cell is greater than the modulus of the soil material, the stress sensed by the pressure cell is greater than the stress in the free-field, which is referred to as passive arching. In turn, a pressure cell with a sensing stiffness less than its surrounding soil material will sense a stress that is less than the stress in the free-field, which triggers active arching (Kogler and Scheidig 1927, Taylor 1945, Monfore 1950, Loh 1954, Askegaard 1963; and Tory and Sparrow 1967). As a general recommendation, Weiler and Kulhawy (1982) and Dunnicliff (1988) suggest that errors associated with stiffness compatibility issues can be minimized by designing instrumentation for high stiffness, as well as aspect ratios of less than 1:10. According to Selig (1964), the embedment pressure cell is not a material element but a structure whose response is dependent on the stress distribution and the total load. Thus, a proper calibration against soil material is needed. Dunnicliff (1988) suggests that, unless an embedment pressure cell is to be used in soft clay, fluid pressure calibrations are generally insufficient, and each cell should be calibrated in a calibration chamber with dimensions of at least three, and preferably five, times the diameter of the cell using the soil in which it will be embedded. Based on Terzaghi (1943) and Mason (1965), who investigated active and passive arching, respectively, the maximum thickness of the soil that is affected by the presence of a cell is three to

four times the cell's diameter in active arching and one sensor diameter in the passive condition. Therefore, it is recommended to calibrate embedment pressure cells against soil material with a thickness of two to three times the diameter of the cell.

When using contact SPCs, primary concerns include: having a reasonable degree of sensitivity, a suitable aspect ratio of the cell, an adequate sensing area, a minimum sensitivity to non-uniform bedding, and a method of installation that will not alter the state of stress at the interactive face between the soil and the structure. Several of these aspects were studied in early literature by Hvorslev (1976), Selig (1964), and Weiler and Kulhawy (1978, 1982). In addition, structural conformity (i.e., similarity in stiffness between the carrier structure and the embedded pressure sensor) is desired.

Other factors that affect the measurements by the contact pressure cells include the number of cells, temperature changes, and irregularity of surface of the structure. Coyle and Bartoskewitz (1976) and Felio and Bauer (1986) investigated the effect of temperature changes on the performance of the hydraulic pressure cells mounted on a precast panel retaining wall and a bridge abutment, respectively. The researchers concluded that temperature changes have a significant effect on the performance of hydraulic pressure cells, and the measurements from the cells should be modified using correction factors. On the contrary, diaphragm pressure cells are not influenced by the temperature changes, and corrections for temperature changes are not required for these cells (Dunnincliff, 1988). DiBiagio (1977) studied the effect of surface irregularity on the measurements of contact pressure cells by installing cells at different locations along a corrugated sheet pile (i.e., protruding and indented corrugations), concluding that surface irregularity could result in considerable errors. They suggested that the best estimate of the stresses could be made by averaging the measurements from the pressure cell. A full description of different types of

embedment and contact soil pressure cells, installation methods, and the factors affecting measurement accuracy can be found in works by Dunnicliff (1988) and Bhatia and Blaney (1991).

During a study of soil-structure interaction problems, Lazebnik and Tsinker (1997) investigated practical approaches of developing, calibrating, and installing various types of soil pressure sensors, and emphasized the influence of cell flexibility and the potential consequences of near-field stress alterations (i.e., soil arching). Soil arching around the sensor will lead to a reduction in the actual applied pressure to the cell, which precipitated the development of the null soil pressure cell. Due to their relatively infinite stiffness, null pressure sensors are capable of minimizing cell deflection, which results in the best performance among all load cells. Jennings and Burland (1960) proposed the early principles of null pressure cells. Talesnick (2005) developed a null pressure sensor based on null method concepts proposed by Doebelin (1990). Talesnick et al. (2008) implemented this sensor in a research study of buried scaled model structures subject to compressive loading from the soil surface. Reasonable soil pressure measurements were obtained.

To date, the use of soil pressure cells remain contentious. The need to install many load cells to obtain measurements of soil stress required to develop a pressure distribution profile along the structure's length is an undesirable feature of this type of device. In addition, the physical size of some pressure cells and their inherent rigidity can potentially make SPCs unsuitable for stress measurement on very flexible structures (Ahmed and Meguid, 2009) or challenge a realistic understanding of average stresses on an element (e.g., specifically when the sensing area is small). However, despite the aforementioned limitations, load cell based SPCs provided valuable means for the measurement of contact stress and for soil-structure interaction analyses in different fields of geotechnical engineering and are consistently integrated in recent research studies (e.g., in

conjunction with shake table testing (Luzhen et al., 2010; Kawamata et al., 2012; and Chen et al., 2012), analysis of laterally loaded piles (Janoyan and Whelan, 2004), and shallow foundations (Star et al., 2015).

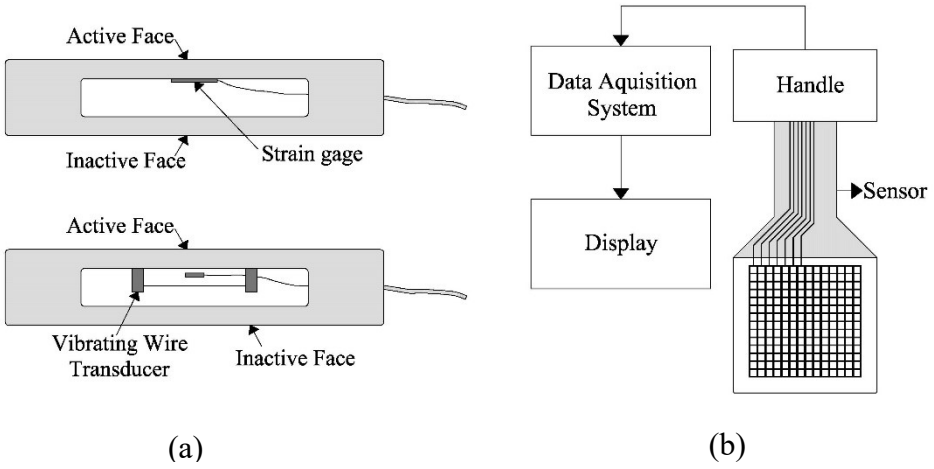

Figure 3.1. Basic schematic of pressure sensors: (a) diaphragm pressure cell, (b) tactile sensor

3.1.2. Tactile sensors

Most commonly used tactile pressure sensors consist of a polymeric sheet encapsulating an embedded array of small sensing units (i.e., sensels) capable of measuring the magnitude and distribution of stresses normal to the sheet surface (Figure 3.1b). By measuring the stresses at a large number of points in close proximity to each other, data recordings provide a relatively accurate measurement of stress distribution (Paikowsky et al. 2006; Palmer et al., 2009). The performance of these sensors is based on the change in electrical resistance in the sensels due to applied forces, and the change in resistance is then correlated to pressure through a calibration relationship. As compared to a conventional pressure sensor, the main advantage of a tactile pressure sensor is its ability to provide a measurement of the distribution of stress across a relatively large surface and of different geometries. The major disadvantage of tactile sensors is

that the sensor must be recalibrated for different test conditions. Moreover, these sensors are vulnerable to moisture (Ahmed and Meguid, 2009) and creep (Büscher et al., 2015), which may limit their usage in some geotechnical applications that require monitoring over a long period.

Nevertheless, since their first geotechnical applications in 1997, tactile sensors have been deployed in a variety of research studies. Examples of tactile sensor use include model scale deep foundation testing investigating stress distribution along the pile foundations (Helm and Suleiman, 2012; Suleiman et al., 2014; and Lin et al., 2015), centrifuge modeling (Springman et al., 2002; Gillis et al., 2015), and studies of ground rupture and horizontal ground displacement and their effect on buried pipelines (O'Rourke and Bonneau, 2007; Ha et al., 2008; O'Rourke et al., 2008; and Palmer et al., 2009). Other studies have investigated specific features and influencing factors relating to the tactile sheet itself. Paikowsky et al. (2006) assessed the influence of grain size relative to sensel dimension, and the researchers concluded that larger grain sizes (e.g., coarse sands and gravels) result in singular contact pressure spikes between areas of no contact, while stress measurements are smoother for finely graded soils (e.g., fine sands and silts). Palmer et al. (2009) investigated the effects of external shear and creep on the performance of tactile sensors, proposed different techniques to minimize the effect of external shear and proposed a measurement method accounting for the sensor's time-dependent performance due to its viscoelastic characteristics. Gillis et al. (2015) proposed a dynamic calibration procedure for the deployment of tactile sensors in centrifuge experiments.

3.2. Motivation for sensor development

Motivated by a study of passive pressures behind a bridge abutment structure (Stewart et al., 2011), a stiff prototype pressure sensor with a large sensing area was designed and manufactured

for deployment in a series of large-scale tests. The main objectives of the sensor design were to (1) obtain a large sensing area to avoid a pressure concentration due to single large grains on small area sensors, (2) create a homemade cell assembly that provides flexibility and facilitates the needs of the application in terms of material and capacity, and (3) create a simple, robust, and cost-efficient alternative to commercially available products. According to Talesnick (2005), new developments of pressure sensors in geotechnical engineering are not frequently published after about 1985. The design of these newly developed pressure cells and their different calibration procedures are described, hereafter.

3.3. Design of the pressure sensor

A schematic and photographs of the developed pressure cell are depicted in Figures 3.2 and 3.3, respectively. The sample pressure cell assembly has an outside diameter of 10 cm, and the sensing face has a diameter of 9.5 cm, which equates to a sensing area of about 78.54 cm^2.

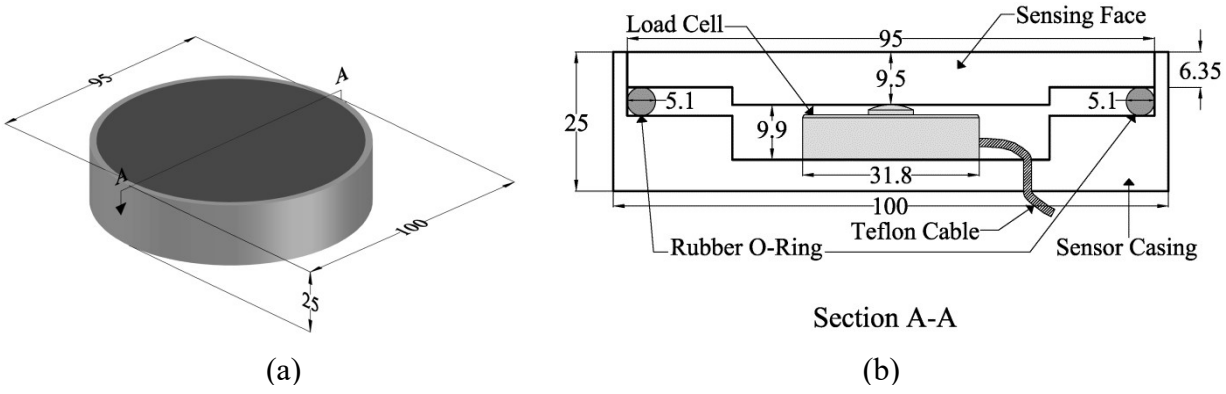

Figure 3.2. Schematic of the pressure sensor: (a) three-dimensional view, (b) cross section (dimensions in mm)

One of the main advantages of the proposed assembly is the flexibility in material choice for the sensors. The external sensor housing can consist of a wide range of materials depending on the stiffness of the structure to which the sensors will be affixed. Ideally, the modulus of elasticity of the material used for the sensor housing should provide a similar flexibility as the host material. In the E-Defense project, the sensor housing was made of aluminum which complies with the material of the model structures in this study. The thickness of the housing at the location of the sensing area is 25 mm. The sensing face consists of a steel plate (i.e., sensing plate) with a thickness of 6.35 mm along the edges, where the plate rests on stiff rubber bearings, and about 9.5mm in the center, where the plate is in continuous contact with the load cell. The stiffness of the sensing plate ensures no deflection in sensing element, which reduces or prevents arching effects from the surrounding soil. Therefore, the sensor calibration is not sensitive to the specific soil material. A high precision, commercially available load cell was installed and rigidly connected to the center of the housing. The sensing face is in intimate contact with the load cell, rests on two stiff rubber O-rings on the side to minimize potential tilting, and is flush with the housing. In addition, and depending upon the application, the load cell cable can exit the housing at the bottom or through the side of the pressure cell. This provides additional flexibility to accommodate potential constraints of the installation location. The cable consists of a 4-conductor wire with standard dimensions (e.g., 26 AWG) that provides input and output voltages. The sensor was powered with an input voltage of 10V per the load cell manufacturer's recommendations. Photographs of the assembled pressure sensor are shown in Figure 3.3.

Figure 3.3. Photo of pressure cell (left and middle), and pressure cell with adapter ring (right)

A primary advantage is the user-based choice of load cell capacity upon manufacturing. The load cell capacity can be selected based on the expected range of pressures to be measured at the contact surface and or exchanged if a high pressure is to be expected. In the E-Defense project, the load cell capacities ranged from 1110 N (250 lb) to 2220 N (500 lb) and translated into pressure capacities of 144 kPa (3 ksf) and 288 kPa (6 ksf), respectively. The data sampling capacity can be adjusted to the specific type of testing: for the static load tests, sampling frequency was 1 Hz, and for the dynamic testing, the pressures were recorded at a frequency of 200 Hz. The limit of the sensor sampling frequency is dictated by the limitation of the researcher's data acquisition system and in the case of dynamic loading, affected by the Nyquist frequency (i.e., highest frequency of the signal) to avoid aliasing. The minimum sensor resolution depends on the internal load cell. In this application, forces as low as 0.002 N can be captured, which translates to pressures as low as 0.25 Pa.

The installation of the sensor itself can be adapted to the needs of each specific application. The load cell can be embedded in the carrier structure (e.g., though a cut-out), or, alternatively, can be used with an adapter ring if installed inside a hollow structure, as in the E-Defense project.

3.4. Sensor calibration

Two pressure sensors with load capacities of 1110 N and 2220 N corresponding to maximum pressure ranges of 144 kPa and 288 kPa, respectively, are discussed hereinafter. The accurate calibration factor of the internal load cell prior to its installation into the pressure cell was provided by the manufacturer. However, calibration of the assembled system (e.g., housing, sensing phase, O-rings, etc.) was required prior to the sensor's use. Each of the sensors was calibrated statically and dynamically. The static calibration was performed twice: (1) basic loading up to 67% of the sensor's capacity using dead loads from weighted steel plates, and (2) compression loading up to full pressure capacity (100%) from a universal testing machine (UTM). The dynamic calibration was performed using a linear mass shaker to determine the sensor's frequency-dependent response. A brief discussion of the calibration testing is provided below.

3.4.1. Static calibration

The loading schedule for the static calibration performed using the static weights and the compression testing machine is provided in Table 3.1. Photographs of the different load testing configurations are shown in Figure 3.4. The sensors were calibrated using a stepped loading sequence. For the static calibration performed using static weights (Figure 3.4a), the loading was applied in five relatively equal increments up to about 67% of the cell's capacity, and then unloaded in the reverse order. For the static calibration performed using the compression testing machine, the loading was applied in four relatively equal increments up to about 100% of the cell's capacity, and then unloaded in the reverse order. To assess the effect of load shape on the response of the sensor, three different loading configurations were applied to each sensor during calibration testing with the UTM: (1) a point load (Figure 3.4b), (2) a distributed load using a two-inch

diameter plate between the reference cell and the pressure cell (Figure 3.4c), and (3) a distributed load using a four-inch diameter plate between the reference cell and the pressure cell (Figure 3.4d).

Table 3.1. Loading schedule for static calibration using static weights and using the compression testing machine

Step No.	Static Weights		Compression Testing Machine			
	Incremental (kN)	Total Applied (kN)	Incremental (kN)	Total Applied (kN)	Load Transition Time (s)	Duration of Hold (s)
0	0	--	0	0	-	-
1	0.14596	0.14596	0.267	0.267	1	3
2	0.14774	0.29370	0.267	0.534	1	3
3	0.14685	0.44055	0.267	0.801	1	3
4	0.14774	0.58829	0.267	1.068	1	3
5	0.14774	0.73603	-0.267	0.801	1	3
6	-0.14774	0.58829	-0.267	0.534	1	3
7	-0.14774	0.44055	-0.267	0.267	1	3
8	-0.14685	0.29370	-0.267	0	1	-
9	-0.14774	0.14596	-	-	-	-
10	-0.14596	0	-	-	-	-

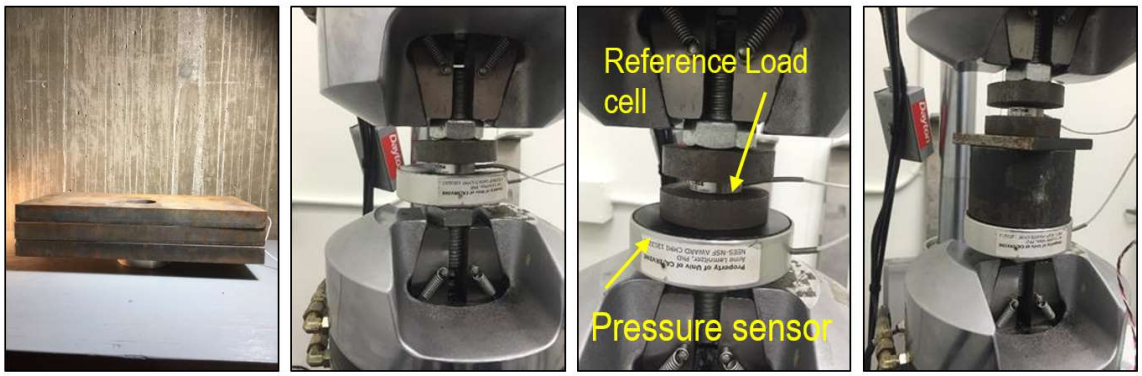

(a) (b) (c) (d)

Figure 3.4. Photographs of the different loading configurations: (a) using static weights, (b) point load in UTM, (c) distributed loading using a two-inch diameter plate in the UTM, and (d) distributed loading using a four-inch diameter plate in the UTM

An average voltage response was measured for each increment of loading or unloading. Voltage time histories were correlated with the corresponding applied loads, and calibration curves

(i.e., voltage-load relationships) were derived. For both cells, the voltage-load relationship was found to be linear within the applied load range. The results indicate very consistent pressure measurements among the recordings for each of the loading configurations. The data depicted in Figure 3.5 include the measurements of a reference load cell installed between the UTM load application point and the response of the pressure cell as shown in Figure 3.4b-d. The results indicate in the load-time histories for the 144 kPa pressure cells are nearly identical throughout the measurement range (Figure 3.5), and similar results were observed for the 288 kPa pressure sensor.

A graphical summary of the calibration relationships for the 144 kPa and 288 kPa sensors for each of the four loading configurations is shown in Figure 3.6. The average static calibration relationship for each sensor was determined as the average linear trend line of the four loading configurations and is represented by a dashed line (Figure 3.6). As can be seen from Figure 3.6, the calibration factor obtained from the manual testing with weighted plates was minimally larger (4 %) compared to other calibration methods, particularly for the 144 kPa sensor. This difference can be attributed to random errors, including the physical setup of this calibration and the accuracy in predetermining the weight of the applied loads as well as the user-handling procedures. This error has been eliminated during the calibration of the 288 kPa pressure cell.

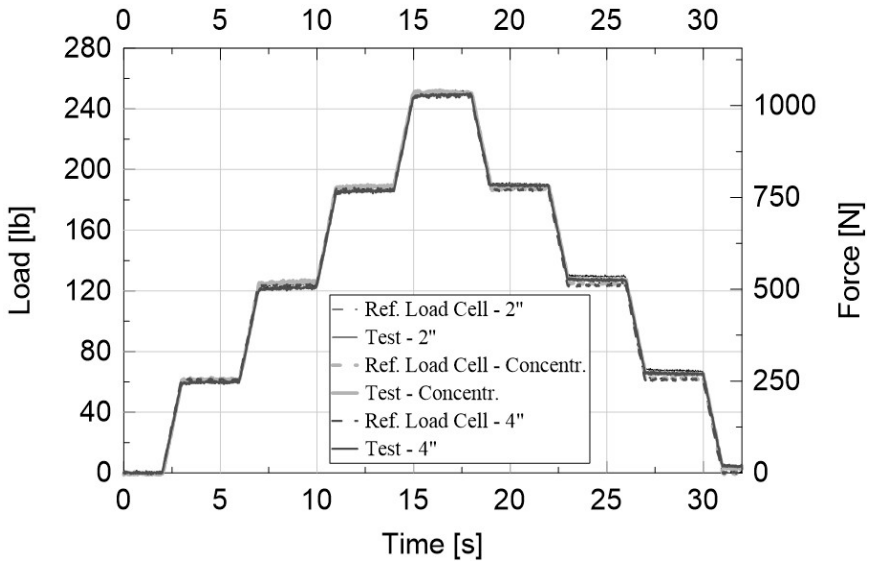

Figure 3.5. Load-time histories for 144 kPa sensor for different load configurations using UTM

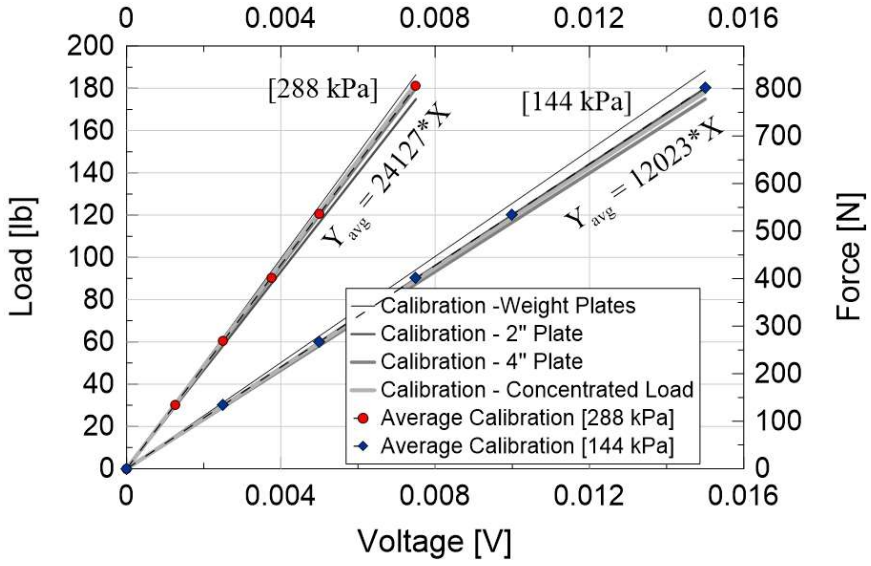

Figure 3.6. Calibration relationships for the 144 kPa and 288 kPa sensors for the different static loading configurations

3.4.2. Dynamic Calibration

Each sensor was calibrated dynamically in the structural engineering laboratory using a linear mass shaker to determine the sensor's frequency-dependent response. As shown in Figure 3.7, the mass shaker was mounted above the sensor and oriented vertically. The shake table provided

dynamic excitation through a 2.5 cm thick steel plate, which was used to ensure that a uniformly distributed dynamic pressure was applied to the sensor. The sensor was affixed to a 5 cm thick steel plate to prevent movement during the excitation and to ensure there was no eccentricity in the applied loading. Two accelerometers were used to measure the dynamic motions during the testing. Accelerometer No. 1 was attached to the moving part of the shake table and was used to measure the inertial acceleration induced by the applied motion, whereas Accelerometer No. 2 was attached to the static frame of the shake table and was used as a reference that could be used to remove any additional inertial forces from the non-moving part of the shaker (Figure 3.7).

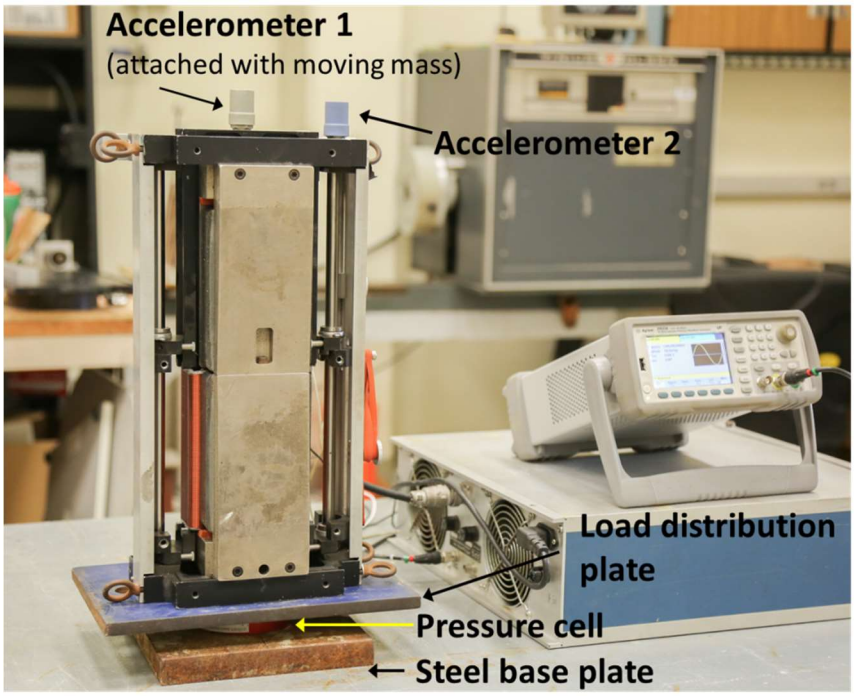

Figure 3.7. Setup for dynamic calibration with vertically oriented shake table

The sensors were calibrated using a stepped sinusoidal excitation, where the frequency was increased from 2 Hz to 16 Hz in 2 Hz increments. These frequencies deemed suitable to capture typical ranges of earthquake ground motions. Each increment of frequency was maintained for

approximately 20 seconds, resulting in a total duration of excitation of about 160 seconds. The applied force on the sensor was computed by multiplying the measured acceleration of the moving plate (Accelerometer No. 1) by the mass of the moving plate (i.e., M_{moving} = 3.083 kg) minus the force observed from Accelerometer 2 (negligible). Data were recorded using the same sampling frequency, f_{samp}, of 200 Hz. The unfiltered voltage -time histories for the 144 kPa and 288 kPa pressure cells are shown in Figure 3.8a (first row), respectively. Please note that the selected amplitude for the 2Hz motion and the higher frequency motions was different to evaluate the capability of the sensor to capture a broad range of frequencies and amplitudes. An amplitude of 40 mVpp was used for the 2Hz loading, while an amplitude of 100 mVpp was selected for frequencies of 4Hz and higher. The recorded data were filtered by first transforming the signal from the time domain to the frequency domain using the Fast Fourier Transformation (FFT), and then applying a low-pass, 8^{th} order (n_f = 8) Butterworth filter to remove frequencies above 16 Hz, i.e., all frequencies outside the applied frequency range were eliminated. After the filtering was completed, the signals were transformed back into the time domain using the inverse FFT. The static calibration factor was applied to the voltage data, and the filtered force-time histories are shown in Figure 3.8b (second row) for the 144 kPa (left) and 288 kPa (right) pressure cells, respectively.

The Fourier force amplitude for each of the filtered data set (i.e., pressure cell and accelerometer) was normalized by its maximum Fourier amplitude, and is shown in Figure 3.9 for both pressure cells.

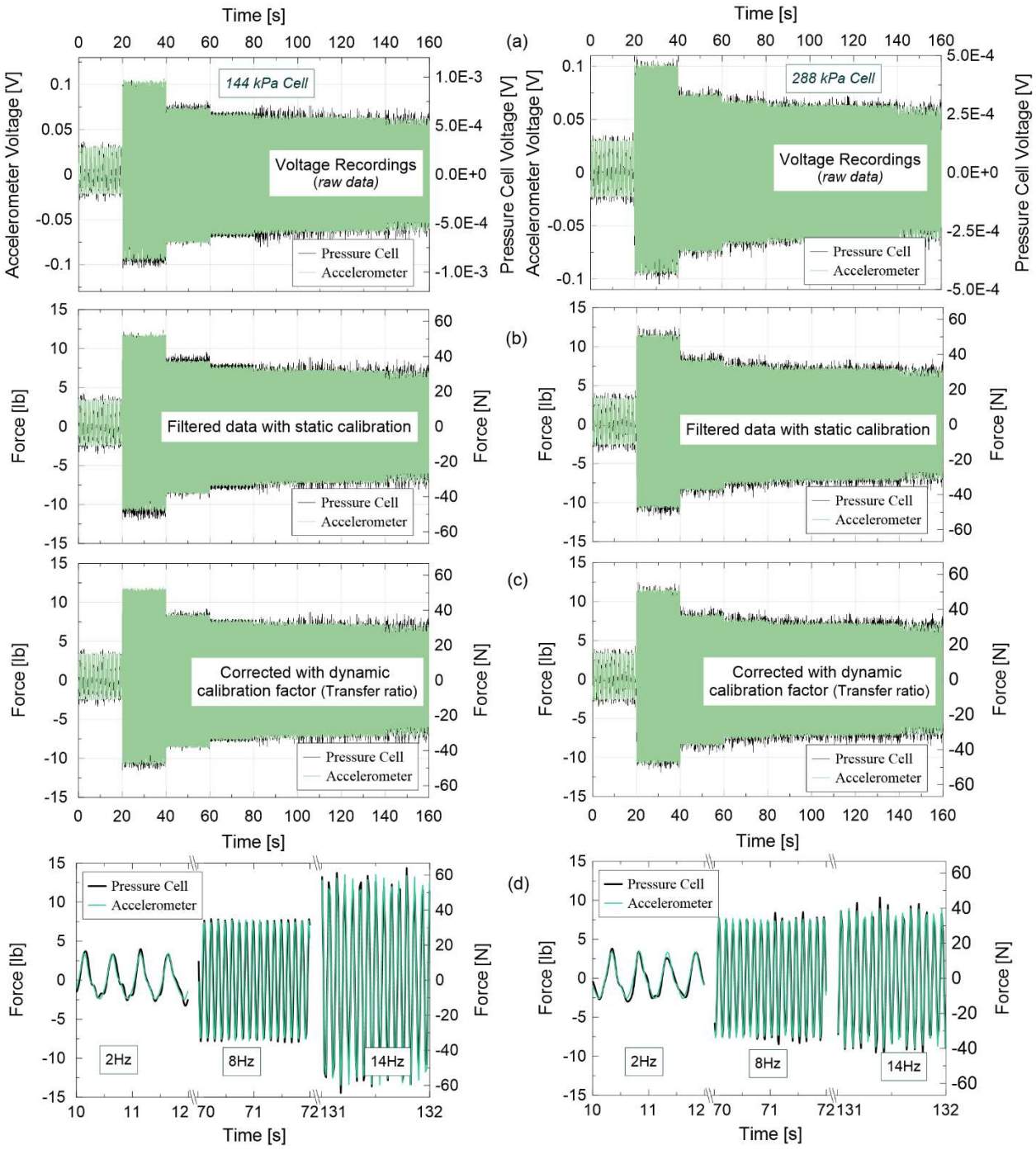

Figure 3.8. Pressure cell response to dynamic loading: 144 kPa cell (left column) and 288 kPa cell (right column) for unfiltered, raw (top row), filtered (second row), dynamically calibrated (third row) dynamic, and enlarged signals (fourth row)

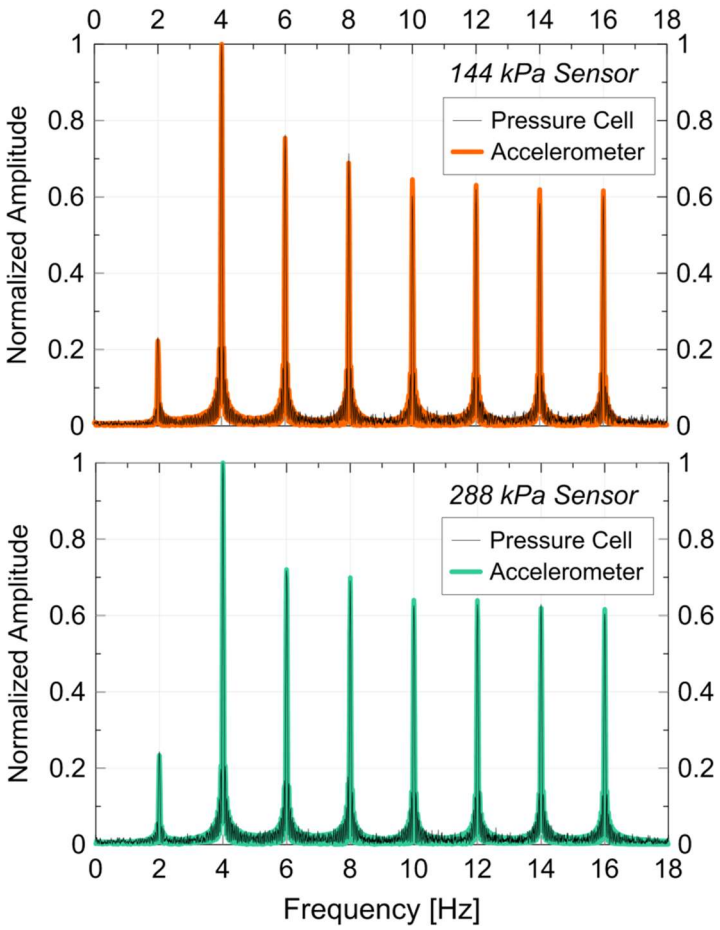

Figure 3.9. Normalized Fourier amplitudes

Following Gillis et al. (2015), a frequency dependent transfer function (i.e., a transfer ratio) between the accelerometer and the pressure cell was obtained by dividing the Fourier force amplitude of the accelerometer, $P_{accelerometer}$, by the Fourier force amplitude of the pressure cells ($P_{pressure\ cell}$) at each of the frequencies of the applied motion (i.e., 2 Hz, 4 Hz, 6 Hz, etc.), as expressed in Eq. 1.

$$TF(f) = \frac{|P_{accelerometer}(f)|}{|P_{Pressure\ cell}(f)|} \quad (1)$$

The variation of the transfer ratio with the loading frequency for the 144 kPa and 288 kPa sensors are shown in Figure 3.10. The best fit to the transfer ratios was obtained using a second-degree polynomial function, as shown by the dashed line in Figure 3.10. It can be seen that the dynamic transfer ratio is extremely close to 1.0, indicating that differences between applied and measured pressures were small (i.e., ≤ 6.3% for the 250 lb sensor and < 4.6% for the 500 lb sensor). This also confirms that the sensor assembly has little impact on the pressure recordings and that the sensor responds consistently across a variety of applied frequencies.

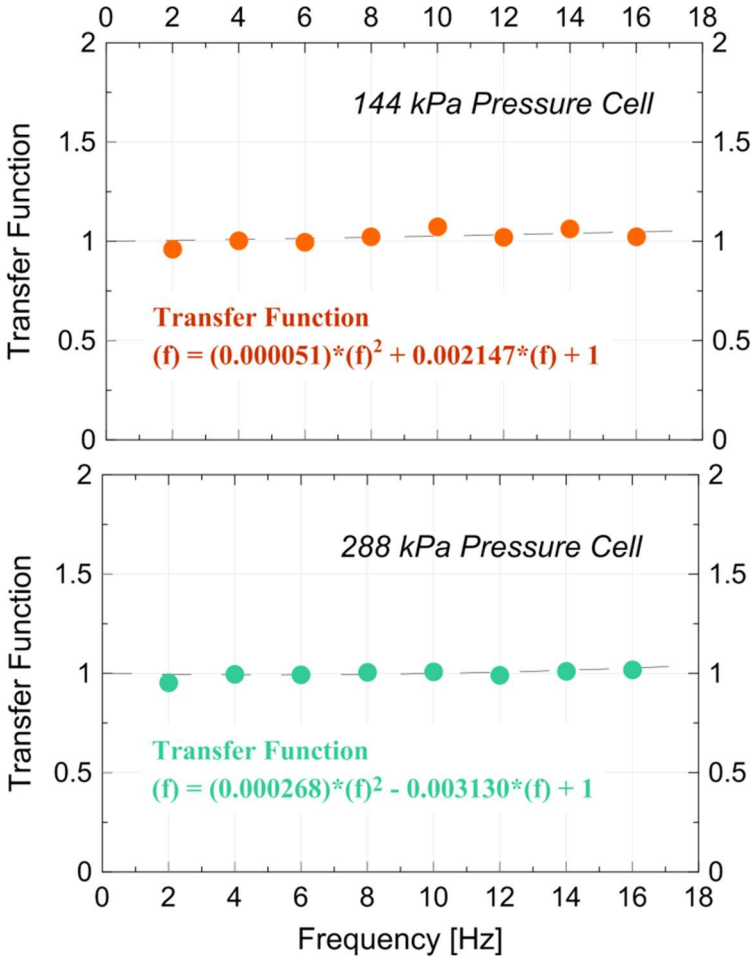

Figure 3.10. Transfer function between applied and recorded acceleration measurements

After obtaining the transfer function for each pressure sensor, the corrected sensor response can be obtained by multiplying the pressure sensor data record with the value of the corresponding transfer ratio, as expressed in Eq. 2. In this case both data sets are very similar as the transfer ratio is almost 1.0 across the entire frequency range.

$$P_{\text{pressure cell}-\text{corrected}}(f) = TF(f) \times P_{\text{pressure cell}}(f) \quad (2)$$

The corrected Fourier force amplitude spectra obtained using Eq. 2 was transformed back into time domain using an inverse FFT. Figure 3.8c (third row) presents the dynamically calibrated force time histories of the pressure sensors. Very good agreement can be observed for both pressure sensors. Figure 3.8d depicts a close-up version of several time intervals during the application of the 2 Hz, 8 Hz and 14 Hz frequencies. This zoomed graph is used to illustrate the ability of the sensor to capture the applied amplitudes within reasonable accuracy.

3.5. Soil-sensor stiffness compatibility and loading/unloading nonlinearity

As it was explained in section 3.2.1 of this dissertation, soil-to-cell stiffness and aspect ratio are two major issues that affect the measurements of embedment pressure cells and it is recommended to calibrate them against soil material with a thickness of two to three times the diameter of the cell. Dunnicliff (1988) suggested that the aspect ratio and soil/cell stiffness ratio are not among the parameters that predominantly affect the performance of contact pressure cells and recommended that the calibration of a contact cell be performed under fluid pressure only. In turn, Talesnick (2005) and Talesnick, Ringel, and Avraham (2014) indicated that fluid calibration will not provide realistic values compared with measurements obtained in soil, hereby referring to both types of sensors. Selig (1980) suggests calibrating this type of pressure cell against soil

material to be beneficial but declares it as “unessential” for contact pressure cells in comparison with embedment pressure cells.

The amount of deflection of the sensing element, is another issue with soil pressure sensors which could result in under-registration (active arching) during loading as well as significant nonlinear response and hysteresis behavior during unloading.

The newly designed pressure cell presented in this research is a contact pressure cell. Considering the high stiffness of the load cell (i.e., sensing element) used in this pressure cell as well as the stiffness of the external housing and its compatibility with the carrier material, it is believed that the soil stiffness and soil arching around the sensor are not primary problems for this pressure cell. However, even when using the stiffest load cell product available on the market, it may still experience deflection under the applied pressures. Therefore, due to this issue and also controversy of opinions within the technical literature regarding the effect of soil-sensor stiffness ratio on the contact pressure cells, the response of the designed pressure cell was examined against soil materials with varying thicknesses under static loading/unloading cycles.

Figures 3.11 and 3.12 show a calibration setup and measured calibration data obtained by applying dead loads on the sensor directly, as well as with soil layers consisting of sand and clay materials with varying thicknesses (i.e., 1cm, 2cm, and 3cm). The diameter of the sensing load button of the pressure cell was 8.10 mm, resulting in a ratio of the soil thickness-to-sensing diameter equal to about 1.23, 2.47, and 3.70 for the three thicknesses of soil used. The calibration test setup, as shown in Figure 3.11, followed recommendations by Tognon, Rowe, and Brachman (1999) to reduce the amount of side friction in the setup. As such, a stiff plastic tube with an inside diameter of 10 cm was furnished with a greased polyethylene (i.e., Teflon) sheet with a thickness of 0.254 mm. The pressure cell was placed at the bottom of the tube. The loading was applied

through a circular steel plate placed atop the sensor, the soil layer, or both using steel weights (Pl. 1 through Pl. 7 in Figure 3.11) up to 68 % of the cell's capacity. Unloading was performed by removing the steel weights in a progressive sequence back to zero.

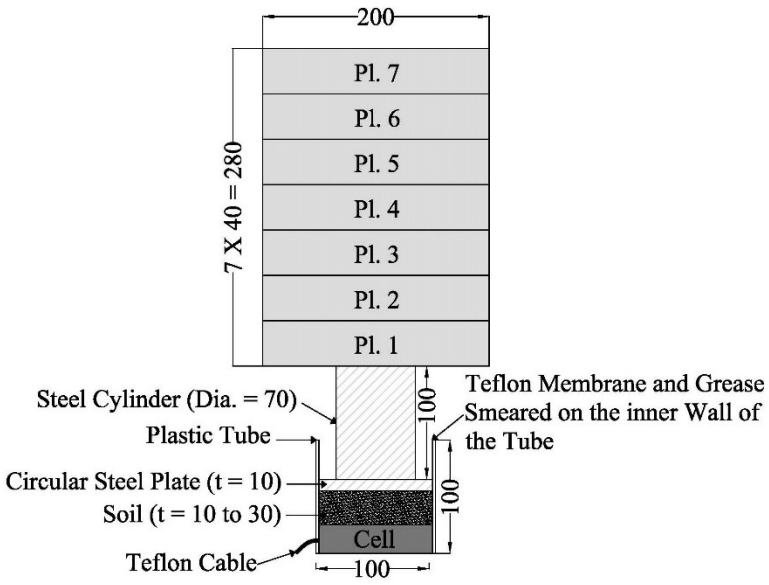

Figure 3.11. Calibration setup using static weights (all dimensions in mm)

The load–voltage calibration relationships for the loading and unloading conditions are shown in Figure 3.12. The difference between the loading and unloading voltage readings during equal load levels is 8.40 % for the clay soil and 12.47 % for the sand soil. The calibration relationship appears relatively linear for small thicknesses of soil. However, these differences increase with decreasing stiffness of the sensing element (i.e., if a less stiff pressure cell is used) or when the soil thickness is increased. Within the setup presented in Figure 3.11, the thickness of soil used was increased further to 60 mm and then again to 90 mm. For a soil thickness of 60 mm, the difference in the calibrations between loading and unloading ranged between 15 % and 18 %. This difference (or error) in the calibrations did not increase for the load application with 90 mm of soil.

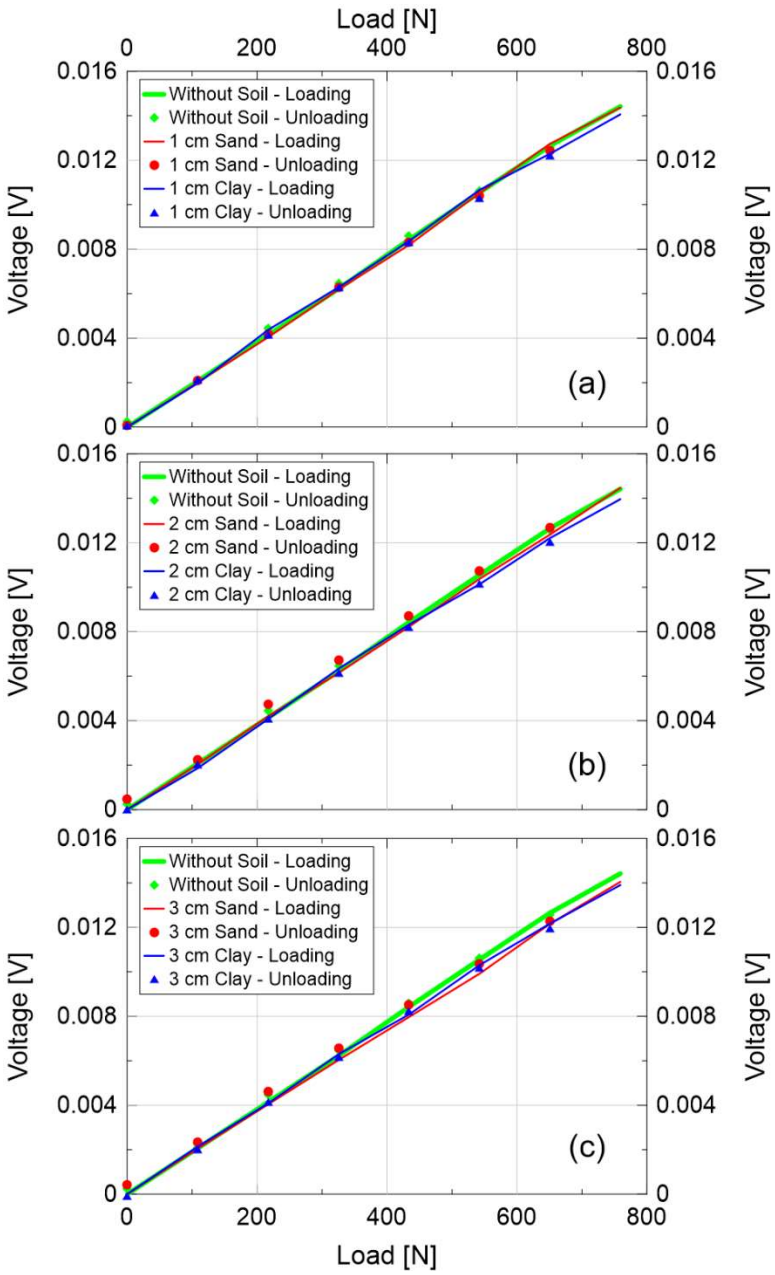

Figure 3.12. Calibration relationships for the pressure cell-soil thickness of (a) 10mm, (b) 20 mm, and (c) 30 mm

In some scientific and engineering applications, a calibration difference or error of 15 % to 20% may be excessive and highly unacceptable. However, in geoengineering and geoconstruction applications, in which readily available sophisticated instrumentation to provide accurate estimates of soil pressures is not currently attainable, limited or rudimentary monitoring systems provide

data with inherent errors. From a practical viewpoint, users and stakeholders may desire simple or commercially available sensor instrumentation, or both, to provide monitoring, which provide some level of measurement even with an inherent error and may be adequate given the availability of current technological capabilities.

3.6. Conclusions

The design, development, and calibration, of a simple, easily constructible, and robust soil pressure sensor are presented. One of the primary advantages of the sensor is its versatility, namely, the pressure sensor can be constructed with a housing material compliant with the stiffness of the structural element to which the sensors are being affixed, while the internal load cell can be selected so that it can accommodate the expected range of applied pressures during testing. In addition, the sensor response is relatively independent of soil type, condition, and stress history, and it is most suitable for soils with relatively even gradation, typical for most research experiments. The large sensing area has the benefit of reducing localization effects (i.e., large soil particles altering pressure measurements for sensors of small size) and minimizes misleading (i.e., enlarged) pressure magnitudes. The sensor is suitable for long-term monitoring, for which a corrosion protective coating for the sensor housing is recommended. For highly non-homogeneous soils (e.g., with large rock or gravel particles) for which highly concentrated pressures with large eccentricities are expected, use of the sensor may require additional calibration. For this use in these special instances, the authors are currently developing a second sensor prototype, which will be capable of accommodating compression and tension loading (resulting from eccentric loading).

3.7. Acknowledgments

The authors would like to acknowledge the assistance in static data calibration and the intellectual exchange with Dr. Eric Ahlberg. Dr. Sergio Carnalla is gratefully acknowledged for his help with the dynamic calibration in the UCI Structural laboratory. Prof. J. Stewart and Dr. Y. Kawamata, principal investigators and collaborators on the abovementioned projects, are recognized for their support and willingness to install the sensors for the pressure measurements presented herein.

Chapter 4

Experimental measurements and analytical comparisons

4.1. Introduction

The soil pressure data recorded on the vertical shafts used in the E-Defense shake table tests under 50% and 80% Kobe motions are used to assess the magnitude and distribution of seismic soils pressures on flexible vertical underground structures. While the shafts' model-scale dimensions resemble "pile-like" geometries, the shafts' prototype dimensions translate to geometries (i.e., widths) that are typical for traditional "retaining wall" elements. The question arises whether traditional soil pressure theories may be suitable to provide a rough preliminary estimate on the overall system performance.

In this chapter, upon a brief review of the instrumentation used in the analyses (i.e., accelerometers, and pressure cells), and characterization of the soil dynamic properties, general observations of tests are described and then obtained dynamic soil pressure data on flexible underground structures subject to 50% and 80% scaled Kobe ground motions are presented. Hereafter, the suitability of different analytical methods, such as traditional and recently developed limit-state and elastic approaches for both cohesionless and cohesive ($c - \varphi$) soils in predicting the seismically induced earth pressures, is examined. Thorough understanding of the seismic soil pressures recorded on these types of structures serves as basis for the numerical model development, model verification and extended parametric simulations that consider the 3D behavior of the underground systems (chapter 5 of this dissertation).

The general description of the test setup was presented in chapter 2 of this dissertation. A schematic of the test configuration is shown in Figure 4.1 with the vertical shaft utilized in the analyses highlighted.

4.2. Instrumentation utilized in the analyses

Of interest to this section is the instrumentation of the vertical shaft with the rigid joint (VSR), located on the left of the model layout in Figure 4.1 (see highlighted shaft). As it was described in chapter 2, this shaft was instrumented with 20 load-cell based pressure cells with two different capacities (i.e., 144 kPa and 288 kPa) (Figure 4.2). Details on this newly developed instrumentation and the calibration in static and dynamic regimes was presented in chapter 3 of this dissertation. Figure 4.2 presents the pressure sensor instrumentation along all 4 sides of the shaft. Side 3 had the most pressure cells installed; hence, data from this side is used for consecutive analyses and interpretation.

Additional instrumentation of interest consists of accelerometers arrays along the container wall and within the soil material as shown in Figure 2.6. Four accelerometers located at the surface of the shake table adjacent to the container walls were used to estimate the model input motion. Accelerometers along array 6 in Figure 2.6 (i.e., in the free field soil) were used to obtain the dynamic properties of the soil material.

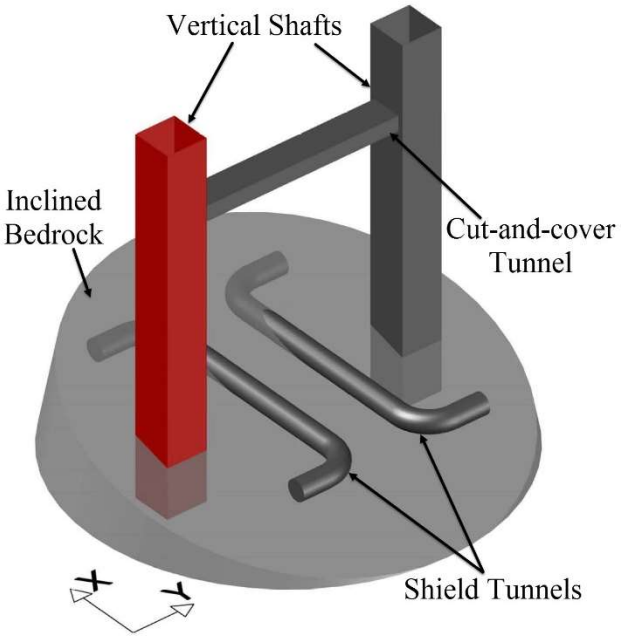

Figure 4.1. Schematic experimental setup

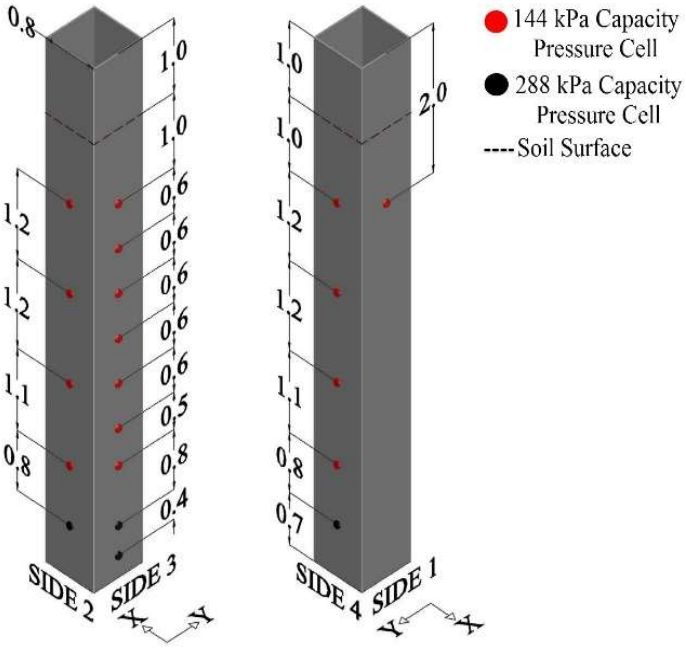

Figure 4.2. Instrumentation on the vertical shaft

4.3. Characterization of dynamic soil properties

The damping ratio ζ and shear modulus reduction G/G_{max} were determined using acceleration records from accelerometer array 6 (see Figure 2.6). Accelerations were filtered and baseline corrected prior to double integration. The required corner and cutoff frequencies were obtained using Fourier spectra analyses of the 50% and 80% Kobe motions at 0.3 Hz and 15 Hz, respectively. The acceleration records were bandpass filtered for frequencies between 0.3 Hz and 15 Hz. A baseline correction was performed using the method proposed by Yang and Lin (2006). A sample displacement time history obtained from accelerometer array 6 during the 50% Kobe motion is shown in Figure 4.3. Following Zeghal and Elgamal, (1994), Equation 1, shear strains (γ) were calculated by differentiating displacement records with respect to depth (z), using a second-order approximation between the accelerometers installed along the same vertical array.

$$\gamma(z_i) = \frac{[(u_{i+1} - u_i)\frac{(z_i - z_{i-1})}{(z_{i+1} - z_i)} + (u_i - u_{i-1})\frac{(z_{i+1} - z_i)}{(z_i - z_{i-1})}]}{(z_{i+1} - z_{i-1})} \quad (1)$$

where the index i is relative to the position of the central instrument and $i - 1$ and $i + 1$ to the upper and lower accelerometer, respectively. Sample shear strain time histories for the 50% motion is presented in Figure 4.3.

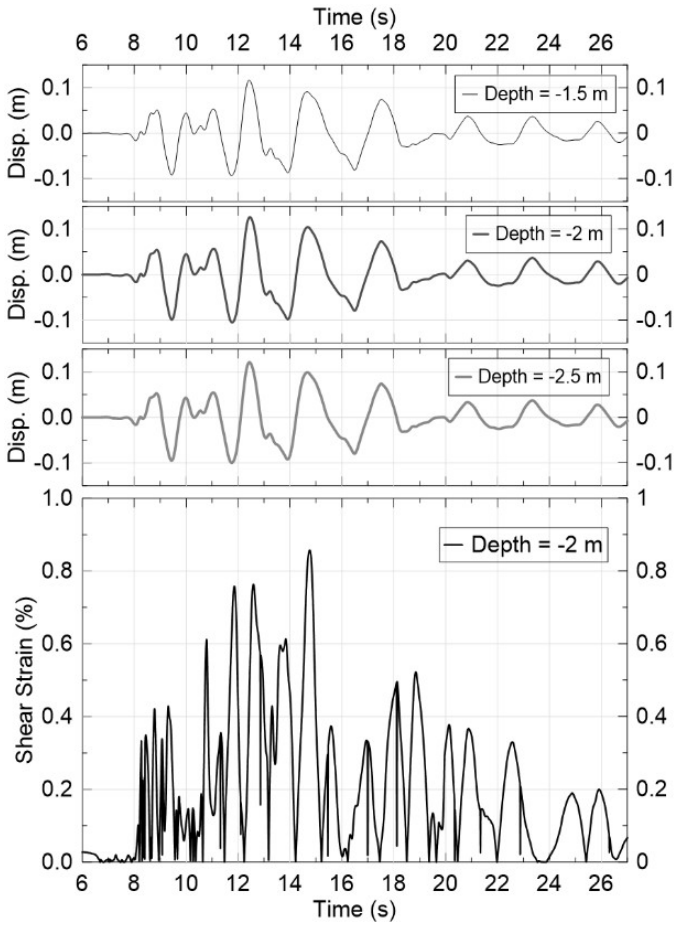

Figure 4.3. Sample displacement-time histories obtained from three consecutive accelerometers (top) and the corresponding shear strain for the 50% motion (bottom)

Following Bolt (1969), G/G_{max} and ζ were obtained using the bracketed duration approach in which a preset time frame of data records is considered. This time frame uses acceleration data above a threshold acceleration of 0.05g. Resulting equivalent uniform shear strains for the 50% and 80% motions were computed to be 0.182% and 0.387%, respectively.

To determine G/G_{max} and ζ, graphical solutions by Seed et al. (1986) suggested 28% and 12% for the 50% Kobe earthquake, respectively, and 18% and 16% for G/G_{max} and ζ for the 80% Kobe earthquake, respectively. The upper bound curve for sands was used for the results obtained above.

The fundamental frequency of the soil-wall system was computed using the dynamic response of pressure sensors during the sine sweep motions in x direction. This direction was of interest as

shaft side #3 (normal to the x-direction) will be used for consecutive pressure analyses and represents the most heavily instrumented shaft side. Sweep accelerations of 0.1 m/s^2 and 0.3 m/s^2 were selected, and pressure –time histories were transformed into the frequency domain. A transfer type of function, defined as the ratio of soil pressure amplitude to the amplitude of the corresponding base acceleration, was developed for each frequency level as is shown in Figure 4.4 for the 0.3 m/s^2 sine sweep motion. The fundamental frequency of the system was estimated to be 5.36 Hz.

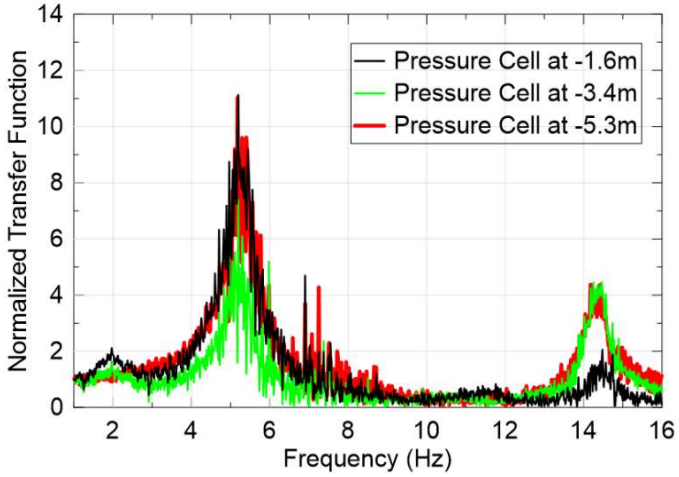

Figure 4.4. Transfer function spectrum for soil pressure cells obtained from the 0.3 m/s^2 sine motion

4.4. General test observations

This section presents sample data to illustrate different aspects of the tests. Upon test completion the specimen was inspected for damage development. Following the 50% Kobe earthquake, longitudinal cracks above the cut-and-cover tunnel indicated soil settlement of approximately $\leq$ 2 cm resulting from damage observed in the flexible joint connection, i.e., in the rubber-steel plate assembly. The damaged "flexible" joint was repaired and turned into a fixed connection for the subsequent ground motions. No damage was observed at the original rigid joint. The rigid joint was replaced with a connection that represents insufficient seismic strength, that is,

by replacing the original stainless steel bolts with resin bolts. No other issues were observed at this point and testing was continued. After the 80% Takatori shake, the specimen was investigated and dismantled. Surface cracking appeared on top of the cut-and-cover tunnel and a complete failure of the bolt connection at the joint with resin bolts (VSR) was manifested. Since underground structures typically work as networks, this type of local damage may induce malfunction of the entire network. In addition to the joint damage, a gap of 7.0 cm was observed underneath the cut-and-cover tunnel. This gap was induced through soil settlement and may results in addition joint damages in the prototype version. No gapping was observed around the shield tunnels, however detachment of some segments (i.e., joint failure along the tunnel axis) was observed. Figure 4.5 presents some of the damage observations. While most responses were in agreement with pre-test numerical studies, only one unexpected damage was observed, and is associated with the loosening of the bottom connection of one of the vertical shafts. This detachment occurred during the 50% shake and is unlikely to alter the system response as vertical uplifts were recorded to be less than 5.0 mm. Uplift motions during the 80% Takatori loading was higher and should be considered when evaluating the structural responses of the shaft (e.g., bending etc.) or when back-calculating soil pressures using the sensors on the flexible shaft (i.e., Japanese strain-gauge based instrumentation).

Figure 4.5. Observed damage after the 80% Takatori motion: (a) settlement beneath the cut-and-cover tunnel (photo taken after excavation), (b) failed resin bolts on the rigid joint, and (c, d) cracks at the ground surface parallel to the buried cut-and-cover tunnel

4.4.1. Sample measurements

Figures 4.6 and 4.7 exhibit sample displacement and settlement measurements recorded during the 50% and 80% scaled Kobe motions.

Input motions and overall specimen displacements: Figures 4.6a&b present the specimen input motions for the 50% Takatori EQ in the x and y directions recorded at the container table surface. The maximum x and y accelerations were recorded as 0.38 g and 0.32 g respectively. Values were averaged using four accelerometers placed on the table surface around the test specimen.

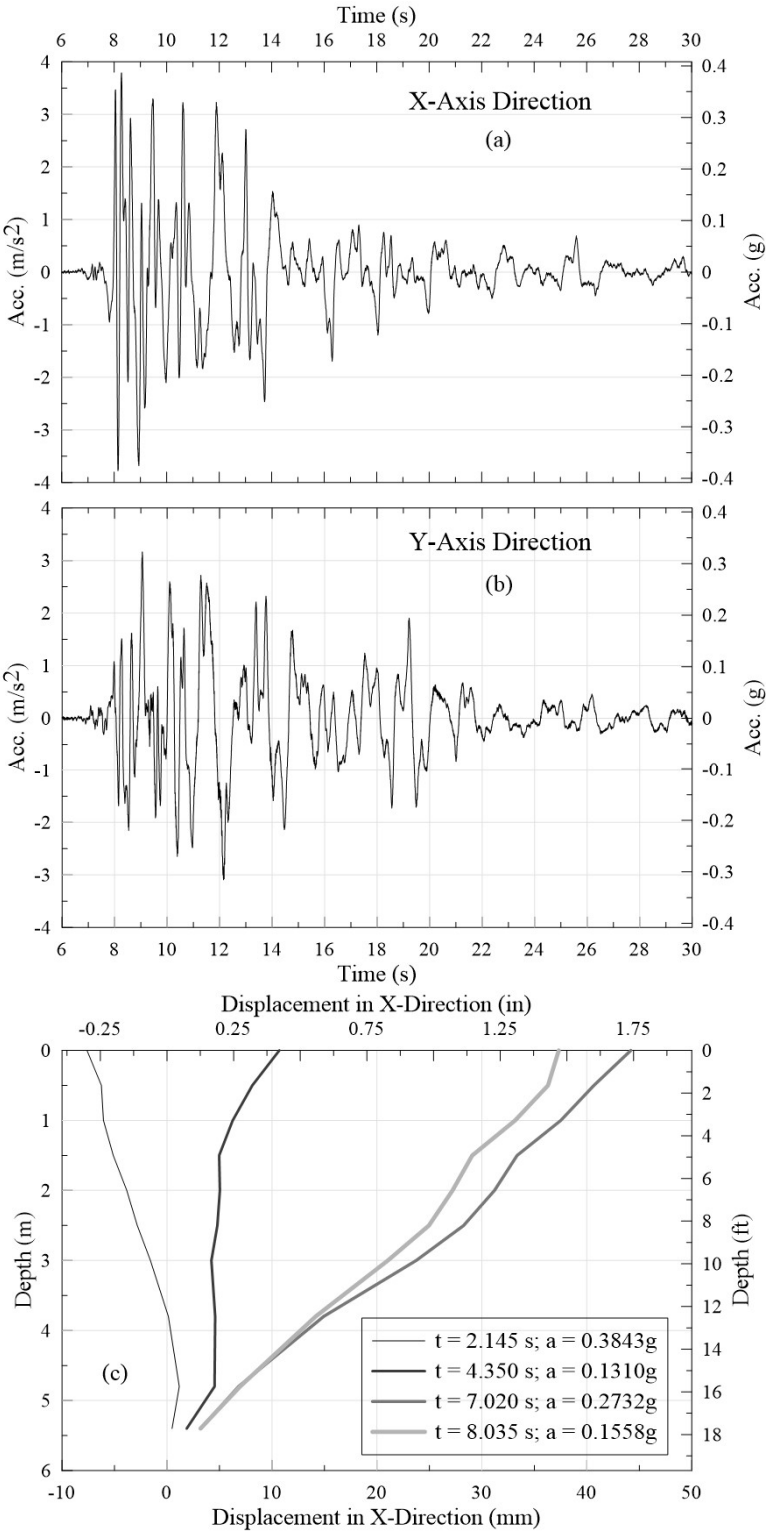

Figure 4.6. Acceleration input at the container bottom in (a) x and (b) y directions, and (c) lateral displacements of the soil container for the 50% Kobe motion

Figure 4.6c displays the horizontal drift of the entire soil container in x-direction at selected acceleration levels during the 50% Takatori EQ. Recorded displacements were derived using displacement transducers installed along the container wall. Maximum recorded horizontal displacements at the container top measured 7.4 cm in x direction and 7.9 cm in y-direction. During the 80% Kobe motion maximum container displacements were measured to be 22.6 cm in the x-direction and 23 cm in the y-direction.

Ground settlement: Figure 4.7 shows time histories of the estimated soil settlements during the 50% and 80% Takatori motions at different elevations in the container. The settlements were measured through wire-type displacement transducers depicted in Figure 2.6 which were embedded in the ground at depths of -1.0 m, -2.0 m, -3.0 m, and -4.0 m. These transducers were located near the rigid vertical shaft at coordinates of X = -1.50 m and Y = 2.50 m in the global coordinate system.

In the upper 1.0 m of soil, a settlement of 6.7 cm, and 13.6 cm was measured after the 50% and 80% Kobe motion, respectively. As shown in Figure 4.7, settlements accumulated immediately upon load applications. In the 50% motion, maximum / residual settlement estimates of 6.70 cm, 5.80 cm and 5.40 cm were observed at depths of -1.0, -2.0 and -3.0 m below ground surface respectively, observed settlements at lower depth of -4.0 m were measured to be only 3.5 cm. In the 80% motion, a sudden increase was observed in recorded settlements at all of the levels around t = 12.44 s which is believed to be due to a potential gap in the sand material. Ignoring this sudden spike, measured settlements follow the trend of the 50% motion by gradually accumulating their maximum and residual value.

These settlement observations support the hypothesis that lateral residual pressures are accumulated and locked into the system and that an increase in soil density during shaking may

translate into an increase in lateral pressures (i.e., an accumulation of pressures that exceed the amount of static pressure measured prior to shaking).

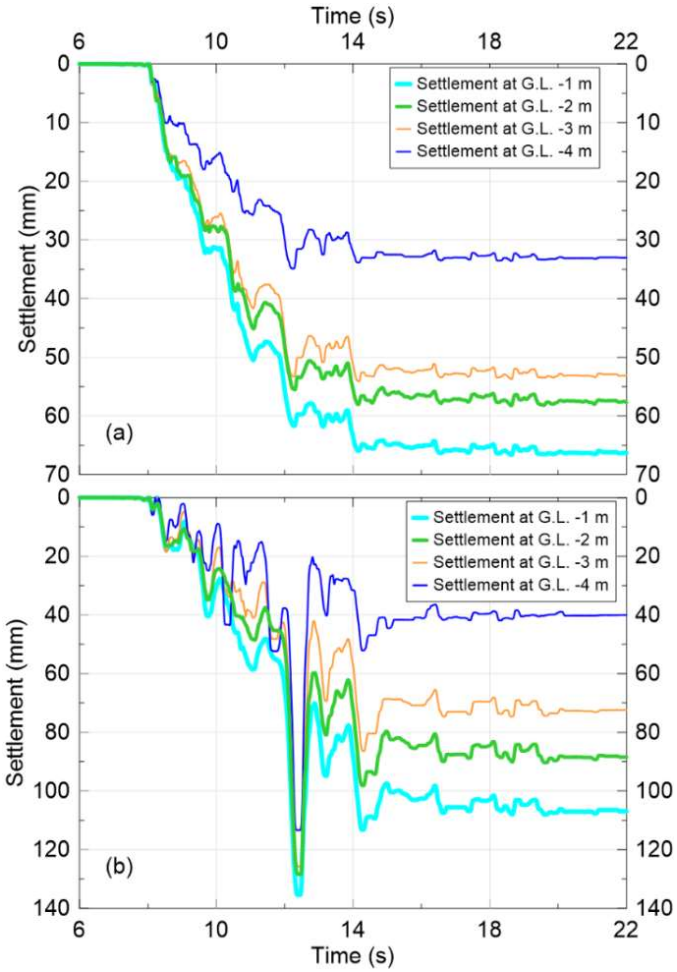

Figure 4.7. Vertical Settlement of fill soil at selected depths: (a) 50% Kobe motion, (b) 80% Kobe motion

4.5. Experimental soil pressure measurements

Figure 4.8 depicts the base acceleration and pressure time histories at selected depths along shaft VSR Side 3. The base acceleration (Figure 4.8a) was determined using the average of the four base sensors accelerations in x-direction, measured at the table surface. The dynamic pressure histories are shown in Figure 4.8b–e for selected depths.

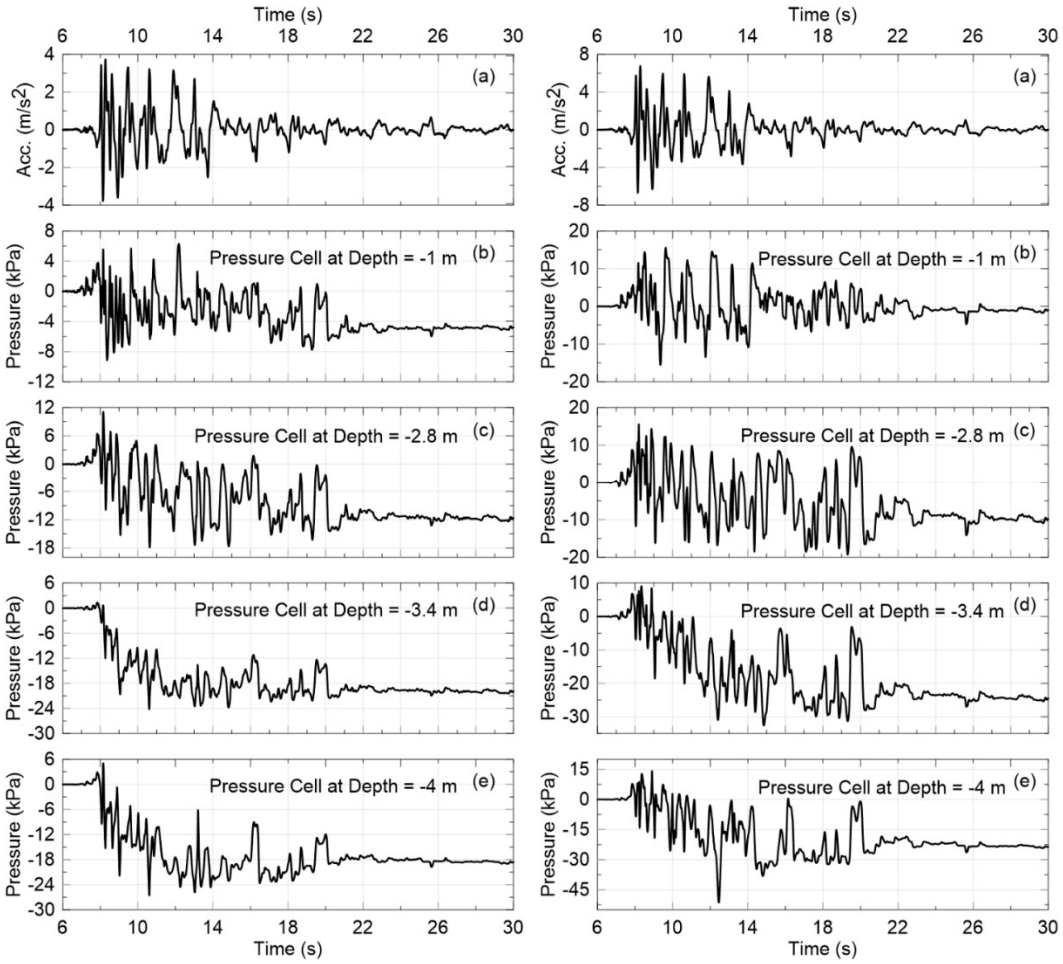

Figure 4.8. Acceleration and pressure time histories recorded during the 50% (left) and 80% (right) Kobe motions

It is customary for E-Defense experiments to zero all sensor readings prior to load application; hence, Figure 4.8 shows only seismic pressure increments during the dynamic loading (i.e., difference between the total dynamic and the static pressures). No static pressure readings are available. It should be noted that the increase of the pressure against the wall relative to the static case is shown with negative values and positive values indicate the decrease of the total dynamic stress with respect to the static pressure. Time histories depicted in Figure 4.8 indicate an accumulation of lateral soil pressures with increasing shaking time and overall increase of pressure

magnitudes with increasing depths. In addition, residual lateral pressures are accumulated towards the end of shaking which can be correlated to the densification of the fill soil in the container.

Figures 4.9 and 4.10 show a suite of pressure distribution profiles for selected times steps during the 50% and 80% Kobe earthquake motion in X and Y direction, i.e. normal to side 3 and 2, respectively. Time steps were selected to include acceleration peaks and intermediate acceleration levels as indicated in the acceleration time history. A general "belly-shaped" pressure distribution commonly known for flexible retaining structures was observed. The set of curves presented in Figures 4.9 and 4.10 suggests that maximum pressure magnitudes do not occur simultaneously with the level of maximum ground accelerations. Consequently max pressures and maximum inertial forces do not coincide. Similar conclusions were reached by Al-Atik and Sitar (2010) while studying the seismic pressure distribution on rigid open-channel structures. This observation supports the theory that pressures are dependent on soil-structure interaction in terms of relative displacements as proposed by Brandenberg et al. (2015).

Similar pressure distributions were obtained for the 80% Kobe motion. The total seismic pressure envelope was developed for both ground motions and is shown in Figure 4.9 and 4.10 by a dashed line. This line represents the maximum pressures at any sensor location during the applied ground motion. Both ground motions show consistent results. On average, total pressures during the 80% motion are 42% higher than for the 50% motion.

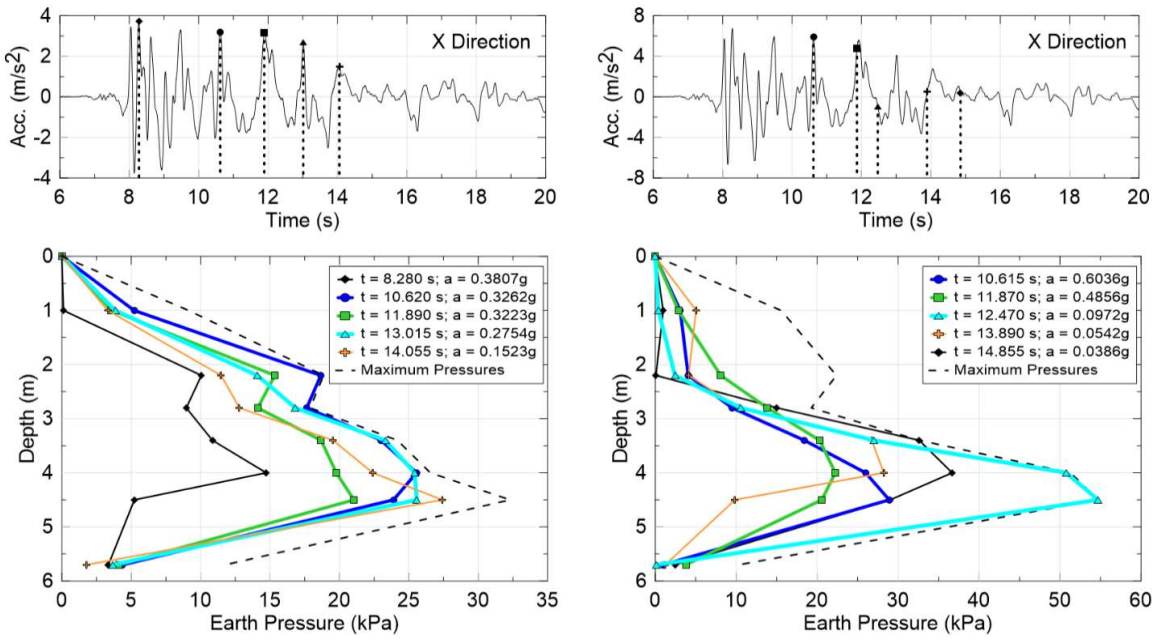

Figure 4.9. Acceleration records in X direction and soil pressures distribution for selected time steps and accelerations: 50% Kobe motion(left), 80% Kobe motion (right)

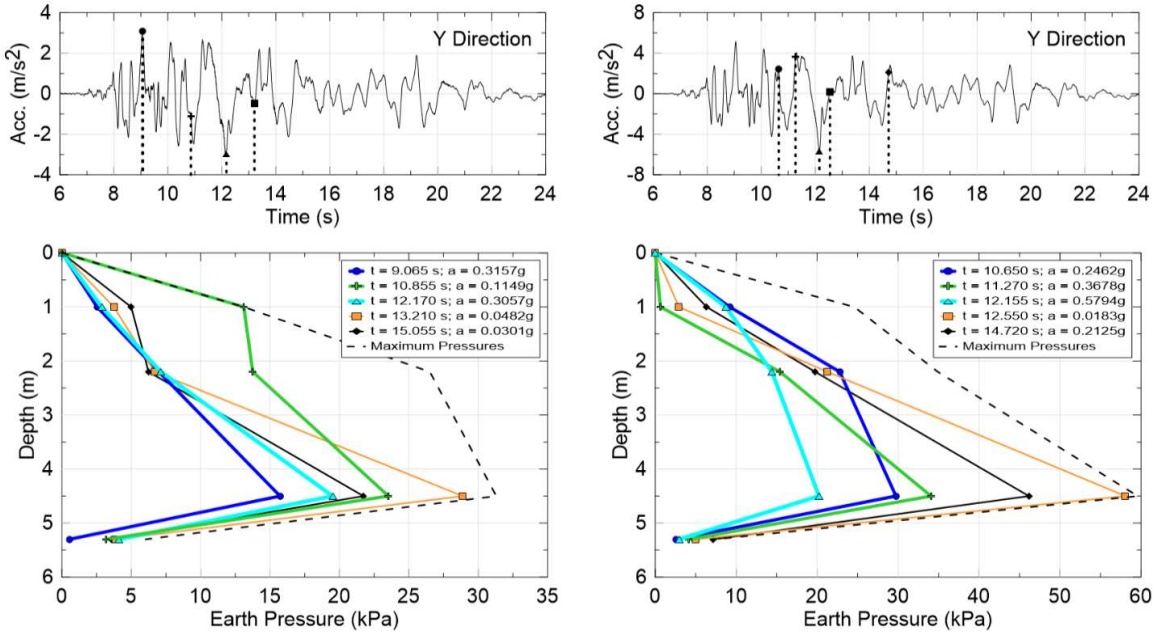

Figure 4.10. Acceleration records in Y direction (side 2) and soil pressures distribution for selected time steps and accelerations: 50% Kobe motion(left), 80% Kobe motion (right). Please note: less sensors were installed on side 2 compared to side 3.

4.6. Comparison of experimental results with analytical models

The experimental results were compared with three different elastic-based methods and six limit-state methods as introduced in the chapter 1 of this dissertation. In these comparisons, the experimental pressure profiles were generated using the maximum pressure recordings at each depth (i.e., dashed lines in Figures 4.9 and 4.10) and not at the time instant with the maximum resultant seismic force. This selection was due to the limitations of the analytical methods utilized in this study. For instance, the Brandenberg method (2015) predicts the pressure profile based on the maximum pressures of each depth obtained separately and not at the time of maximum resultant force. Moreover, all of the other studied analytical methods use the pseudo-static approach which ignores the time history of the seismic motion. Therefore, conservatively it was decided to use the profile resulting from maximum pressures of each depth.

4.6.1. Comparison of soil pressure measurements with elastic-based methods

Veletsos and Younan (1997), Ostadan (2004), and Brandenberg et al. (2015) were selected as representative elastic methods. Among the three, only Veletsos and Younan derived their solution for a flexible boundary condition. Methods suggested by Ostadan (2004) and Brandenberg et al. (2015) are more applicable to rigid retaining structures, but are included for completeness, until more solutions for flexible structures become available. All of the elastic-based methods consider the retained soil as a single uniform layer. Therefore the top and bottom strata in the experiment were simulated through a combined layer of equivalent properties, specifically a weighted average shear wave velocity and corresponding shear modulus of 207 m/s and 76 MPa, respectively (NIST, 2012).

Figures 4.11a and 4.11b depict the distribution of measured and analytically determined seismic soil pressures (dynamic increment only) along the vertical shaft side #3 for the 50% and 80% Kobe motions.

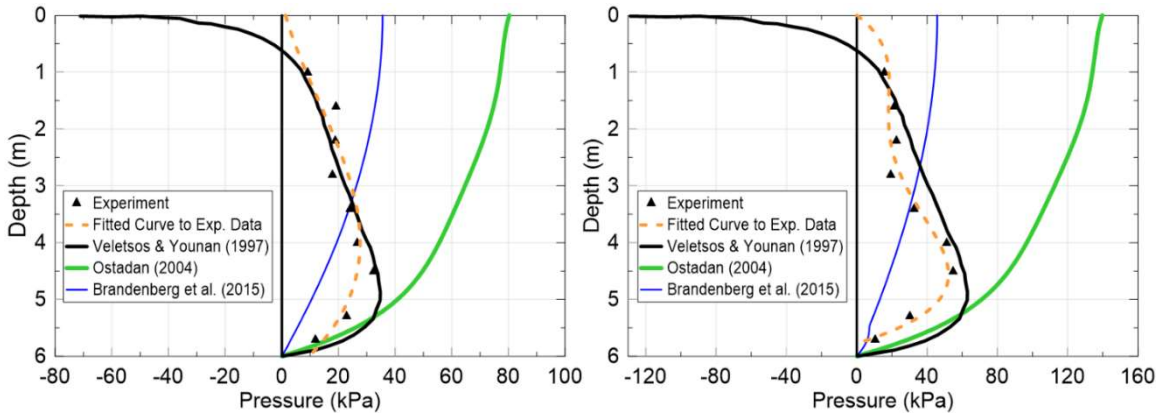

Figure 4.11. Comparison of the distribution of seismic lateral earth pressures obtained from elastic-based methods with the experimental results for the 50% motion (a) and 80% motion (b)

Veletsos and Younan (1997) provide a good fit to the experimental measurements and capture the soil pressure distribution along the majority of the vertical shaft. The amplification factor, required by the method was taken as 1.0. The small wall thickness of the vertical shaft resulted in a relative flexibility d_w that exceeded the proposed values of Veletsos and Younan; thus the upper limit of $d_w = 40$, as suggested by the authors was utilized. The vertical shafts were fixed on the shake table; hence the relative rotation stiffness d_θ was zero. A comparison between the pressures obtained from this method and the maximum recorded pressures at the depths of the soil pressure sensors was approximately 8% for the 50% motion and 15% for the 80% motion. The negative soil pressures predicted by Veletsos and Younan in the near-surface region are an inherent byproduct of the assumption that complete bonding between the wall and the soil medium exists. Due to soil gapping, settlement and caving, this was not observed in the experiment and near surface pressures are fitted to be zero.

The Ostadan (2004) method as well as the Brandenberg et al. (2015) method did not provide a close fit to the experimental pressure distribution. This behavior was anticipated, as both methodologies were derived for boundary conditions different from this experiment. Consistent with the derivation by Ostadan larger pressure magnitudes for non-displacing rigid walls compared to those obtained for flexible wall systems are predicted, supporting the theory that flexible structures move with the soil during ground shaking and therefore generate less pressures. Both methods suggest maximum pressures to occur at the top of the wall coinciding with the highest amplification of the motion at the ground surface. Maximum seismic pressures suggested by Ostadan are 149% and 155% bigger than the recorded pressures for the 50% and 80% Kobe earthquake motion, respectively. Input parameters for the Ostadan analysis were selected as follows: the fundamental frequency of the system was taken as $f_o = 5.36$ Hz (Figure 4.4), and the acceleration response spectra using a damping ratio of 30% were developed for the 50% and 80% Kobe motions. As shown in Figure 4.12, response accelerations of 6.18 m/s^2 and 10.80 m/s^2, were obtained for both ground motions respectively.

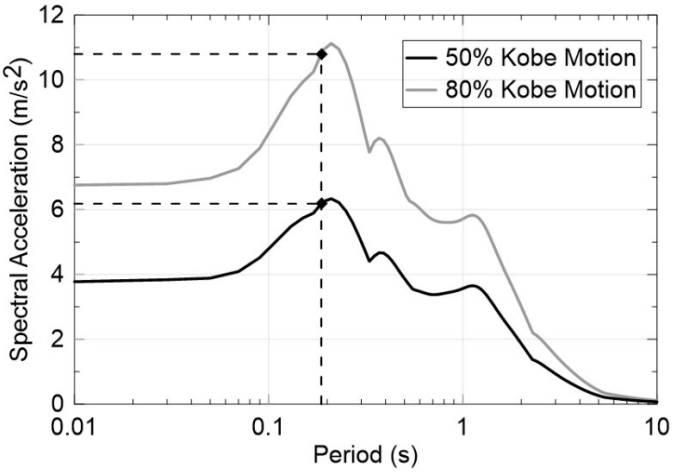

Figure 4.12. Response acceleration spectra of the system at ζ = 30% for 50% and 80% Kobe Motions

Similar to Ostadan (2004), the Brandenberg et al. (2015) solution was developed for rigid, non-displacing structures. The authors suggest back-calculating soil pressures using displacement time histories, as shown in chapter 1 Equations 6 and 7. This method (as discussed previously) appears to be more realistic regardless of the stiffness condition of the wall. Free field displacement time histories of the ground surface (i.e., u_{g0}) for both earthquake motions were obtained using the closest accelerometer of array #6 to the ground surface (depth of 0.1 m) and are shown in Figure 4.13a. The displacement and stiffness terms, $u_{g0} \cos kz$ and k_y^i, which are both frequency dependent were then computed at different frequencies, and Fourier amplitudes of seismic soil pressures in the frequency domain were obtained. Values of k_y^i were calculated based on the average shear modulus, shear wave velocity, and damping ratio presented above. It should be noted that in order to gain correct pressure profiles, seismic soil pressure amplitudes $p_E(z)$ were zeroed for frequencies bigger than the Nyquist frequency. Time histories of seismic soil pressures at different wall elevations were calculated through Inverse Fast Fourier Transform (IFFT). Exemplary seismic pressure time histories at depths of 0.0 m, 2.0 m, and 5.0 m for 50% motion are presented in Figure 4.13b. At each depth, the maximum value of p_E in the time history was selected as the maximum seismic pressure at that level, and seismic pressure distribution profiles for 50% and 80% motions were assembled.

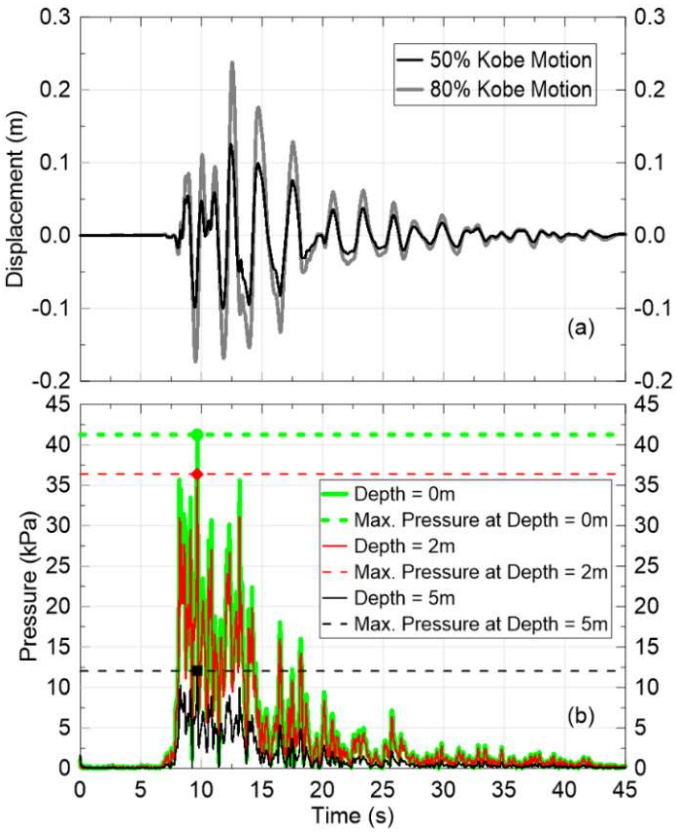

Figure 4.13. (a) Ground surface displacement (u_{g0}) time histories for 50% and 80% motions, (b) sample seismic pressure time histories for the 50% motion obtained using the Brandenberg et al. method, max values indicated with dashed line

Table 4.1 presents a summary of elastic based methods and experimental data in terms of pressure resultants (force and moment) and point of application of the resulting force. Lateral seismic soil pressures were assumed to be zero at the ground surface. The trapezoidal rule was employed to calculate the experimental resultant force of the maximum recorded pressure envelope. The point of application of the resultant force was obtained through computation of the first area moment under the pressure curve with respect to the base of the shaft.

Table 4.1. Summary of the results of elastic-based methods and their comparison with experimental data for 50% and 80% motions

	Ground Motion					
	Kobe EQ - 50% Motion			Kobe EQ - 80% Motion		
	Resultant Force (kN)	Point of Application (h/H)	Resultant Moment[a] (kN-m)	Resultant Force (kN)	Point of Application (h/H)	Resultant Moment[a] (kN-m)
Experiment	108.73	0.419	273.35	155.37	0.409	381.28
Veletsos and Younan (1997)	94.3	0.257	145.41	170.72	0.257	263.25
Ostadan (2004)	355.43	0.587	1251.82	618.38	0.587	2177.93
Brandenberg (2015)	140.81	0.627	529.73	179.93	0.628	677.98

[a] Resultant Moment was calculated as the product of the resultant force and height with respect to the base

Brandenberg et al. (2015) conservatively over-predict the resultant forces for both ground motions, but provide a reasonably close fit to the experimental data in terms of resultant pressure magnitude. Discrepancies of only 10% and 16%, for the 50% and 80% ground motions, respectively, were back-calculated. Ostadan (2004) significantly over-predicts the resulting force and moment, while Veletsos and Younan (1997) under-predict the pressure resultants for the 50% Kobe earthquake. This under-prediction can potentially be attributed to the assumption that perfect bonding between wall and soil is suggested in the Veletsos and Younan method, which allows for negative stress development rather than gapping. Ostadan (2004) and Veletsos and Younan (1997) ignore the influence of frequency of the applied motions, hence the point of application of the resultant seismic force is identical regardless of the ground motions applied. This assumption is reasonable for frequencies whose ratio to the fundamental frequency of the system is almost zero (i.e., pseudo-static condition). However, for ground motions with higher dominant frequencies, differences in the location of the resultant force will become apparent.

This comparison enforces that formulations shall not be extrapolated outside the range of their original development. The presented analytical methods have been developed for retaining structures with plane strain configuration. Although the studied model structure represents typical geometric shapes of subsurface structures, its configuration induces some three-dimensional effects which are not present for typical 2D retaining walls. In this type of underground structures, and in addition to the effects of bottom fixity, the structural flexibility plays an important role which might explain the good agreement between the obtained experimental results and the Veletsos and Younan (1997) method.

4.6.2. Comparison of soil pressure measurements with limit-state methods

Experimental results were compared with predictions from six limit-state methods. It should be noted that the method proposed by Xu et al. cannot be used in the comparative analysis as it performs unreliably for higher levels of base accelerations (e.g., $a > 0.4g$).

The first three methods, namely, Mononobe-Okabe, M-O, Seed and Whitman, S-W, and Mylonakis et al. (2007) neglect the cohesion of the soil material; while the remaining three methods (Richards and Shi (1994), Shukla and Bathurst (2012), and Iskander et. al (2013) consider the cohesion of the soil/rock material. For the approaches that neglect the cohesion of the soil material, the two-layered soil strata was modeled as a combined, single, uniform layer with an equivalent weighted unit weight of $\gamma = 17.33$ kN/m^3 and a friction angle of $\varphi = 36°$. For the methods considering cohesion, the formulations were adjusted to account for the two-layer soil system, as explained in more detail hereafter.

Iskander et al. (2013), and Richards and Shi (1994) capture the variation of lateral soil pressures along the height of the retaining structure by utilizing the stress state at every depth. This state of stress should comply with the Mohr-Coulomb failure criterion and use the mechanical

properties (i.e., c and φ) of that specific depth. The original formulations of both methods assume constant unit weight for the retained soil medium and are applicable to the top soil layer. When calculating the soil pressures in the bottom layer the top layer was simulated by a uniformly distributed vertical surcharge.

Shukla and Bathurst employ the kinematic solution and determine the resultant force by finding the equilibrium of forces on the assumed failure wedge behind the wall (Figure 4.14a). Thus, the authors are not able to capture the lateral stresses at each depth along the wall and assume a linear stress distribution. The effect of the different cohesion and unit weight of the cemented layer should be considered in the applied forces on the failure wedge. The Shukla method which was originally developed for a single uniform layer was modified accordingly and a new unit weight, γ_{New}, is defined based on the different thicknesses and unit weights of the first and the second layer: $\gamma_{\mathrm{New}} = \mathrm{b}^2 \cdot \gamma_2 + \mathrm{a} \cdot \gamma_1(1 + \mathrm{b})$, where a and b are defined in Figure 4.14b.

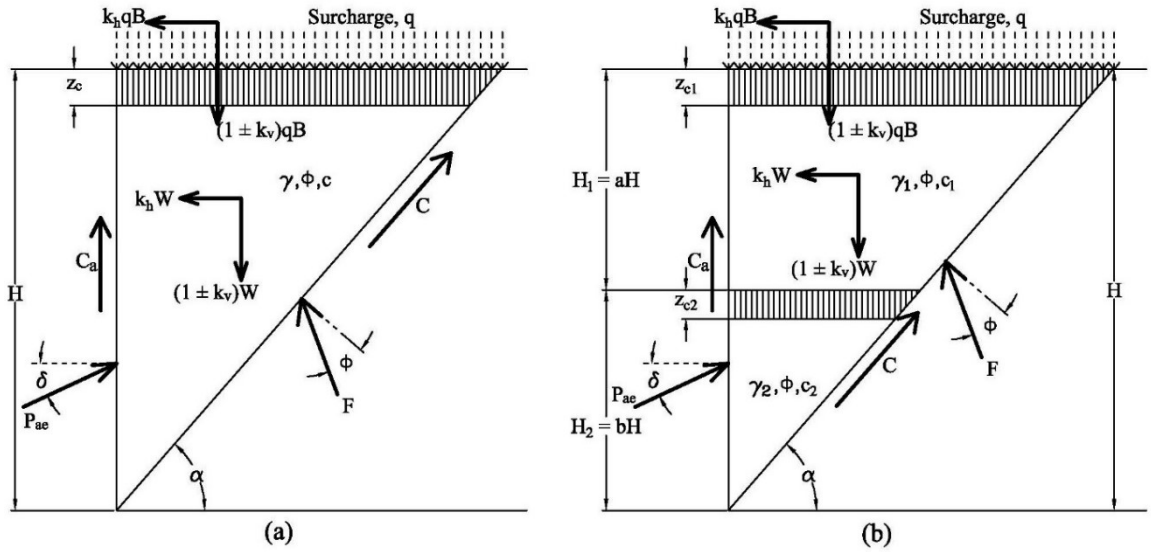

Figure 4.14. Forces acting on a trial failure wedge: (a) consisting of a single layered backfill (original Shukla and Bathurst method), (b) consisting of a two layered backfill (modified Shukla and Bathurst method)

Following Huntington, 1957, Shukla and Bathurst (2012) suggest the use of the Rankine tensile crack equation, i.e., $z_c = \frac{2c}{\gamma}\tan\left(\frac{\pi}{4}+\frac{\varphi}{2}\right)$ as a rough approximation for seismic loading and as recommended by Lambe and Whitman (1979), assumed that the full cohesive resistance is mobilized at z_c, and at points between the ground surface and the z_c, less than the full cohesive resistance is mobilized.

Hence, the total cohesion, C, and adhesion, C_a, forces for 2-layer system presented by Figure 4.14b are:

$$C = \left(\left(\frac{c_1}{2}\right)z_{c1} + c_1(H_1 - z_{c1}) + \left(\frac{c_2}{2}\right)z_{c2} + c_2(H_2 - z_{c2})\right)\text{cosec}\alpha \quad (2)$$

$$C_a = a_f \cdot C \cdot \sin\alpha \quad (3)$$

The computed tensile crack depth in the cemented layer exceeded the thickness of this layer, and thus the average mobilized cohesion in this layer was estimated to be $0.5 \times \left(\frac{1.10}{59.08}\right) \times 334.19\ \text{kPa} = 3.11\ \text{kP}$.

The distribution of seismic lateral earth pressures obtained from limit-state methods for the 50% and 80% Kobe motions are presented in Figures 4.15 and 4.16, respectively. The cohesion of the sand layer was taken as zero, as suggested by the secant method.

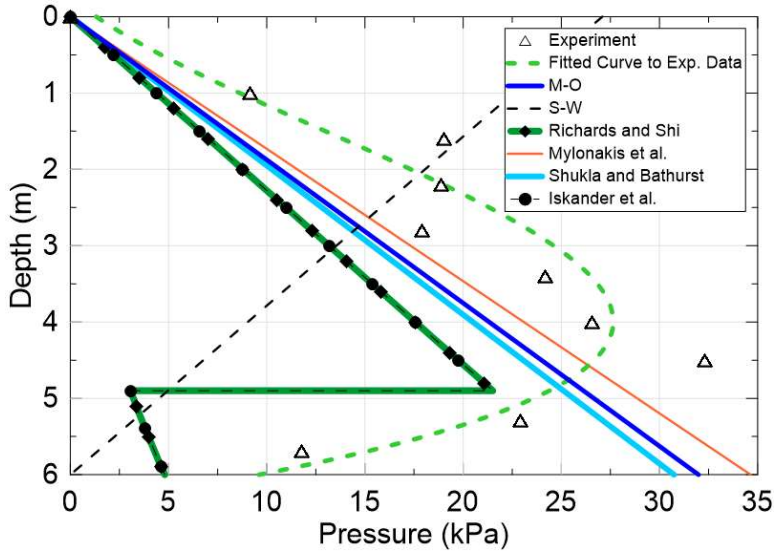

Figure 4.15. Comparison of the distribution of seismic lateral earth pressures obtained from limit-state methods with the experimental results for the 50% motion

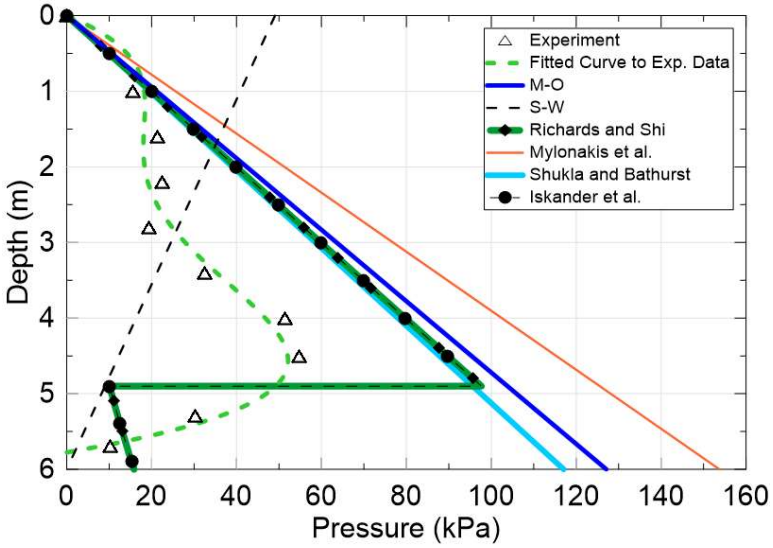

Figure 4.16. Comparison of the distribution of seismic lateral earth pressures obtained from limit-state methods with the experimental results for the 80% motion

Results for the 50% Kobe motion with a PBA of 0.38g (Figure 4.15) suggest that all limit-state methods under-predict the measured seismic pressures along the shaft. This finding is contrary to observations of yielding rigid walls for which limit-state methods were observed to lead to excessively conservative designs for PGAs below 0.4g (Seed and Whitman 1970, Clough and

Fragaszy 1977; Sitar et al. 2012). Within the upper sand layer, the calculated pressures by Mylonakis et al. (2007) were closest to the experimental data; however none of the methods is capable of capturing the pressure distribution accurately. Richard and Shi (1994), as well as Iskander et al. (2013) provide the same values of seismic stresses along the wall although they use two different sets of assumptions and formulations. Both are capable of implementing a two-layer stratigraphy but can't assimilate the experimental pressure distribution on the flexible system.

Results for the 80% Kobe motion (PBA 0.69g) show a strong over-prediction of seismic soil pressures for all methods. At the elevation of maximum seismic pressures, the difference in pressure magnitude between experimental and limit-state methods ranged between 60.48% and 110.75%. Comparison analyses not presented in this chpater considered the apparent cohesion in the abovementioned methods, and yielded a much closer match between the experimental data and the Rankine based methods (i.e., Richards and Shi 1994, Iskander et al. 2013) for the sand layer.

Table 4.2 summarizes the resultant forces, their point of application and corresponding moments for all limit-state methods. As observed in Figures 4.15 and 4.16, none of the methods can capture the experimental location of the resultant force. This mismatch can in part be attributed to the fact that all of the limit-state methods consider earthquake loading through pseudo-static inertial forces and ignore the frequency characteristics of the applied motion which has a significant influence on the distribution and magnitude of seismic soil pressures.

Table 4.2. Summary of the results of limit-state methods and their comparison with experimental data for 50% and 80% motions

	Ground Motion					
	Kobe EQ - 50% Motion			Kobe EQ - 80% Motion		
	Resultant Force (kN)	Point of Application (h/H)	Resultant Moment[a] (kN.m)	Resultant Force (kN)	Point of Application (h/H)	Resultant Moment[a] (kN.m)
Experiment	108.73	0.419	273.35	155.37	0.409	381.28
M-O	95.97	0.333	191.75	381.27	0.333	761.78
S-W (1970)	81.28	0.6	292.61	147.14	0.6	529.70
Richards and Shi (1994)	57.01	0.427	146.22	253.44	0.435	661.09
Mylonakis et al. (2007)	103.92	0.333	207.63	461.16	0.333	921.40
Shukla and Bathurst (2012)	92.23	0.333	184.28	351.15	0.333	701.60
Iskander (2013)	57.02	0.427	146.25	253.48	0.435	661.19

[a] Resultant Moment was calculated as the product of the resultant force and (h) with respect to the base

4.7. Summary

Seismic soil pressure measurements were recorded on flexible vertical underground structures with dimensions of 0.8 m in width and 7 m in height. Pressure records were measured through contact pressure sensors installed at various elevations on multiple shaft sides. The underground structures are constructed as hollow aluminum structures and subject to earthquake ground motions with PGAs of 0.38g and 0.69g. The surrounding soil strata consisted of cemented sand at the bottom of the structure, and a thick medium dense silica sand layer at the top. The maximum pressure envelope took a curved, belly-shaped form and was generally best captured through the analytical solution for flexible structures suggested by Veletsos and Younan (1994). Current limit-state methods available in literature were not able to reproduce the pressure profiles observed in the experiment. The comparison analysis affirmed the importance of considering the structural flexibility of the structure as well as the nature of the loading (i.e., frequency characteristics of the applied motion). Even though the structure in this experiment showed strong resemblance with a

vertical shaft-type of structure, general soil pressure estimations, primarily developed for retaining-type structures, could be used as preliminary estimate.

Chapter 5

3D numerical analyses of seismic soil pressures on deep underground structures

5.1. Introduction

This chapter presents the results of 3D numerical analyses of the seismic behavior of deep underground structures using the finite element code ABAQUS. First, the correctness of the utilized numerical methodology is verified through modeling a series of large-scale tests performed on an underground structure system (Lemnitzer et al. 2017). Keeping the configuration of the baseline model, a limited set of parametric studies is then performed, and effects of the structure's adjacent soil parameters (i.e., cohesion, and friction angle) and also the flexibility of the structure are investigated. In the last section, a simplified 3D soil-structure model is developed and influences of the most important parameters on the seismic soil pressures, including the retained soil mechanical parameters, structure and its base flexibilities, amplitude of the ground motion's acceleration, and geometry of the wall are examined through an extensive set of parametric studies. Variations of the resultant seismic forces and their corresponding moments against each of the studied parameters are presented by normalized graphs which could be used in preliminary analysis and design stage of deep embedded structures.

5.2. Numerical simulations

5.2.1. Model calibration

Prior to performing a parametric study, the numerical model underwent a calibration process to replicate the experimental observations and gain confidence in varying soil, structural, and geometric parameters. Although there have been many researchers who used the 3D numerical approach to study the dynamic response of geotechnical structures like piles and tunnels (e.g., Chen et al. 2012, Luo et al. 2016, Nguyen et al. 2017) but all of the previous numerical studies of the dynamic response of retaining structures were performed assuming plane strain conditions (e.g., Psarropoulos et al. 2005, Jung and Bobet 2008, Al-Atik and Sitar 2010, Geraili Mikola and Sitar 2013, Wagner and Sitar 2016). In order to provide more accurate results and also due to the complex configuration of the tests, 3D approach was used in this research.

The test setup of the performed experiments is complicated and consists of different components (i.e., structural elements, soil materials, and the laminar soil box). In this chapter, Utilized procedures in the simulation of these components are first explained and are followed by the comparison of numerical and experimental results.

5.3.1.1. Laminar soil box and model structures

The laminar soil box is one of the main factors that should be considered in the modeling. Different researchers have used various methods for modeling the laminar soil box. In 2004, Prasad et al. reviewed the problems in the simulation of the laminar shear boxes and referred to the inertia force, friction, membrane effect, and the boundary effect as the main issues. In 2D plane strain modeling approach, the laminar box is not modeled and only its effect is idealized by horizontal rollers with a mass representing the effect of the inertia force caused by the laminar box (Matsui et al., 2001) which is not accurate. In 3D modeling approach, one possible method which

was proposed by Chen et. al (2012) is to use thin shell elements with the same stiffness as the soil (to minimize the boundary effects) and actual weight of the wall (to consider the correct inertial forces); the high stiffness of the wall material comparing to the soil is taken into account by assuming that each ring has only rigid movement in the direction of applied motion. Because of the circular shape of the laminar box in E-Defense project, this method which is only applicable to rectangular boxes could not be used in our studies. Therefore, in order to model the laminar soil box precisely, 4-node quadrilateral general-purpose shell elements with the same stiffness as the actual steel rings were used in the numerical models. The thickness of the shell elements was adjusted to 0.0102 m to provide the same weight as the actual rings. The slippage and separation between the wall and the soil were ignored and the soil was assumed to be constrained within each ring. Although the laminar box rings were allowed to move freely along the horizontal directions (x and y), the vertical movement of them was constrained to account for the roller bearings between them (Figure 5.1). This approach takes into account the boundary effects, inertial forces and shear deformations of the rings properly.

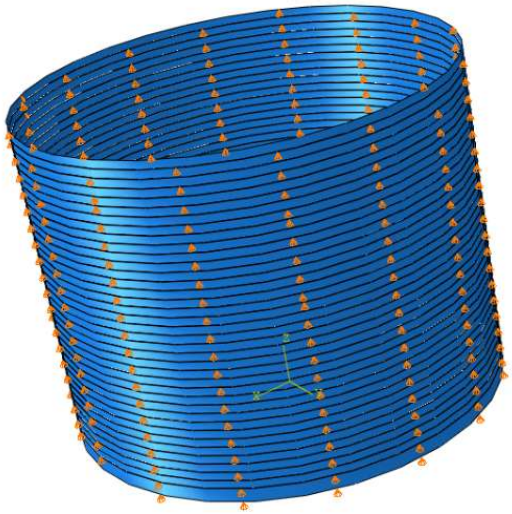

Figure 5.1. Laminar soil box geometry and boundary conditions

The model structures (i.e., vertical shafts, cut-and-cover tunnel, shield tunnels) were modeled using 4-node quadrilateral general-purpose shell elements (Figure 5.2). It should be noted that due to meshing limitations, the circular section of the shield tunnels was replaced by a square section with an equivalent area (side length of 0.36 m). All of the structural elements were modeled using linear elastic materials (Table 5.1). It should be noted that a damping ratio of 5% was used for all of the structural elements.

Table 5.1. Material properties of the structural elements

Material	Density (kg/m^3)	Modulus of Elasticity (GPa)	Poisson's Ratio (ν)
Aluminum (Vertical Shafts, Cut-and-cover Tunnel)	2700	70.6	0.33
Acrylic Plastic (Shield Tunnels)	1180	3.4	0.3
Steel (Laminar Soil Box)	7200	210	0.2

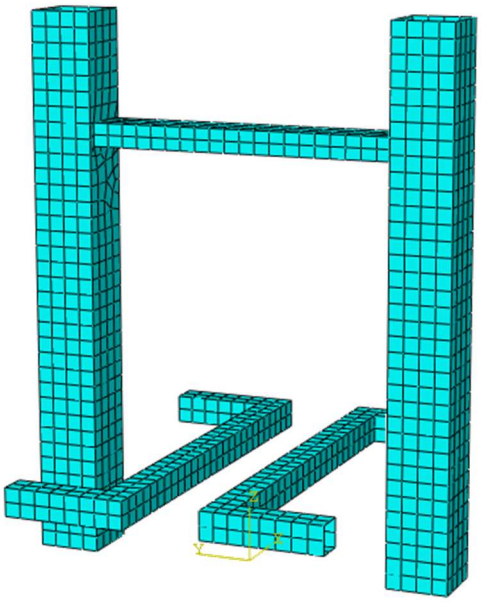

Figure 5.2. Meshing of the model structures

5.3.1.2. Soil materials models

The nonlinearity of soil materials plays an important role in the dynamic response of soil-structure systems. There are mainly two analytical approaches to model the nonlinearity of the soil material under seismic loadings: equivalent linear soil model and the fully nonlinear soil model. The equivalent linear soil model assumes soil properties to be constant during the ground shaking and estimate the shear modulus and damping ratio of the soil based its effective strain. This method can only approximate certain effects of soil nonlinearity. Using this approach makes soil elements to be too soft and overdamped under weak ground motions and too stiff and underdamped under strong ground shakings (Hokmabadi et al. 2014). Under earthquake motions soils show nonlinear behavior and geometric nonlinearity due to large strain deformations and thus modeling soils as a fully nonlinear material is a more appropriate method in dynamic response analysis of geotechnical structures with soil-structure interaction. In this research, the Modified Drucker-Prager/Cap model was used to model the sandy soil material (top layer) and the cemented layer was simulated using the Mohr-Coulomb constitutive model. Mohr-Coulomb required parameters for modeling the cemented layer were estimated based on what was explained before, however, the Modified Drucker-Prager/Cap model includes several mechanical parameters which should be determined precisely.

The Modified Drucker-Prager/Cap model has been widely used in finite element programs for a variety of geotechnical engineering applications and is based on the addition of a cap yield surface to the Drucker-Prager plasticity model. This model is capable of considering the effect of stress history, stress path, dilatancy, and the effect of the intermediate principal stress. The yield surface of this model consists of three parts: a Drucker-Prager shear failure surface, an elliptical cap, which intersects the mean effective axis at a right angle, and a smooth transition section between the shear failure surface and the cap, as shown in Figure 5.3. The addition of the cap yield

surface to the Drucker-Prager model serves two main purposes: it bounds the yield surface in hydrostatic compression, thus providing an inelastic hardening mechanism to represent plastic compaction; and it helps to control volume dilatancy when the material yields in shear by providing softening as a function of the inelastic volume increase created as the material yields on the Drucker-Prager shear failure surface. Elastic behavior can be modeled as linear elastic through using the generalized Hooke's law or alternatively by the Porous Elasticity model which is a nonlinear, isotropic model and considers the increase of the soil's stiffness when it undergoes compression. In this model, the bulk modulus, K, is not constant and depends on the mean effective stress, p′, void ratio, e_0, and unloading-reloading line slope, κ, (Eq. 1). κ is the slope of the unloading-reloading line in the $e - \ln p'$ plane and is related to the swelling index (C_s) through: $\kappa = \frac{C_s}{2.3}$. Young's modulus, E, and shear modulus, G, can be easily obtained from the bulk modulus. The porous elasticity model was used in this research.

$$K = \frac{(1+ e_0)p'}{\kappa} \quad (1)$$

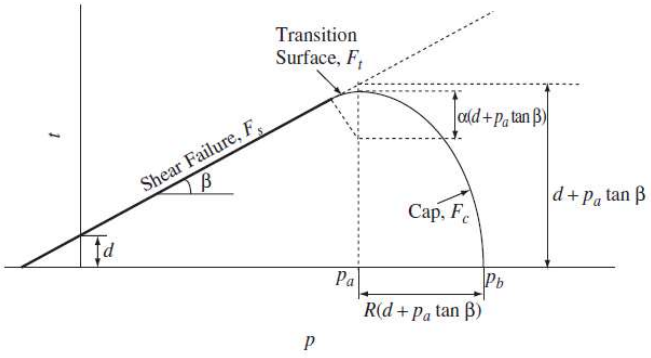

Figure 5.3. Yield surfaces of the modified Drucker-Prager/Cap model in the t-p plane (Helwany, 2007)

The Drucker-Prager shear failure segment is a perfectly plastic yield surface (no hardening) and is given by:

$$F_s = t - p\tan\beta - d = 0 \quad (2)$$

In Eq. 2, β is the soil's friction angle and d is its cohesion in the p-t plane. t is a measure of shear stress calculated as $t = q/g$, where g is a function used to control the shape of the yield surface in the deviatoric principal stress plane (the plane in the principal stress space orthogonal to the hydrostatic pressure axis) and is defined as

$$g = \frac{2K}{1+K+(1-K)(\frac{r}{q})^3} \quad (3)$$

Where r is the third stress invariant and K is a constant. Setting $K = 1$ causes the yield surface to be independent of the third stress invariant and t becomes equal to $q = \sigma_1 - \sigma_3$. For triaxial stress conditions, the Mohr-Coulomb parameters can be converted to Drucker-Prager parameters as follows:

$$\tan\beta = \frac{6\sin\varphi}{3-\sin\varphi'} \quad (4)$$

$$d = \frac{6c\cos\varphi'}{3-\sin\varphi'} \quad (5)$$

As shown in the figure, the cap yield surface is an ellipse with $\text{eccentricity} = R$ in the $p - t$ plane. The cap yield surface is dependent on the third stress invariant, r, in the deviatoric plane. The cap surface hardens (expands) or softens (shrinks) as a function of the volumetric plastic strain.

When the stress state causes yielding on the cap, volumetric plastic strain (compaction) results, causing the cap to expand (hardening). But when the stress state causes yielding on the Drucker-Prager shear failure surface, volumetric plastic dilation results, causing the cap to shrink (softening). The cap yield surface is given as

$$F_c = \sqrt{(p - p_a)^2 + \left(\frac{Rt}{1+\alpha-\frac{\alpha}{\cos\beta}}\right)^2} - R(d + p_a \tan\beta) = 0 \quad (6)$$

where R is a material parameter that controls the shape of the cap and α is a small number (typically, 0.01 to 0.05) used to define a smooth transition surface between the Drucker-Prager shear failure surface and the cap:

$$F_t = \sqrt{(p - p_a)^2 + \left[t - \left(1 - \frac{\alpha}{\cos\beta}\right)(d + p_a \tan\beta)\right]^2} - \alpha(d + p_a \tan\beta) = 0 \quad (7)$$

p_a is an evolution parameter that controls the hardening-softening behavior as a function of the volumetric plastic strain. The hardening-softening behavior is simply described by a linear function relating the mean effective (yield) stress, p_b, and the volumetric plastic strain, ε_{vol}^{pl}. This function can easily be obtained from the results of one isotropic consolidation test with several unloading-reloading cycles. Consequently, the evolution parameter, p_a, can be calculated as

$$p_a = \frac{p_b - Rd}{1 + R\,ta} \quad (8)$$

In this model, the plastic potential function in the p-t plane comprises two segments (Figure 5.4). In the cap region, the plastic flow is defined by a flow potential that is identical to the yield surface (i.e., associated flow). For the Drucker‐Prager failure surface and the transition yield surface, a non-associated flow is assumed: The shape of the flow potential in the $p - t$ plane is different from the yield surface. In the cap region the, elliptical flow potential surface is given as

$$G_c = \sqrt{(p - p_a)^2 + \left(\frac{Rt}{1 + \alpha - \frac{\alpha}{\cos\beta}}\right)^2} \tag{9}$$

The elliptical flow potential surface portion in the Drucker‐Prager failure and transition regions is given as:

$$G_s = \sqrt{[(p_a - p)\tan\beta]^2 + \left(\frac{t}{1 + \alpha - {}^{\alpha}/_{\cos\beta}}\right)^2} \tag{10}$$

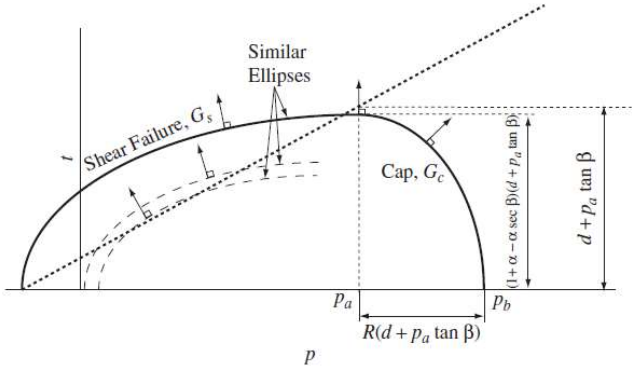

Figure 5.4. Plastic potential function of the modified Drucker-Prager/Cap model in the t-p plane (Helwany, 2007)

Consolidated undrained (CU) test results performed on the sandy soil were used in initial estimation of the Drucker-Prager/Cap model parameters (i.e., d, β, R, K, α, κ, and λ) to be used in

the numerical analyses. Since the average relative density of the sand layer in the E-Defense project was $D_r = 54.05\ \%$, Results of the (CU) triaxial tests performed at $D_r = 60\ \%$ and confining pressures of 50 kPa and 100 kPa were used to determine the parameters of this model. These tests were modeled through a two-dimensional axisymmetric approach Figure 5.5. Dimensions of the model were selected as the performed tests (diameter = 5 cm and height = 10 cm). The element chosen was a pore fluid/stress eight-node axisymmetric quadrilateral element with biquadratic displacement, bilinear pore pressure, and reduced integration. In order to simulate the undrained condition of the tests, during the loading step, all of the element sides were made impervious and a uniform downward displacement of 1.5 cm was applied slowly. The aforementioned mechanical parameters were chosen in a way to produce the same stress-strain and excess pore pressure-strain behavior as the sand specimens. These results are presented in Figure 5.6 for the both of the triaxial tests with confining pressures of 50 kPa (left) and 100 kPa (right), respectively.

Soil layers are modeled using the 8-node linear brick, reduced integration solid elements. Final mechanical properties utilized for both of the sand layer and cemented layer are presented in Table 5.2.

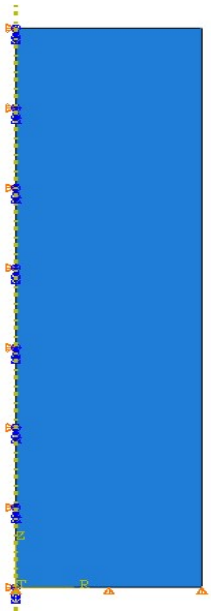

Figure 5.5. Axisymmetric model of the triaxial test

Table 5.2. Soil materials mechanical properties used in numerical analyses

Material Properties	Top Layer (Sand)	Bedrock (Cemented Layer)
Unit Weight (kN/m^3)	16.59	20.59
β°	51.8	-
d (kPa)	4	-
φ'°	-	36
ψ°	0	6
c' (kPa)	-	334
λ	0.004	-
κ	0.006	-
α	0.05	-
R	0.1	-
K	1	-
Initial Void Ratio (e_0)	0.636	-
G (MPa)	-	311
Poisson's Ratio (ν)	0.33	0.33

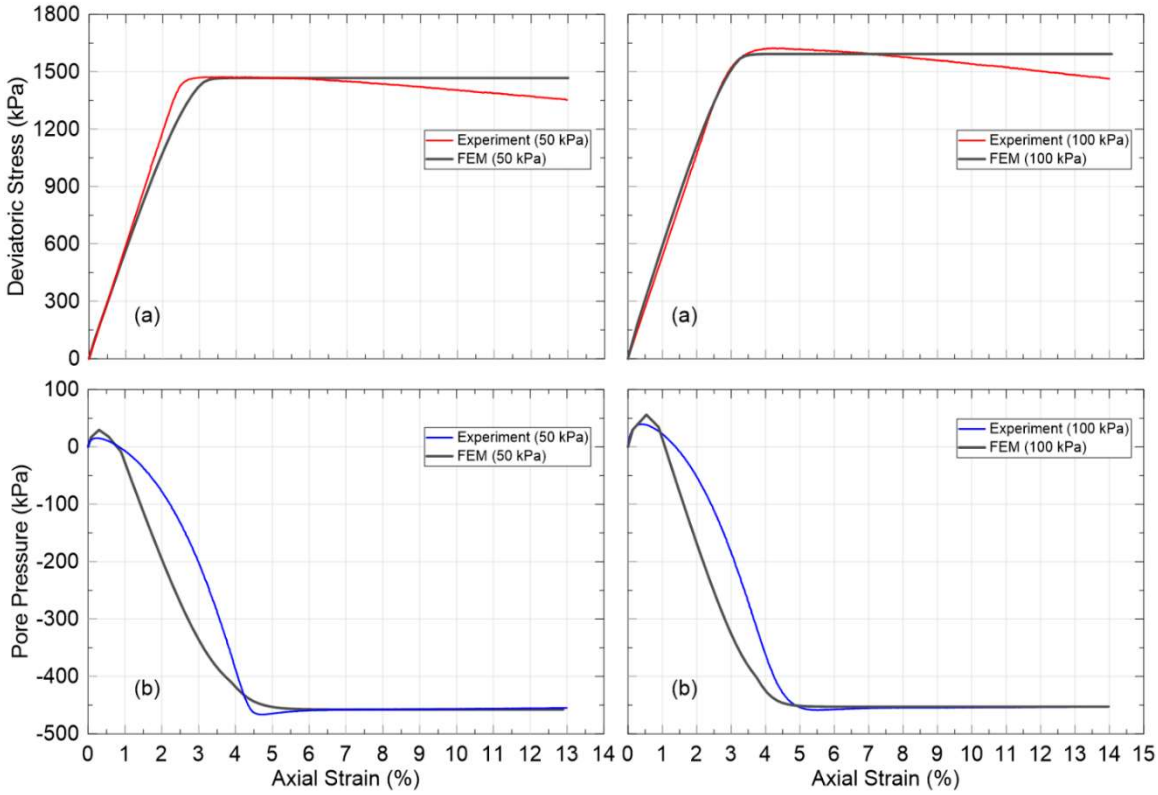

Figure 5.6. Comparison of numerical and experimental results of the triaxial tests

5.3.1.3. Soil damping

Rayleigh damping model was adopted for the soil materials. Damping coefficients α, and β for each of the Kobe motions were calculated through the Eq. 11 and by using the natural frequencies of the soil layers and damping ratios obtained from each test.

$$\alpha + \beta\omega_i^2 = 2\omega_i\zeta_i \tag{11}$$

ω_i is the i^{th} natural frequency of the system and ζ_i is its corresponding damping ratio. The first two Natural frequencies of the soil layers were computed from the sine sweep motions in x-direction with accelerations of 0.1 m/s^2 and 0.3 m/s^2. This direction was of interest as shaft side

#3 (normal to the x-direction) was used for numerical pressure analyses. For this purpose, the ratio of the Fourier amplitude of the acceleration at the ground surface to the amplitude of the corresponding base acceleration was calculated for each level of frequency. Calculation of acceleration Fourier amplitude at the ground surface was conducted twice, once using the recordings of the highest accelerometer along array 6 (close to the container's wall) and once using the average of recordings by highest accelerometers installed on different locations of the laminar soil box. The transfer function for the 0.1 m/s^2 sine sweep motion is shown in Figure 5.7.

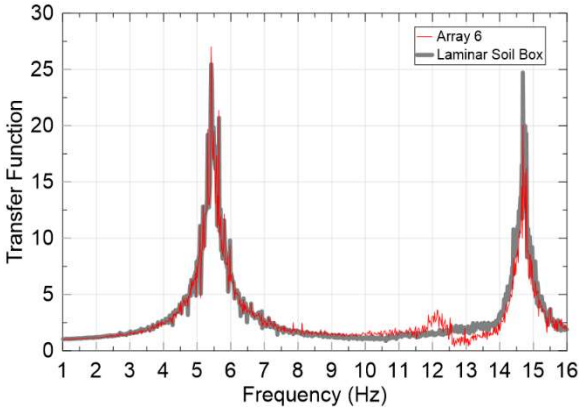

Figure 5.7. Transfer function from the step sine motion with 0.1 m/s2 amplitude

The fundamental frequency (ω_1) and 2nd natural frequency (ω_2) of the system were obtained equal to 5.36 Hz and 14.69 Hz, respectively.

Following the study by Zeghal and Elgamal (1994) and using the recordings of accelerometers along array 6, the equivalent uniform shear strains of the soil layers for the 50% and 80% motions were computed to be 0.182% and 0.387%, respectively (Keykhosropour and Lemnitzer, 2019). Damping ratios of the first two modes of vibration were assumed to be equal (Chen et al. 2012, Nguyen et al. 2017) and were found through the graphical solution by Seed et al. (1986) to be 12% and 16% for the 50% and 80% Kobe motions, respectively. Initially, α and β coefficients were

calculated using these damping ratios but investigation of acceleration time histories along the depth of soil materials obtained from numerical analyses, revealed that Rayleigh coefficients corresponding to damping ratios of 18% for the 50% Kobe motion and 21% for the 80% motion led to more accurate numerical results. Final Rayleigh coefficients used in numerical models were $\alpha = 8.88$ and $\beta = 0.0028$ for the 50% motion and $\alpha = 10.36$ and $\beta = 0.0033$ for the 80% motion.

5.3.1.4. Soil-structure interaction

Contact simulation is an important issue which can cause severe nonlinearities. In ABAQUS, there are mainly three different approaches for defining contact interactions: general contact and contact pairs which use surfaces to define contact and contact elements. It is generally recommended to use contact pairs or general contact if possible. In this research, contact pairs approach was selected for modeling the soil-structure interaction. Simulation of any contact requires the proper definition of its mechanical properties (i.e., pressure-overclosure relationship, frictional behavior) and formulation (i.e., contact discretization, tracking approach, and assignment of master and slave roles to the contact surfaces). If the surfaces of a contact pair are on parts with comparable stiffnesses, master surface should be chosen as the surface of the stiffer body or as the surface with the coarser mesh. In our numerical models, in contact with structural elements and the laminar soil box, soil materials were selected as slave surfaces. Hard contact relationship without separation was adopted for the pressure-overclosure relationship. The hard contact relationship minimizes the penetration of the slave surface into the master surface at the constraint locations and does not allow the transfer of tensile stress across the interface. The frictional behavior of contact surfaces was defined through the Coulomb failure model. This model relates the maximum shear stress (τ) across an interface to the contact pressure (p) through the coefficient

of friction (μ) as $\tau = \mu p$. In this study, μ was taken equal to 0.75 which is a commonly used value in geotechnical applications (Kim et al. 2011, Fatahi et al. 2014, Nguyen et al. 2017).

In ABAQUS, the contact simulation is conducted through applying conditional constraints at specific locations along interacting surfaces. The locations and conditions of these constraints depend on the discretization method used in the contact formulation. There are two available discretization approaches in ABAQUS: node-to-surface and surface-to-surface. The latter is a more realistic method and considers the shape of both the slave and master surfaces in the region of contact constraints and contrary to the former method, large penetrations of master nodes into the slave surface do not occur.

Tracking approach is another important component of contact formulation which accounts for the relative motion between the interacting surfaces of a contact pair. Finite-sliding and small-sliding are two available tracking approaches in ABAQUS. Finite-sliding is more general and allows for any relative motion between the contacting surfaces (e.g., separation, sliding, rotation). On the other hand, small-sliding approach assumes that there will be relatively little sliding of one surface along the other and is based on linearized approximations of the master surface per constraint. In this research, formulation of the soil-structure interactions was conducted through the finite-sliding, surface-to-surface method.

5.3.1.5. Geostatic stress equilibrium

The elasto-plastic behavior of the soil layers and the interaction forces between the soil material and model structures are significantly influenced by the initial stresses produced by the gravity. These initial stresses should be in balance with the applied gravity force and the boundary conditions (i.e., produce zero settlement) of the numerical model. In order to balance the initial stresses in soil, the gravity force is applied on the whole model and then the calculated stresses are

taken as initial conditions and applied on the whole system again. This procedure is performed before applying the dynamic loading and should result in almost zero settlement of the soil material otherwise the balance of the initial stresses is not achieved. Figure 5.8 shows the settlement contour of the model under study after applying the initial stresses and is can be seen the maximum settlement is 1.97×10^{-4} m which is almost zero.

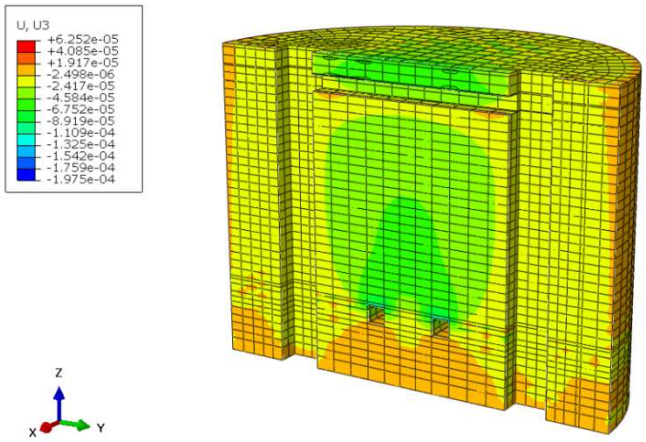

Figure 5.8. Settlement contour of the model after applying the initial stresses due to the gravity

In the experiment, the laminar shear box was constrained on the shaking table. Therefore, measured time histories of acceleration of the shake table, are applied directly to the base of the FEM model.

5.3.1.6. Seismic motion input

In E-Defense experiments, the laminar soil box was fixed on the shake table. Therefore, acceleration time histories of the seismic motions (i.e., 50% and 80% scaled Kobe motions) were applied directly to the base of the numerical model. Acceleration time histories of the applied motions are presented in Figure 5.9.

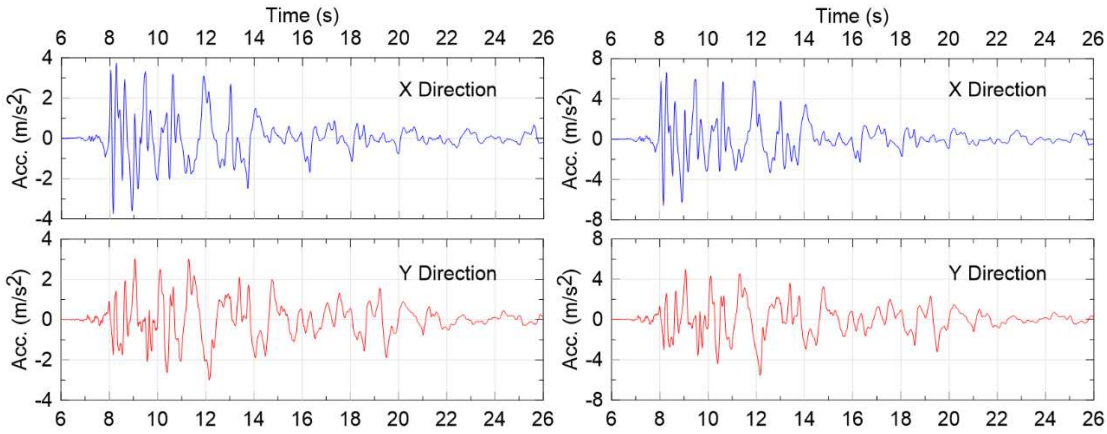

Figure 5.9. Acceleration time histories of the 50% (left) and 80% (right) Kobe motions

5.3.1.7. Results

In this section, results of numerical analyses are presented and compared with their experimental data concerning induced seismic soil pressures and acceleration response of the soil material at different depths. Soil accelerations recorded at different depths along the array #6 in both X and Y directions were compared with their numerical counterparts. These results are presented in Figures 5.10 and 5.11 for 50% and 80% Kobe motions, respectively. Acceleration time histories were also converted to frequency domain and compared to each other. Figures 5.12 and 5.13, depict the Comparison of experimental and numerical acceleration Fourier amplitudes at the depth of 3 m, for 50% and 80% motions, respectively. As it can be seen from these figures, numerical results are in acceptable agreement with experimental recordings in both time and frequency domains. For both motions, dominant frequencies were around 1 Hz and 3 Hz for the X component and around 1 Hz and 2 Hz for the Y direction.

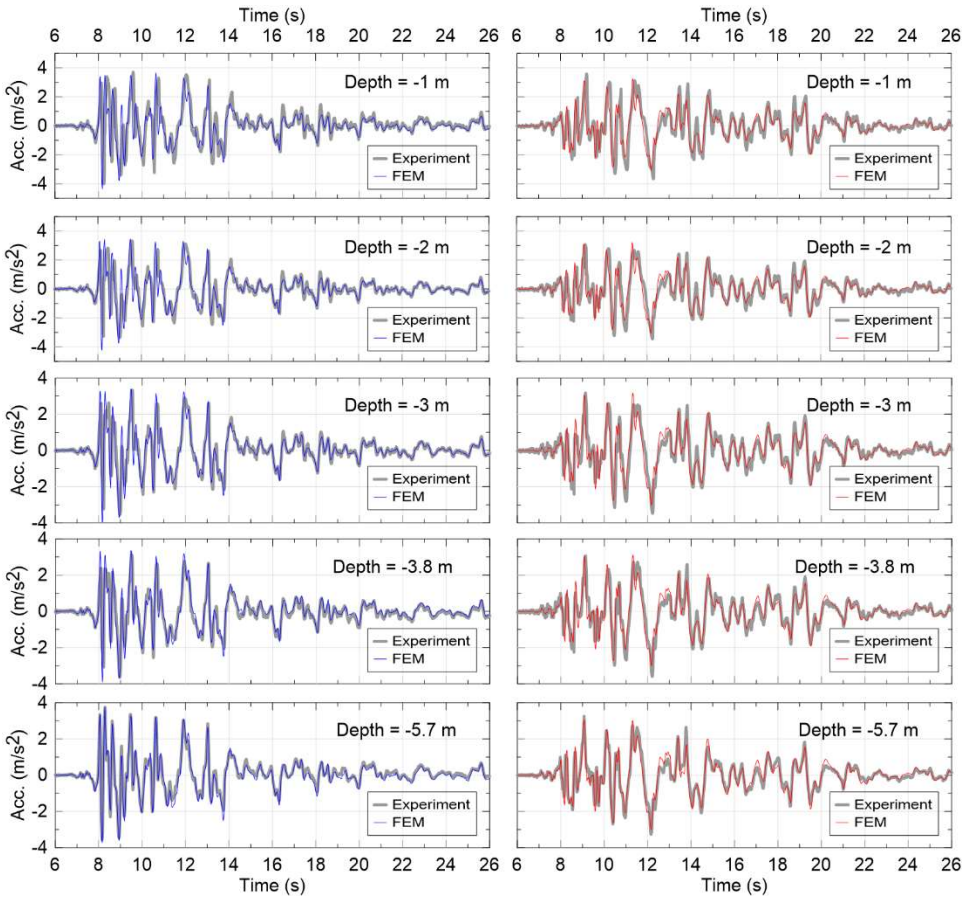

Figure 5.10. Comparison of experimental and numerical soil acceleration response at different depths along X (left) and Y (right) directions for the 50% Kobe motion

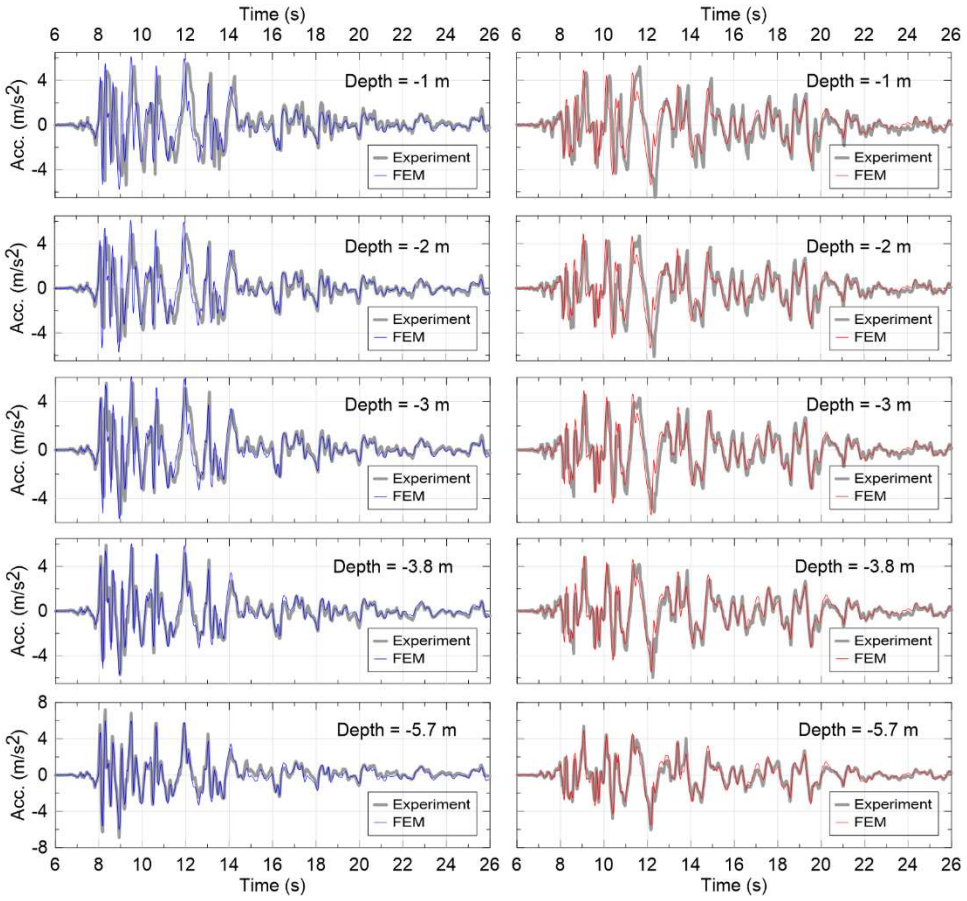

Figure 5.11. Comparison of experimental and numerical soil acceleration response at different depths along X (left) and Y (right) directions for the 80% Kobe motion

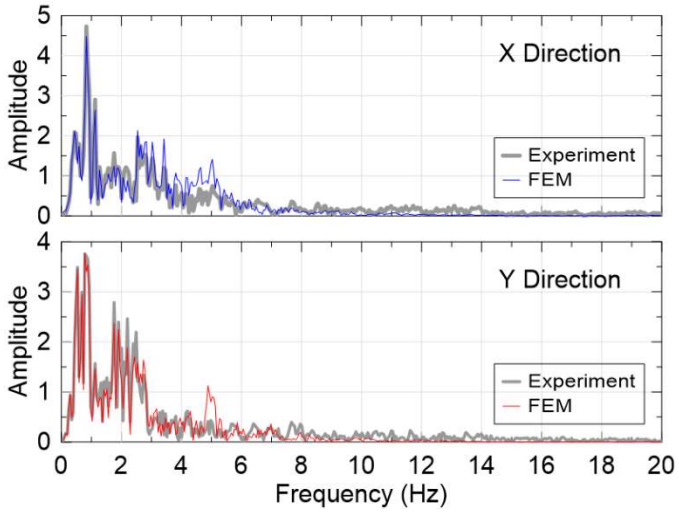

Figure 5.12. Comparison of experimental and numerical soil acceleration Fourier amplitude along X and Y directions at depth = 3m for the 50% Kobe motion

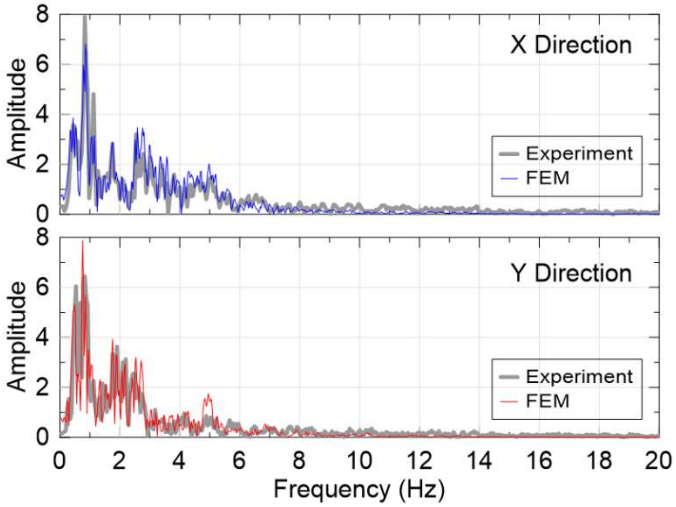

Figure 5.13. Comparison of experimental and numerical soil acceleration Fourier amplitude along X and Y directions at depth = 3m for the 80% Kobe motion

Since Side #3 of the vertical shaft had the most pressure cells installed, data from this side was used for analysis of seismic soil pressures. Distribution of maximum recorded pressures at different depths and also the experimental seismic pressure profile at the peak force instant were compared to their numerical counterparts. Figures 5.14 and 5.15 depict these results for 50% and 80% Kobe motions, respectively. Figure 5.16, depicts the contours of horizontal movement of the shafts at the peak force instant.

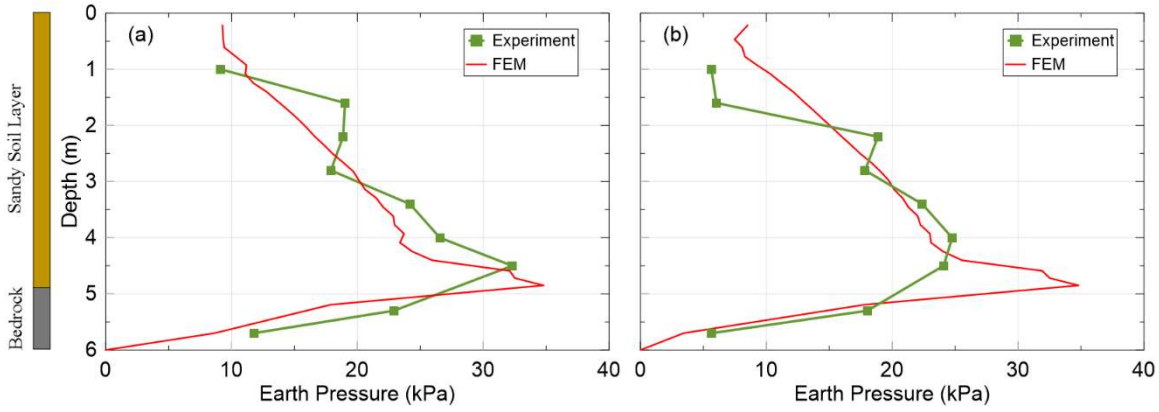

Figure 5.14. Comparison of the distribution of experimental and numerical seismic soil pressure for the 50% motion: (a) maximum pressures obtained at different depths, (b) pressure distribution at the peak force instant

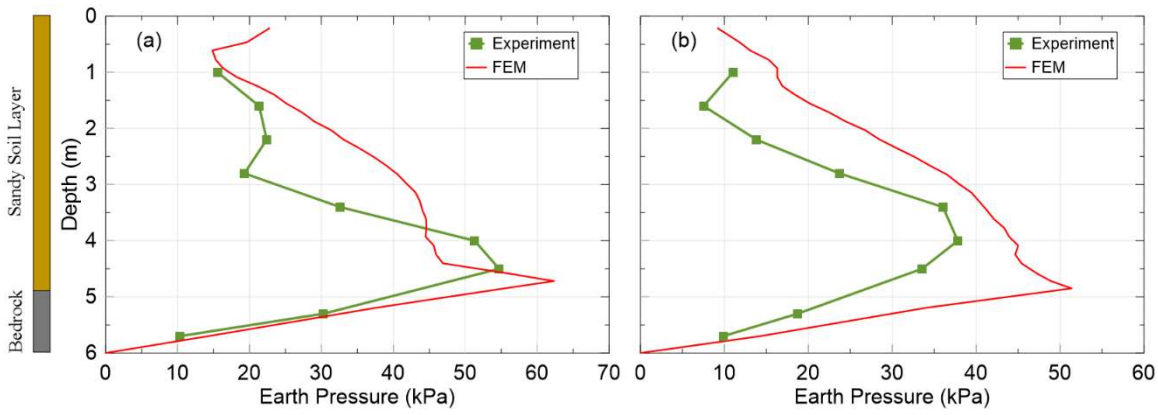

Figure 5.15. Comparison of the distribution of experimental and numerical seismic soil pressure for the 80% motion: (a) maximum pressures obtained at different depths, (b) pressure distribution at the peak force instant

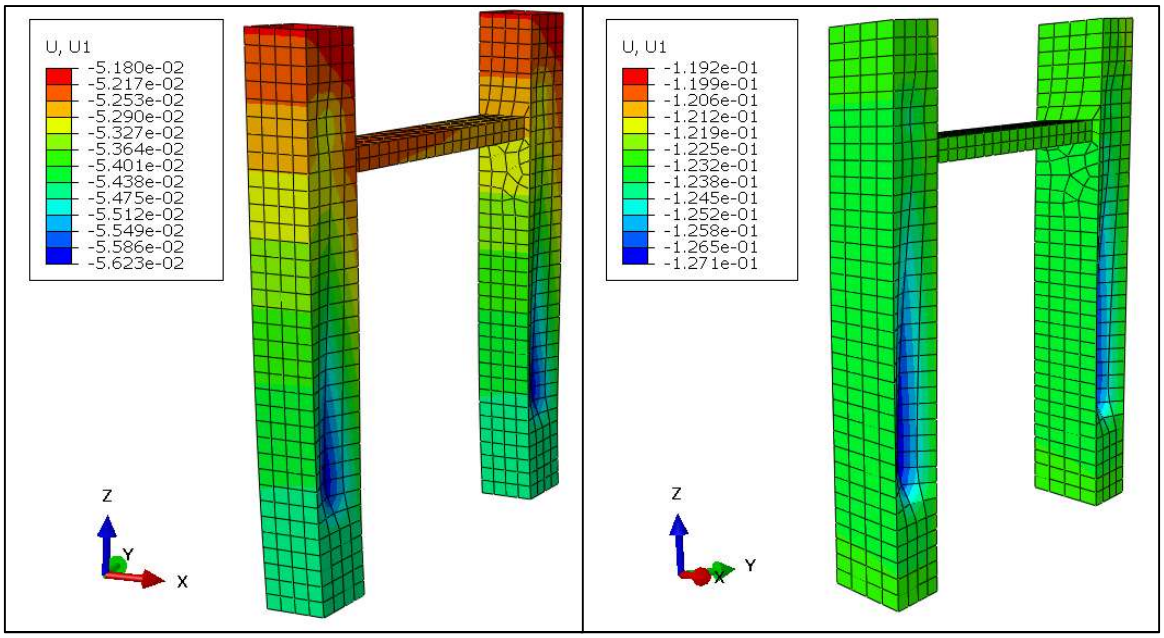

Figure 5.16. Horizontal movement contours of the vertical shafts at the peak force instant during the 50% motion (left) and 80% motion (right)

As it can be seen from figures 5.14 and 5.15, there is a sudden increase of the seismic soil pressure at the depth of 4.9 m which is the border between the soil layers. This increase is due to the higher stiffness of the bottom layer comparing to the top layer which results in stress concentration at this point. This phenomenon can also be seen in Figure 5.16, as the maximum deflection of the shafts occurs in the top layer around its border with the bedrock. The range of

numerical stresses is in good agreement with the experimental data for the 50% motion but is relatively higher at the peak force instant for the 80% motion (Figure 5.15b). In the E-Defense project, the 50% motion was performed prior to the 80% motion test. Densification of the sand layer due to the 50% motion test altered this layer's mechanical properties which consequently affected the induced seismic soil pressures in the 80% motion experiment. This change of soil parameters was not seen in the numerical modeling of the 80% Kobe motion and therefore, higher pressures were obtained for this test.

5.2.2. Parametric studies

After calibrating the numerical model, the model configuration (i.e., geometry and boundary conditions) and also the dynamic loading was kept constant and influence of the relative flexibility of the wall and the soil, d_w, and also the mechanical properties of the retained soil (i.e., cohesion and friction angle) on the distribution and magnitude of lateral seismic soil pressures were studied. It should be noted that due to the higher acceleration levels, the 80% scaled Kobe motion was used in this set of analyses. Aim of this part of the research was to investigate the effect of the aforementioned parameters on the dynamic response of the deep flexible structures located in dense urban areas which are under influence of their adjacent structures. Results of these analyses are presented in this section. It should be noted that the constitutive models of the soil materials were kept the same as the initial numerical models and in order to investigate the influence of cohesion and friction angle of the retained soil material, these Mohr-Coulomb parameters (i.e., c and φ) were converted to Drucker-Prager model parameters through Equations 4 and 5.

Besides the mechanical properties of the soil, relative flexibility of the wall and retained medium, d_w, and relative flexibility of the rotational base constraint and retained medium, d_θ, are

two important parameters that control the dynamic response of the retaining structures. These parameters as defined by Veletsos and Younan (1997) are presented in Equations 12 and 13.

$$d_w = \frac{GH^3}{D_w} \tag{12a}$$

$$D_w = \frac{E_w t_w^3}{12(1-\nu_w^2)} \tag{12b}$$

$$d_\theta = \frac{GH^2}{R_\theta} \tag{13}$$

Where, G is the retained soil average shear modulus, E_w and ν_w are the modulus of elasticity and Poisson's ratio of the wall, respectively, H is the wall height, and t_w is the wall thickness. R_θ is the rotational constraint stiffness of the wall's base.

In the E-Defense experiments, the vertical shafts of the test were fixed on the shake table and thereby the base constraint was rigid and $d_\theta = 0$. Since the model configuration was intended to be kept unchanged, the effect of d_θ was not studied in this section.

The thickness of the model shaft structures in E-Defense experiments was 12 mm. The effect of relative flexibility of the shafts' walls and the soil, d_w, was studied through variation of this parameter from 1/8 to 8 times of its initial value. This was done by analyzing three other models with shaft thicknesses of 6 mm, 18 mm and 24 mm which corresponded to $\frac{d_{w(new)}}{d_{w(initial)}}$ ratios of 8, 3.375, and 1/8, respectively. Comparison of the shaft's wall peak response under the 80% motion for these different thicknesses is presented in Figure 5.17. Figure 5.17a shows the seismic pressure distribution at the time of peak force for these cases. The profile of the horizontal displacement of

the shaft's wall relative to its base was also extracted for each case. These results are depicted in Figure 5.17b.

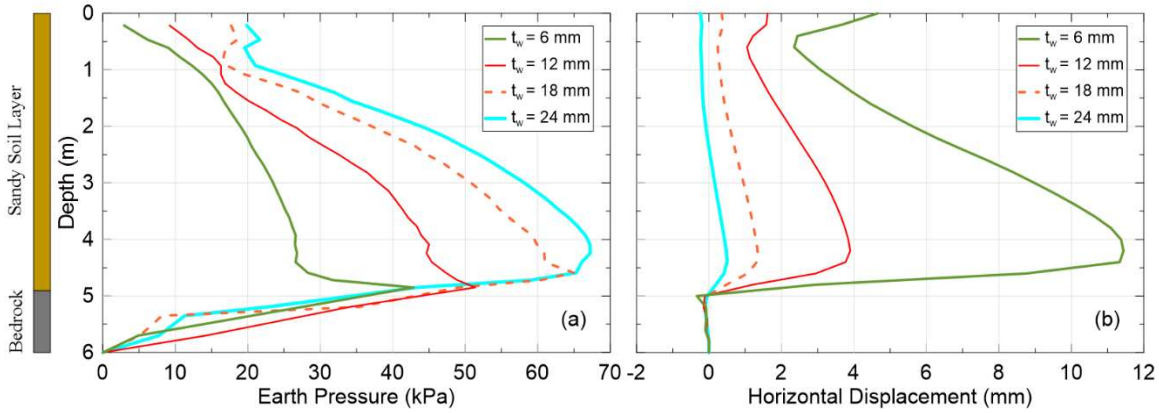

Figure 5.17. Comparison of the shaft's wall response under the 80% motion for different wall thicknesses: (a) seismic pressure distribution, (b) wall and adjacent soil displacement

As it can be seen from Figure 5.17, increase of the wall's thickness (rigidity) resulted in higher seismic pressures and as expected less deflection along the shaft's wall. Stiffer walls experienced more uniform deflection along their height and the difference of the wall's deflection in the sandy soil and the bedrock became less which resulted in smoother distribution of seismic soil pressure around the soil materials border. Moreover, as the walls became more flexible, the location of the maximum pressure moved slightly toward the base of the wall. Table 5.3 summarizes the resultant forces, their point of application and corresponding moments for the analyzed models with different thicknesses of the shaft's wall. Variation of the wall's thickness from 6 mm to 24 mm has increased the resultant force and moment by 107% and 124%, respectively.

Table 5.3. Summary of the results for different wall thicknesses

	Resultant Force (kN)	Point of Application (h/H)	Resultant Moment (kN.m)[a]
t_w = 6 mm	115.23	0.44	305.80
t_w = 12 mm	173.89	0.43	451.49
t_w = 18 mm	215.98	0.46	602.16
t_w = 24 mm	238.95	0.48	686.61

[a] Resultant Moment was calculated as the product of the resultant force and (h) with respect to the base

Next parameter which its effect was studied was the cohesion of the top layer. In these analyses, the cohesion, c, was normalized by the product of the unit weight of the top layer, $\gamma = 16.59\ {}^{kN}/_{m^3}$, and its thickness, H = 4.9 m. The normalized cohesion of the sandy soil used in the baseline numerical models was $\frac{c}{\gamma H} = 0.02$, and was considered equal to zero. Three other cases with $\frac{c}{\gamma H}$ of 0.1, 0.2, and 0.3 were also analyzed and their results were compared to each other. Comparison of the shaft's wall peak response under the 80% motion for these cases is presented in Figure 5. 28 in terms of distribution of seismic pressure and the wall's horizontal displacement.

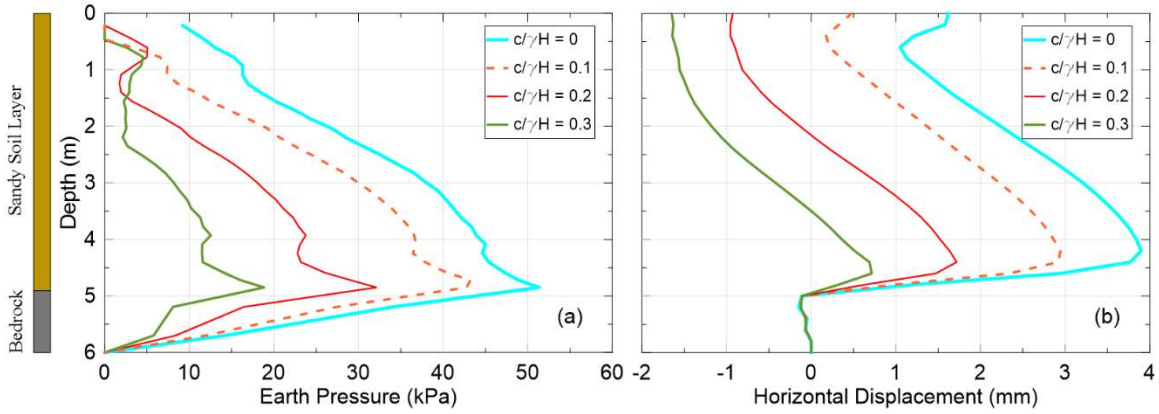

Figure 5.18. Comparison of the shaft's wall response under the 80% motion for different soil cohesions: (a) seismic pressure distribution, (b) wall and adjacent soil displacement

As it can be seen from Figure 5.18, the amplitude of seismic soil pressures along the wall's height decreased with the increase of the soil's cohesion and zero seismic pressures were obtained

for depths down to the 0.5 m below the ground surface (≈ 8% of the wall's height) for cohesion values above zero. It should be reminded that in the post-processing of the numerical results, tensile stresses have been regarded as unrealistic, and therefore, ignored (Psarropoulos et al., 2005). As it was also expected, the increase of the soil's cohesion resulted in less deflection along the shaft's wall height. The summary of results for the numerical models with different cohesion values is presented in Table 5.4. As it can be seen from this table, cohesion of the retained material has a significant influence on the magnitude of the resultant force and its corresponding moment. Increase of the $\frac{c}{\gamma H}$ from 0 to 0.3 led to decrease of the resultant force and moment by 70% and 81%, respectively. Moreover, by increasing the cohesion, the point of application of the resultant force moved toward the base of the wall.

Table 5.4. Summary of the results for different soil cohesion values

	Resultant Force (kN)	Point of Application (h/H)	Resultant Moment (kN.m)[a]
$c/\gamma H = 0$	173.89	0.43	451.49
$c/\gamma H = 0.1$	130.17	0.39	307.12
$c/\gamma H = 0.2$	78.58	0.37	176.19
$c/\gamma H = 0.3$	39.89	0.37	87.43

[a] Resultant Moment was calculated as the product of the resultant force and (h) with respect to the base

Last studied parameter in this section was the top layer's friction angle, φ°. The initial φ° used in the numerical analyses was 31°. Three other models with friction angles of 25°, 35°, and 45° were also analyzed and their results were compared to each other. These results are shown in Figure 5.19. As it is expected, increase of the friction angle as one of the main strength parameters of the soil, results in lower seismic pressures and deflection along the wall's height. Summary of the resultant forces and moments results is presented in Table 5.5. Variation of the friction angle from 25° to 45°, has decreased the resultant force and moment by 48% and 51%, respectively.

Although the increase of the friction angle has slightly moved the point of application of the resultant force toward the wall's base but compared to the soil material's cohesion, this movement is lower.

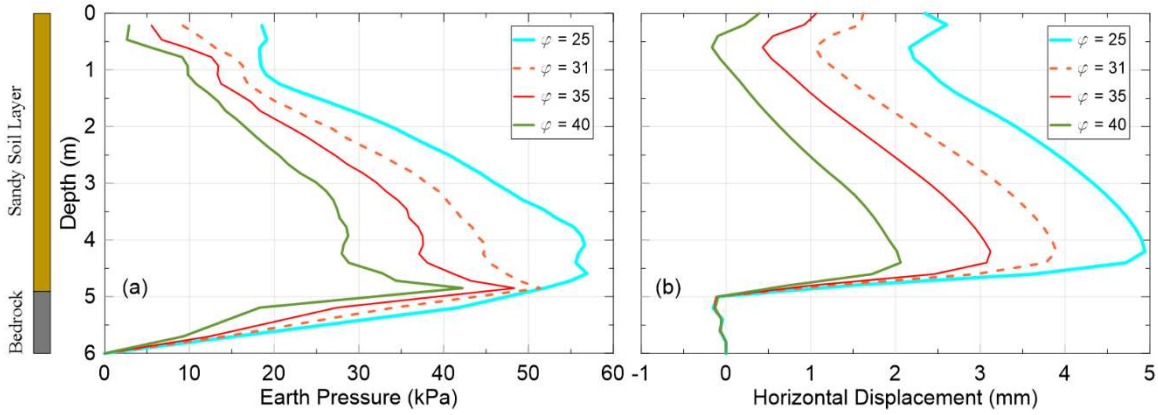

Figure 5.19. Comparison of the shaft's wall response under the 80% motion for different soil friction angles: (a) seismic pressure distribution, (b) wall and adjacent soil displacement

Table 5.5. Summary of the results for different soil friction angle values

	Resultant Force (kN)	Point of Application (h/H)	Resultant Moment (kN.m)[a]
φ° = 25	214.33	0.45	572.68
φ° = 31	173.89	0.43	451.49
φ° = 35	146.07	0.43	372.58
φ° = 40	110.95	0.42	279.45

[a] Resultant Moment was calculated as the product of the resultant force and (h) with respect to the base

5.2.3. Extended set of parametric studies

In this step a simplified 3D soil-structure system was used to investigate the effect of the most important parameters that are believed to govern the distribution and magnitude of seismic soil pressures on deep underground structures. The aim of this section was to provide normalized graphs that could be utilized to predict seismically induced soil pressures on deep underground structures considering the 3D effects, nonlinear behavior of the retaining soil, flexibility of the structure relative to the retained soil, amplitude of the applied motion and also the role of the layer

overlain by the structure. In order to have a more comprehensive insight into the problem, the Veletsos and Younan (1997) method as the only 2D approach which takes into account the flexibility of the wall and its base was also used in the performed numerical study. For this purpose, in addition to the 3D soil-structure system, a 2D model was developed based on the finite element method by Psarropoulos et al. (2005), a more general form of the analytical solution by Veletsos and Younan (1997), and its results were also included in the analyses.

5.2.3.1. The 3D model configuration, boundary conditions, and elements

The model configuration, boundary conditions, and utilized element types are shown in Figure 5.20. The depth of the analyzed structure was selected 13 m which was almost equal to the depth used by Wagner and Sitar (2016) in their study of seismic soil pressures on deep stiff walls (13.3 m). In order to consider the 3D effects, Length of the structure was set equal to its depth ($\frac{\mathrm{L}}{\mathrm{H}} = 1$). The wall's foundation rotational and translational stiffnesses are usually modeled through simple elastic springs (e.g. Veletsos and Younan 1997, Jung and Bobet 2008, Wilson 2009). In this research, a separate visco-elastic infinite soil layer with a thickness of 4 m, foundation soil, was used beneath the retained soil medium to represent the wall's base more realistically. The structure and soil materials were modeled using 8-node linear brick, reduced integration solid elements (C3D8R). Far-field soil materials were represented by 8-node linear one-way infinite brick elements (CIN3D8). Infinite elements are based on the work of Lysmer and Kuhlemeyer (1969) and are used to account for the energy absorption from the unbounded soil medium (i.e., radial damping). Infinite elements provide quiet boundaries to the finite element model through the effect of a damping matrix; the stiffness matrix of the element is suppressed. These elements keep the static force present at the start of the dynamic response analysis on this boundary; therefore, the far-field nodes in the infinite elements will not displace during the seismic step.

The accuracy of the finite element analysis of seismic problems is controlled by the maximum element size, boundary conditions and scale of the finite domain (Zhang and Tang, 2007). The absorbing boundaries (i.e., infinite elements) were put far enough from the structure to minimize the numerical oscillations. The maximum utilized element size in numerical models, l_{max}, was also selected based on recommendations by Kuhlemeyer and Lysmer (1973) and Lysmer et. al (1975) who suggested that:

$$l_{max} \leq \left(\frac{1}{8} \sim \frac{1}{5}\right) L \tag{14}$$

Where, L is the shear wave length.

The base excitation was introduced by a prescribed harmonic acceleration time history on the base of the model (Eq. 15). Considering the natural frequencies of the soil materials used in the analyses, and in order to avoid dynamic amplification, excitation frequency of 1 Hz was adopted in this study.

$$a(t) = k_h g \sin(\omega t) \tag{15}$$

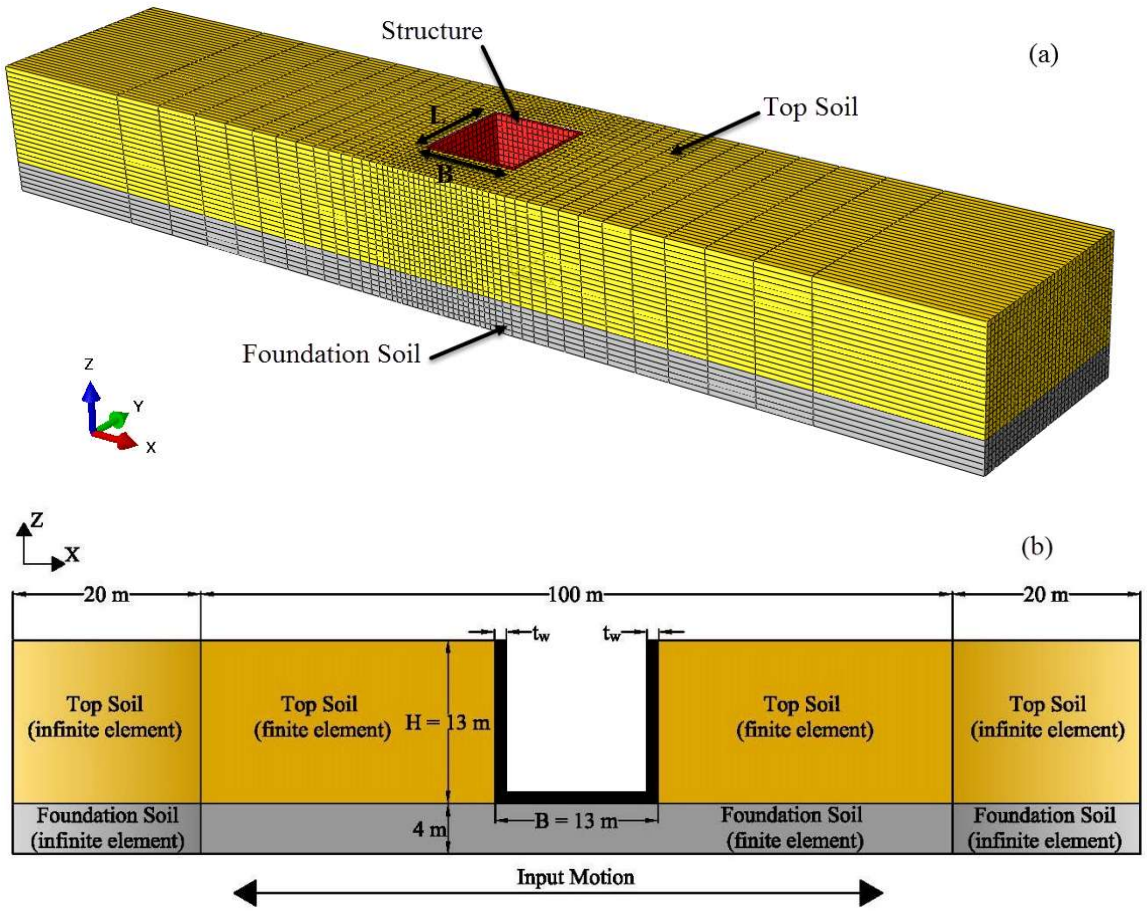

Figure 5.20. Simplified soil-wall system utilized in the analyses: (a) the adopted finite element model, (b) boundary conditions and element types (dimensions not to scale)

The soil-structure interaction simulation was conducted through the same approach explained in section 5.3.1.4.

5.2.3.2. Studied cases through the 3D numerical analyses

The effect of soil mechanical properties on the distribution and magnitude of seismic induced soil pressures were investigated in terms of the soil's cohesion, c, and friction angle, φ. The relative flexibility of the wall and the retained soil, d_w, and relative flexibility of the wall's base rotational constraint and retained soil, d_θ, were two parameters which were chosen to study the role of the structure's flexibility on the results. d_w value was altered between 5 (rigid wall) to 50 (flexible wall) through changing the thickness of the structure's wall. d_θ was also varied between 0 (stiff

base) to 4 (soft base). Keeping the width of the wall, B, constant, the length/height, $\frac{L}{H}$, ratio was varied to consider for the effect of the wall's geometry. The earthquake acceleration amplitude, $k_h = \frac{a_h}{g}$, was the last parameter which its influence was studied in this research. To evaluate the effect of each of the aforementioned parameters on the seismic soil pressures behind the wall, the other parameters were kept constant.

It should be noted that the influence of soil parameters (i.e., c, and φ), $\frac{L}{H}$ ratio, and k_h were looked into for two extreme cases: a flexible wall on a soft soil foundation (d_w = 50, d_θ = 4) and a rigid wall on a stiff base (d_w = 5, d_θ = 0). Finally, the effects of d_w and d_θ were examined for both of the extreme cases of the other one. The analyzed parameters are summarized in Table 5.6.

Except for the models used to study the effect of k_h, in which this parameter was varied between 0.2 and 1, the utilized earthquake acceleration amplitude, $k_h = \frac{a_h}{g}$, was kept 0.4 for all other studied parameters.

Table 5.6. Analyzed parameters in parametric studies

Wall/Base Flexibility Condition	Changing Parameter	Symbol	Varied Values				
Rigid Wall - Stiff Base (d_w = 5, d_θ = 0) Flexible Wall - Soft Base (d_w = 50, d_θ = 4)	Cohesion	$c/\gamma_s H$*	0	0.05	0.1	0.2	0.3
Rigid Wall - Stiff Base (d_w = 5, d_θ = 0) Flexible Wall - Soft Base (d_w = 50, d_θ = 4)	Friction Angle	φ°	20	30	35	40	45
Stiff Base (d_θ = 0) Soft Base (d_θ = 4)	Wall Flexibility	d_w	5	10	25	40	50
Rigid Wall (d_w = 5) Flexible Wall (d_w = 50)	Base Flexibility	d_θ	0	0.5	1	2	4
Rigid Wall - Stiff Base (d_w = 5, d_θ = 0) Flexible Wall - Soft Base (d_w = 50, d_θ = 4)	Wall Length/Wall Height	L/H	1	1.5	2	-	-
Rigid Wall - Stiff Base (d_w = 5, d_θ = 0) Flexible Wall - Soft Base (d_w = 50, d_θ = 4)	Earthquake Acc. Amplitude	k_h	0.2	0.4	0.6	0.8	1

* Cohesion of the retained soil material was normalized with respect to the product of its unit weight, γ_s, and thickness, H.

5.2.3.3. Material models used in the 3D numerical analyses

The top soil material (i.e., retained medium) was modeled as a nonhomogeneous viscoelastic-plastic material using the Mohr-Coulomb failure criteria. Soil is not a homogeneous medium and the assumption of uniform shear modulus with depth is not realistic. The dependence of the soil's shear modulus on mean effective stress has been the topic of many studies and a number of empirical and theoretical equations have been developed to address this issue (e.g., Hardin and Richart 1963, Hardin and Drnevich 1972, and Yamada et al. 2008). The formulation of the soil's shear modulus as a function of depth instead of mean effective stress is an alternate approach which has been used by many researchers (e.g., Wood 1973, Veletsos and Younan 1994). Rovithis et al. (2011), suggested an equation for the formulation of shear wave velocity as a function of depth. Brandenberg et al. (2017), adapted this equation to be used for the shear modulus (Eq. 16).

$$G(z) = G_r \left[b + (1 - b)\frac{z}{z_r}\right]^{2n} \tag{16a}$$

$$b = \left(\frac{V_0}{V_r}\right)^{1/n} \tag{16b}$$

Where, $G(z)$ is the shear modulus at the depth of z measured from the ground surface, n is a dimensionless inhomogeneity factor, G_r, V_r, and z_r stand for a reference shear modulus, reference shear wave velocity, and a reference depth, respectively. V_0 is the shear wave velocity at the ground surface. Setting z_r equal to final depth of the layer, H, the Equation 16a can be rewritten as:

$$G(z) = G_H \left[b + (1 - b)\frac{z}{H}\right]^{2n} \tag{17}$$

In this research, b was set to zero and following Rovithis et al. (2011), $n = 0.25$. In ABAQUS, the continuous shear modulus profile in the top layer (i.e., retained medium), G(z), was approximated through a fine discretization which is shown in Figure 5.21. The average shear wave velocity, $\overline{V}_s$, and unit density of the top layer, ρ, were assumed to be 130 m/s and 1800 kg/m^3, respectively. Using these values and Equation 17, variation of the shear modulus with depth was defined for this layer. For the cases which the Mohr-Coulomb parameters (i.e., cohesion, and friction angle) were not the subject of the study, these parameters were selected as $c / \gamma_s H = 0.05$, and φ = 35° which were assumed to be representative of typical backfill materials. $c / \gamma_s H$ is the cohesion of the retained material normalized with respect to the product of its unit weight, γ_s, and thickness, H.

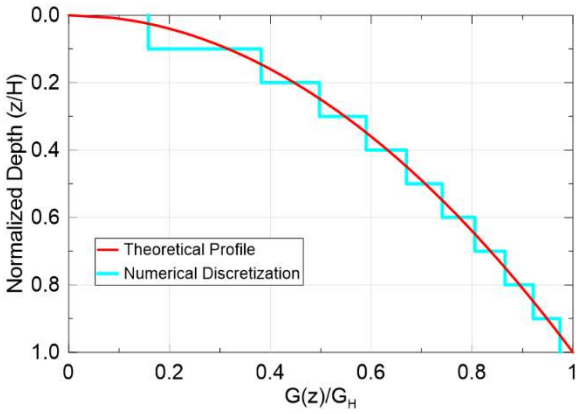

Figure 5.21. Shear modulus variation within the inhomogeneous layer

As it was mentioned earlier, the foundation soil layer was defined as a homogeneous visco-elastic material with a constant thickness of 4 m. In the study the effect of the relative flexibility of the wall's base rotational constraint and retained soil, d_θ, the rotational stiffness of the base, R_θ, was expressed through Equation 18 proposed by Gazetas (1991). In this equation, G_f, ν_f, and t_f,

are shear modulus, Poisson's ratio and thickness of the foundation layer, respectively. The shear modulus of the foundation layer was varied for cases with different d_θ values.

$$\frac{R_\theta}{2L} = \frac{\pi G_f B^2}{8(1-\nu_f)}\left(1 + 0.1\frac{B}{t_f}\right) \quad (18)$$

Due to the suppression of the infinite elements stiffness matrix during the seismic motion, finite elements located adjacent to the boundary of infinite elements are not provided with confinement pressures. This issue does not affect the materials simulated through the traditional linear elastic constitutive model but for elastic-plastic material models, in which the soil stiffness is dependent on the amount of confinement pressure, these boundaries may trigger early yielding and consequently excessive deformation of the boundary elements. To account for this problem, lateral boundaries of the finite domain were placed far away from the structure (i.e., 50 m from each side). However, this configuration may still result in unrealistically high seismic soil pressures for cases with weak retained soil material (i.e., low cohesion and friction angle). This result was observed during the numerical simulations for the cases of soil with cohesion of 20 kPa and friction angle of 20°. Hence the reader is advices to use the results from this specific simulation carefully until further validation by the authors of this thesis is provided.

Another approach for modeling of the side boundary conditions which restricts the lateral deflection, is the use of kinematic tie constraints, which force the opposite vertical sides to move simultaneously (Chen et al. 2012, Tsinidis et al. 2016). This methodology is particularily suitable for simulating the container effects through 2D numerical analysis of shake table and centrifuge experiments. Utilizing of this approach in modeling of unbound fields under seismic motions,

results in negligence of the inertial and stiffness effects of the far-field soil domain and therefore was not used in this research.

Rayleigh damping was adopted for the soil materials. Due to the frequency-dependency of the Rayleigh parameters (α and β), natural frequencies govern the accuracy of the damping function and should be defined precisely. The analyzed problem had a two-layered soil profile in which the foundation soil layer's stiffness was varied for cases with different d_θ values. Natural frequencies of the soil system were calculated for each case separately, through the natural frequency extraction analysis offered by ABAQUS. The frequency extraction is a linear perturbation procedure which uses the Lanczos method to extract the eigenvalues of the system and calculate the natural frequencies and corresponding mode shapes of a system. Considering a damping ratio of 7% for the first two modes of vibration of the soil profile, Rayleigh parameters were calculated for different d_θ values and are presented in Table 5.7.

Table 5.7. Natural frequencies and Rayleigh parameters calculated for the soil profile for different d_θ values

d_θ	1st Natural Frequency (Hz)	2nd Natural Frequency (Hz)	Mass Damping Factor (α)	Stiffness Damping Factor (β)
0	2.74	7.19	1.7427	0.0022
0.5	2.42	6.35	1.5433	0.0025
1	2.17	5.79	1.3882	0.0028
2	1.82	5.27	1.1874	0.0031
4	1.44	4.91	0.9809	0.0035

The structural elements were modeled using visco-elastic constitutive model. Structure damping ratio was considered equal to 3% and was modeled through the Rayleigh damping. For cases with different d_w values, the modulus of elasticity of the structure was kept constant and the thickness of the wall was varied. Utilizing the natural frequency extraction analysis, first and

second natural frequencies and the Rayleigh parameters were obtained for each case separately and are presented in Table 5.8.

Table 5.8. Natural frequencies and Rayleigh parameters calculated for the structure for different d_w values

d_w	1st Natural Frequency (Hz)	2nd Natural Frequency (Hz)	Mass Damping Factor (α)	Stiffness Damping Factor (β)
5	4.14	5.53	0.8925	0.001
10	3.34	4.35	0.7118	0.0012
25	2.69	3.34	0.569	0.0016
40	2.63	3.29	0.5513	0.0016
50	1.97	2.66	0.4269	0.0021

Table 5.9 shows the properties of the structure and soil materials which were kept constant for all of the numerical models.

Table 5.9. Geometrical and mechanical properties of the structure and soils kept constant in all numerical models

	Parameter	Symbol	Value	Unit
Top Layer (Retained Soil)	Unit Density	ρ_s	1800	kg/m^3
	Poisson's Ratio	ν_s	0.33	-
	Average Shear Wave Velocity	$\overline{V}s$	130	m/s
	Damping Ratio	ζ_s	7	%
Bottom Layer (Foundation Soil)	Thickness	t_f	4	m
	Unit Density	ρ_f	1800	kg/m^3
	Poisson's Ratio	ν_f	0.33	-
	Damping Ratio	ζ_f	7	%
Structure	Height	H	13	m
	Width	B	13	m
	Unit Density	ρ_w	2400	kg/m^3
	Modulus of Elasticity	E_w	210	GPa
	Poisson's Ratio	ν_w	0.2	-
	Damping Ratio	ζ_w	3	%

5.2.3.4. The 2D plane-strain numerical analyses and results

The 2D numerical approach by Psarropoulos et al. (2005) was used in the analysis of the two extreme cases: a flexible wall on a soft soil foundation ($d_w = 50$, $d_\theta = 4$) and a rigid wall on a stiff base ($d_w = 5$, $d_\theta = 0$). The compliance of the utilized 2D numerical models with the Psarropoulos et al. (2005) approach, had to be verified first. Therefore, a similar model to the problem studied by them was developed (Figure 5.22). The mechanical and geometrical properties of the materials and the ground motion acceleration were selected based on their study and are presented in Table 5.10.

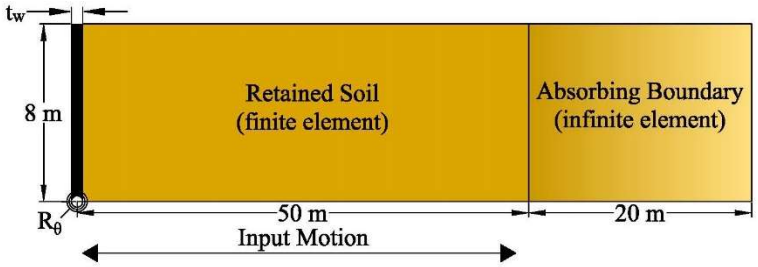

Figure 5.22. The 2D model similar to the problem studied by Psarropoulos et al. (2005)

Table 5.10. Geometrical and mechanical properties utilized in the 2D model similar to the problem studied by Psarropoulos et al. (2005)

	Parameter	Symbol	Value	Unit
Ground Motion	Acc. Amplitude	k_h	0.1	g
	Frequency	f	0.5	Hz
Retained Soil	Unit Density	ρ_s	1800	kg/m^3
	Poisson's Ratio	ν_s	0.33	-
	Shear Wave Velocity	V_s	100	m/s
	Damping Ratio	ζ_s	5	%
Wall	Height	H	8	m
	Width	B	0.2	m
	Unit Density	ρ_w	2500	kg/m^3
	Poisson's Ratio	ν_w	0.2	-
	Damping Ratio	ζ_w	2	%

The Wall was modeled through 2-node linear beam elements (B21) with a unit longitudinal length. A rotational spring with a stiffness of R_θ was placed at the bottom of the wall. The R_θ was defined based on the assumed d_θ value for each of the analyzed cases through Equation 13. The retained soil was simulated through the 4-node bilinear quadrilateral reduced integration plane-strain elements (CPE4R). Psarropoulos et al. (2005) used vertical and horizontal viscous dashpots to simulate the radiation of energy. In this study, 4-node linear one-way infinite plane-strain elements (CINPE4) were utilized to consider for the absorbing boundaries. The input motion was applied at the base of the retained soil layer. Regarding the soil-wall interaction, it was assumed that neither de-bonding, nor relative slippage occurs. In total, four cases with different wall and base flexibilities (d_w and d_θ) were modeled and their results were compared with their counterparts obtained from the analytical solution by Veletsos and Younan (1997) and numerical method by Psarropoulos et al. (2005). Distribution of seismic wall pressures for these cases are shown in Figure 5.23. The pressure values were normalized with respect to $k_h\gamma_s H$, where all of the parameters have been defined before. The y-coordinates along the wall's height were also normalized with respect to the wall's height as y/H. As it can be seen from this figure, seismic soil pressures calculated in the current study are in good agreement with both of the previous studies for every combination of flexibilities. However, there is a discrepancy between the numerical results and the analytical approach near the top of the wall. This issue is a result of the concave deviation of the distributions resulting from the numerical solution while approaching the free surface. This phenomenon characterizes numerical solutions (Psarropoulos et al. 2005, Wood 1975).

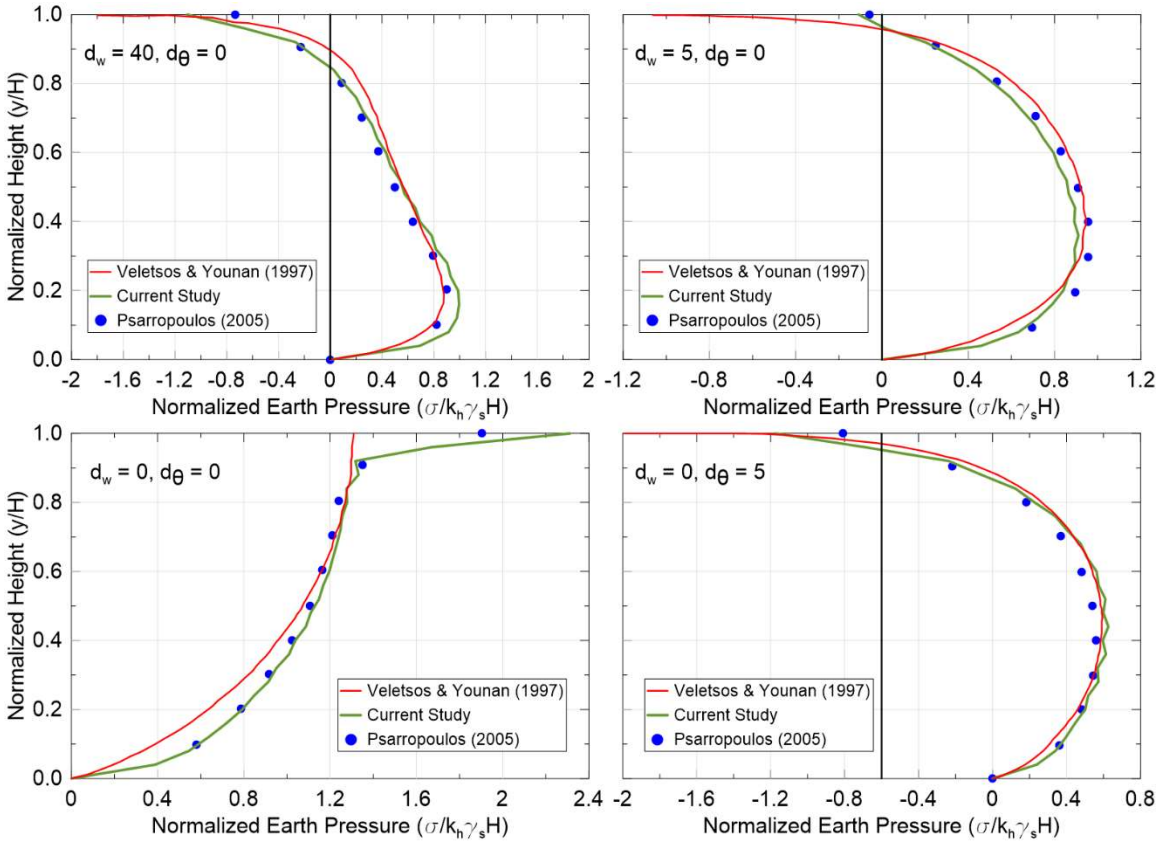

Figure 5.23. Comparison of the distribution of the seismic soil pressures on the wall obtained from current study and those obtained by Veletsos and Younan (1997) and Psarropoulos et al. (2005)

After verification of the 2D model to be complied with the aforementioned methods, geometrical and material properties of the retained soil and the wall were changed to the values used in the current study (Table 5.9). It should be noted that in the 2D models, the retained soil was considered as a homogeneous material with a constant shear modulus along its depth (using the $\overline{V}s$). Two extreme cases of (d_w = 50, d_θ = 4) and (d_w = 5, d_θ = 0) were analyzed. Figure 5.24 depicts the normalized distribution of seismic soil pressures on the wall for these two cases. It is noteworthy to mention that all of the presented seismic soil pressure profiles are at the instant of peak force applied on the wall during the input motion. These profiles were used to calculate the resultant seismic forces and moments which were later compared with the 3D models' results. For the wall with (d_w = 50, d_θ = 4), the normalized seismic pressures resultant force, $\frac{\Delta P_E}{k_h \gamma_s H^2}$, exerted on the

wall, and its normalized corresponding resultant seismic moment, $\frac{\Delta M_E}{k_h \gamma_s H^3}$, were calculated to be 0.26 and 0.10, respectively. $\frac{\Delta P_E}{k_h \gamma_s H^2}$, and the $\frac{\Delta M_E}{k_h \gamma_s H^3}$ were 0.69 and 0.31 for the wall with (d_w = 5, d_θ = 0), respectively. In the post-processing of the numerical results (i.e., calculation of resultant forces and moments), tensile stresses were regarded as unrealistic, and therefore, ignored (Psarropoulos et al., 2005).

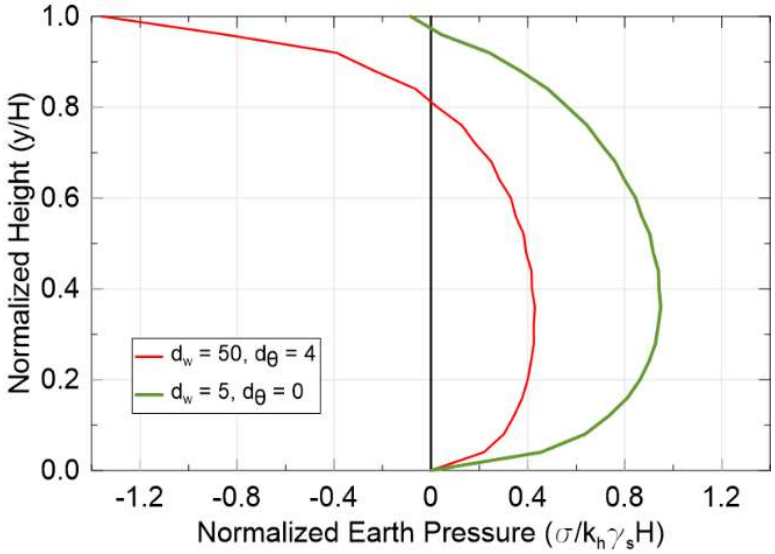

Figure 5.24. Distribution of normalized seismic soil pressures on the wall using the 2D approach for a flexible wall on a soft soil foundation (d_w = 50, d_0 = 4) and a rigid wall on a stiff base (d_w = 5, d_0 = 0)

5.2.3.5. 3D numerical analyses results and discussion

Results of the performed parametric studies are presented and discussed in terms of the magnitude and distribution of seismic soil pressures, resultant seismic forces and moments, and the wall's relative displacement to its base. These results are presented hereafter for each of the varied parameters (Table 5.6) separately. It should be noted that in the numerical simulations, distribution of seismic soil pressures was obtained directly from the contact stresses (CPRESS) between the soil and structural elements. Presented results correspond to the centerline of the

structure's wall (i.e., L/2) which had the maximum structural deflections and was believed to be the most critical section in the structural design of the wall.

Retained material cohesion

The normalized cohesion of the retained soil material, $c/\gamma_s H$, was varied from 0 to 0.3 for each of the extreme cases of ($d_w = 50$, $d_\theta = 4$) and ($d_w = 5$, $d_\theta = 0$). Figure 5.25 shows the normalized seismic pressures resultant force, $\frac{\Delta P_E}{k_h \gamma_s H^2}$, exerted on the wall during the excitation for different analyzed cases. At the instant of the peak resultant force, Figure 5.26 depicts the normalized seismic soil pressure distributions along the wall's height, $\frac{\sigma}{k_h \gamma_s H}$, and Figure 5.27 presents the profiles of the horizontal displacement of the wall relative to its base. The variations of the normalized seismic resultant force, $\frac{\Delta P_E}{k_h \gamma_s H^2}$, and normalized corresponding resultant seismic moment, $\frac{\Delta M_E}{k_h \gamma_s H^3}$, against the normalized cohesion of the retained soil material, $c/\gamma_s H$, for two extreme cases of ($d_w = 50$, $d_\theta = 4$) and ($d_w = 5$, $d_\theta = 0$) are shown in Figure 5.28.

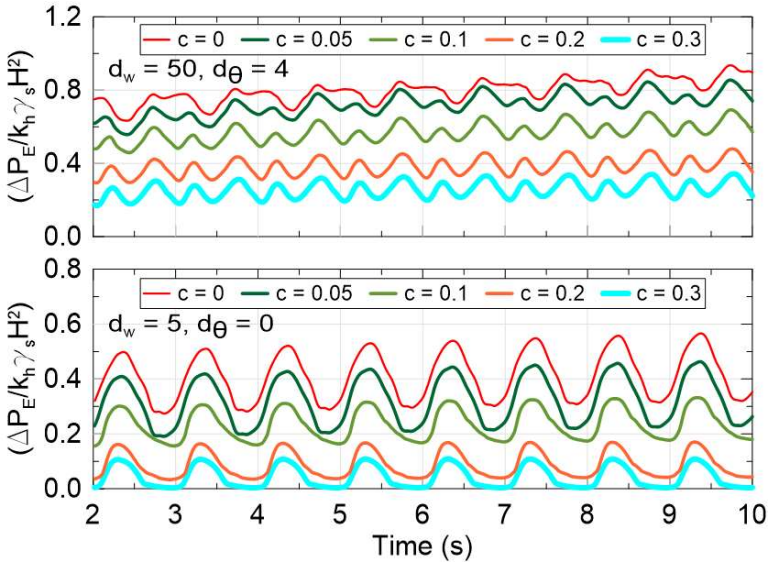

Figure 5.25. Normalized seismic resultant force time history for cases with different retained soil cohesion values

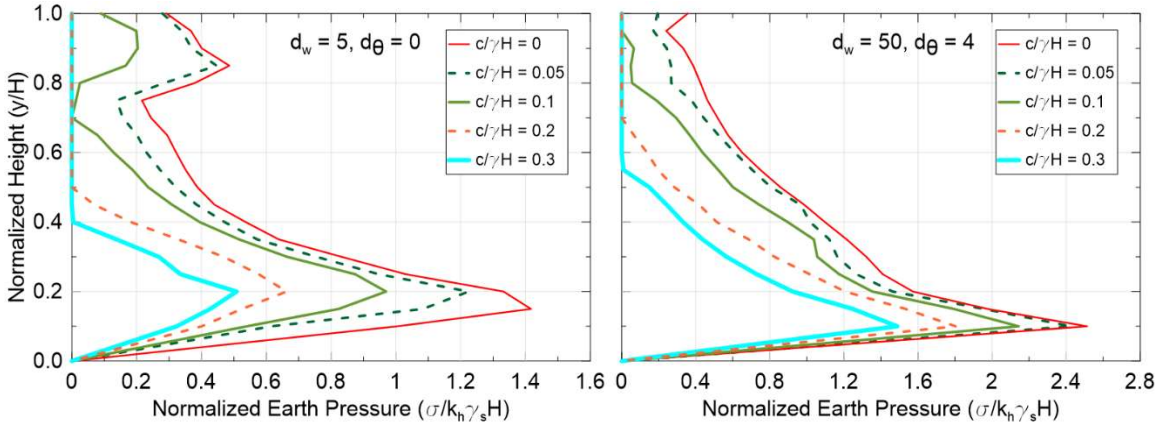

Figure 5.26. Normalized distribution of seismic soil pressures for cases with different retained soil cohesion values

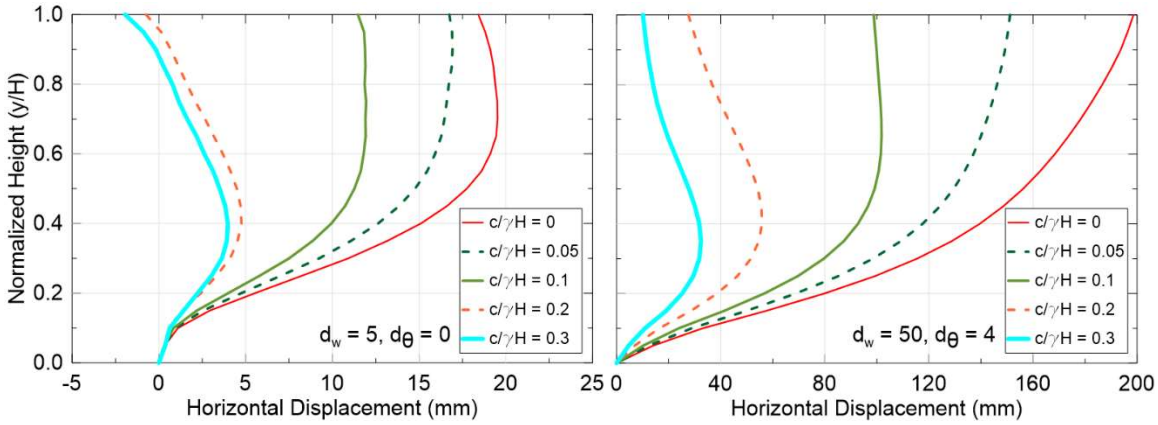

Figure 5.27. Wall and adjacent soil displacements for cases with different retained soil cohesion values

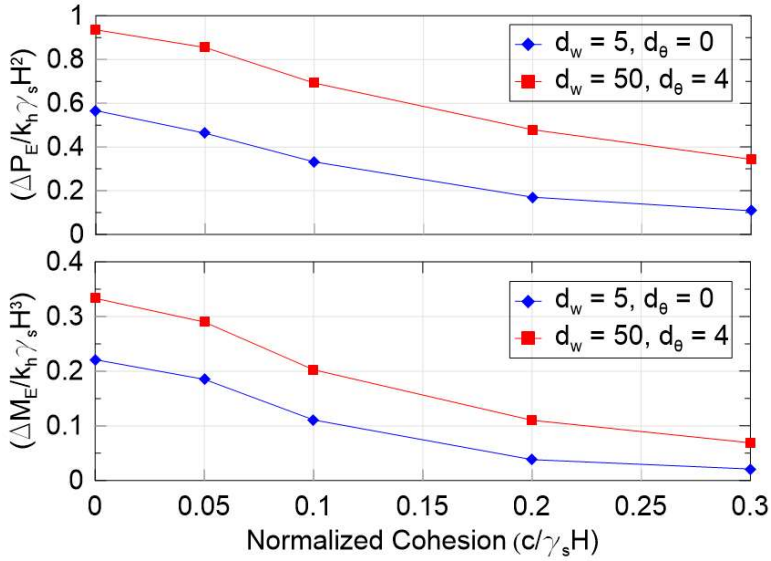

Figure 5.28. Normalized variation of the resultant seismic force and moment against the retained soil cohesion

As it is expected, the increase of the retained soil's cohesion results in lower seismic stresses and therefore in lower resultant forces and moments regardless of the wall and the base flexibilities. For the flexible wall on a soft base, (d_w = 50, d_θ = 4), the variation of the $c/\gamma_s H$ from 0 to 0.3, decreases the resultant seismic force and moment by 63.32% and 79.25%, respectively. These decrease percentages are 80.87% and 90.50% for the resultant seismic force and moment for rigid wall located on a stiff base, (d_w = 5, d_θ = 0). According to FEMA 750 (2009), the ratio of the displacement of the tip of the wall to its height, $\frac{\Delta h}{H}$, is an important parameter which determines the type of the wall to be "yielding" or "non-yielding", the latter one applies when $\frac{\Delta h}{H} > 0.002$. Increase of the $c/\gamma_s H$ from 0 to 0.3, decreases the $\frac{\Delta h}{H}$ from 0.153 to 0.008 for the wall with (d_w = 50, d_θ = 4). This ratio changes from 0.014 to 0.001 for the wall with (d_w = 5, d_θ = 0) which based on the FEMA 750, 2009, implies that the behavior of the wall changes from yielding to non-yielding. Therefore, the seismic behavior of the embedded wall regarding the induced soil pressures and wall's deflection, is considerably affected by the retained soil's cohesion and this parameter should not be ignored in the seismic analysis of underground structures.

Retained material friction angle

The friction angle of the retained soil, was varied from 20° to 45° for each of the extreme cases of (d_w = 50, d_θ = 4) and (d_w = 5, d_θ = 0). The obtained results are shown in Figures 5.29 to 5.32.

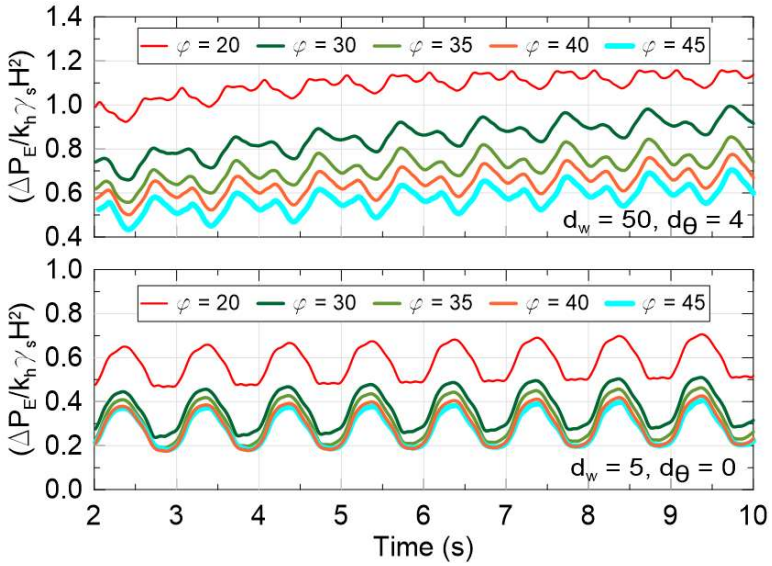

Figure 5.29. Normalized seismic resultant force time history for cases with different retained soil friction angles

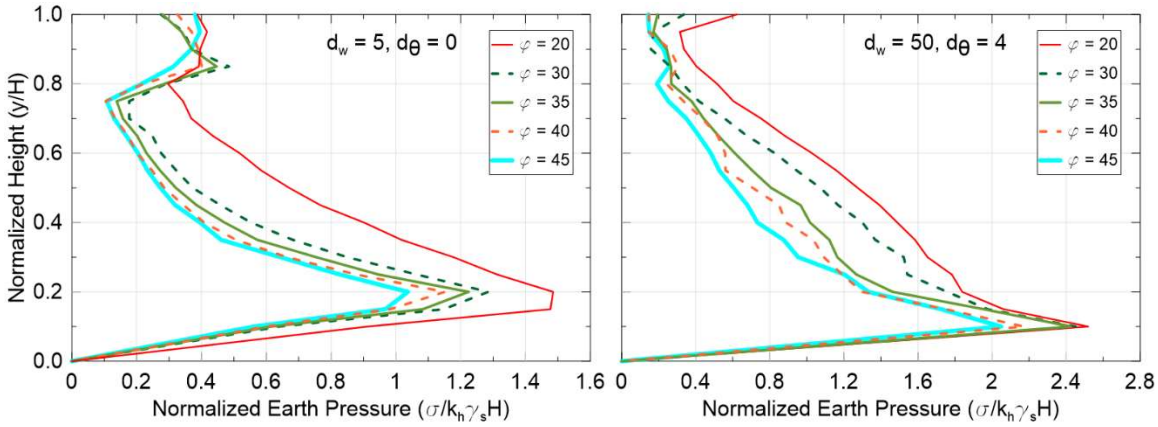

Figure 5.30. Normalized distribution of seismic soil pressures for cases with different retained soil friction angles

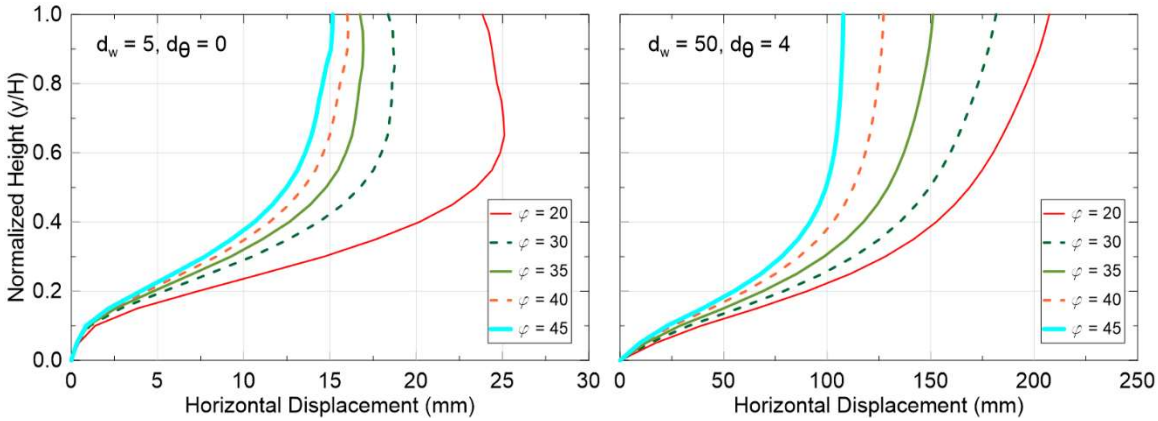

Figure 5.31. Wall and adjacent soil displacements for cases with different retained soil friction angles

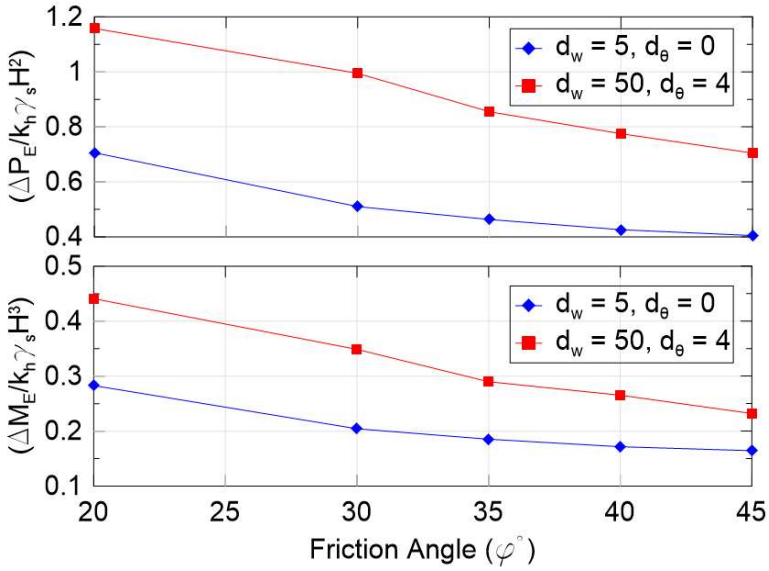

Figure 5.32. Normalized variation of the resultant seismic force and moment against the retained soil friction angles

As it can be seen from the graphs, increase of the friction angle as one of the main strength parameters of the retained soil, decreases the induced seismic soil pressures and wall's displacements for both of the wall/base flexibility combinations. Changing the friction angle from 20° to 45°, decreases the exerted seismic force and its corresponding moment on the wall with (d_w = 50, d_θ = 4) by 39.12% and 47.35%, respectively. For the rigid wall located on a stiff base, (d_w = 5, d_θ = 0), these force and moment reductions are 42.69% and 41.84%, respectively. Moreover, the increase of friction angle from 20° to 45°, reduced the $\frac{\Delta h}{H}$ from 0.159 to 0.083 for the wall with (d_w = 50, d_θ = 4). This ratio changes from 0.018 to 0.012 for the wall with (d_w = 5, d_θ = 0). Comparison of the results obtained from numerical analyses of the influence of the cohesion and friction angle, shows that the cohesion has a more significant effect on the seismic behavior of the wall concerning induced seismic soil pressures and wall's deflection.

Wall flexibility

The relative flexibility of the wall and the retained soil, d_w, was varied between 5 (rigid) to 50 (flexible) for each of the base conditions: stiff base, $d_\theta = 0$, and soft base, $d_\theta = 4$. Figure 3.33 shows the normalized resultant force time history for the analyzed cases.

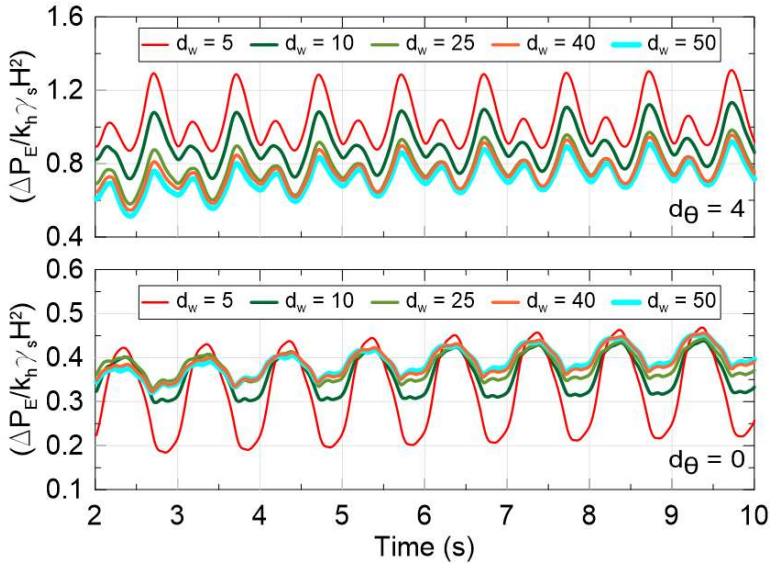

Figure 5.33. Normalized seismic resultant force time history for cases with different wall flexibilities

The profile of normalized seismic pressures along the wall's height and the horizontal displacement of the wall relative to its base for different analyzed cases at the instant of the maximum resultant seismic force are presented in Figures 5.34 and 5.35. Figure 5.36 depicts the variations of the normalized seismic resultant force, $\frac{\Delta P_E}{k_h \gamma_s H^2}$, and normalized corresponding resultant seismic moment, $\frac{\Delta M_E}{k_h \gamma_s H^3}$, against the wall flexibility, d_w, for two base conditions of stiff base, $d_\theta = 0$, and soft base, $d_\theta = 4$.

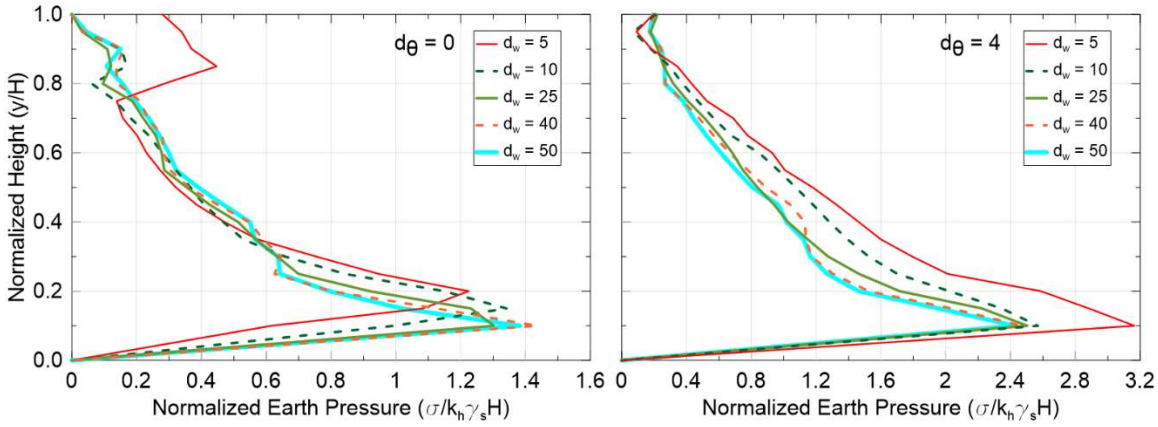

Figure 5.34. Normalized distribution of seismic soil pressures for cases with different wall flexibilities

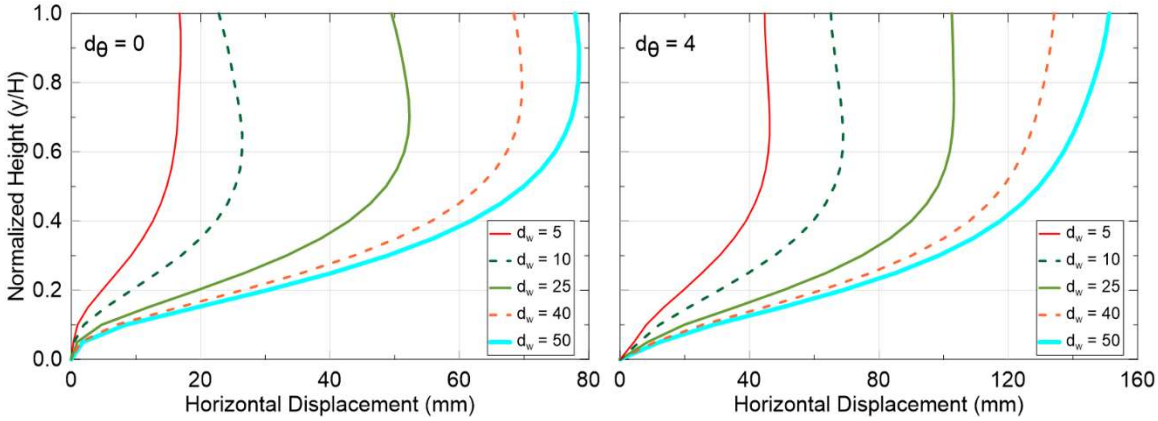

Figure 5.35. Wall and adjacent soil displacements for cases with different wall flexibilities

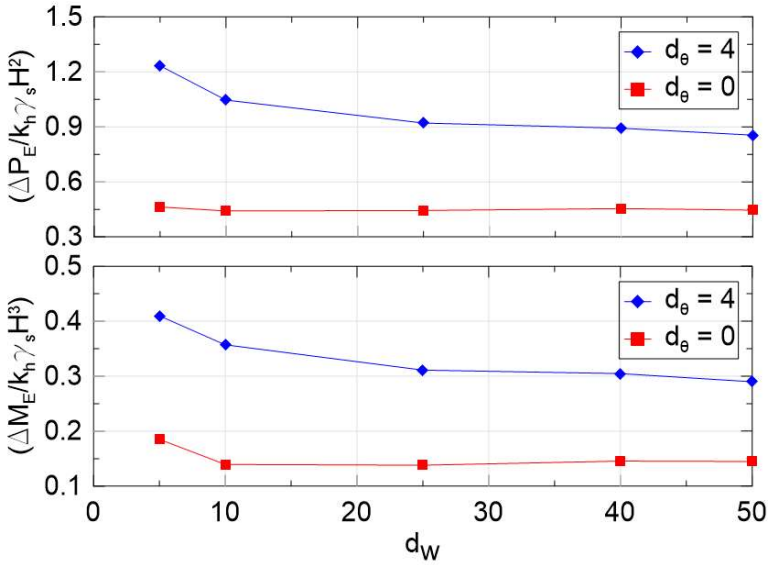

Figure 5.36. Normalized variation of the resultant seismic force and moment against the wall flexibility

For the walls located on a stiff base, $d_\theta = 0$, the influence of the wall's flexibility on the exerted seismic forces and their corresponding moments is negligible; the increase of the d_w from 5 to 50 only changes the $\frac{\Delta P_E}{k_h \gamma_s H^2}$ for less than 3.70 % ; regarding the resultant seismic moment, $\frac{\Delta M_E}{k_h \gamma_s H^3}$, there is a decrease of 24.63% by varying the d_w from 5 to 10 which is also recognizable from Figure 5.34 as the maximum pressure moves toward the base of the wall; the $\frac{\Delta M_E}{k_h \gamma_s H^3}$ remains almost the same for flexibilities between $d_w = 10$ to $d_w = 50$, with the maximum difference of 5.22%.

The effect of the wall's flexibility on the exerted seismic forces and their corresponding moments is more pronounced for walls located on a soft soil, $d_\theta = 4$; the variation of the d_w from 5 to 50, decreases the resultant seismic force and moment by 30.65% and 29.26%, respectively. This shows that the influence of the wall's flexibility on the seismic soil pressures increases with the decrease of the foundation soil's stiffness and higher wall flexibilities lead to larger seismically induced earth pressures.

Concerning the wall's deflection, as it is expected more flexible walls go under higher deflections. The variation of the d_w from 5 to 50 increased the $\frac{\Delta h}{H}$ from 0.013 to 0.06 for the wall with ($d_\theta = 0$). This ratio changes from 0.034 to 0.116 for the wall with ($d_\theta = 4$).

Wall's base flexibility

The relative flexibility of the wall and the retained soil, d_θ, was varied between 0 (stiff base) to 4 (soft base) once for the rigid wall, $d_w = 5$, and once for the flexible wall, $d_w = 50$. The obtained results are shown in Figures 5.37 to 5.40.

As it can be seen from Figures 5.37, 5.38, and 5.39, the increase of the d_θ results in higher seismic soil pressures and consequently larger seismic resultant forces and moments regardless of the wall's flexibility. This finding is contrary to the results obtained through the 2D single-layer

approach proposed by Veletsos and Younan (1997) and later developed by Psarropoulos et al. (2005) and Jung and Bobet (2008). In the Veletsos and Younan (1997) method the rotational stiffness of the wall's base is simulated through a rotational spring (Figure 5.22) and horizontal and vertical translations of the wall were not allowed; later, Jung and Bobet (2008) in their numerical studies considered for the horizontal and vertical flexibilities of the wall's foundation by adding two more springs to the base of the wall. It is clear that utilizing the springs as a simplifying way for the simulation of the foundation soil layer is not accurate and affects the behavior of the retaining structure. Moreover, using the single-layer approach with the springs does not take into account the energy dissipation provided by the foundation soil layer through material and radial damping.

In this study, the change of d_θ was conducted by changing of the shear modulus of the foundation soil layer. Higher d_θ values mean softer foundation soil layers. Having the same density as the retained soil, increasing of this layer's stiffness (lowering the d_θ) results in lower impedance ratio values, $\alpha_z = \frac{\bar{V}_{s(\text{top layer})}}{V_{s(\text{foundation soil})}}$, and thus, lower stresses are transmitted to the top layer, $\sigma_{\text{transmitted}} = \frac{2\alpha_z}{1+\alpha_z}\,\sigma_{\text{incident}}$, (Kramer, 1996). Therefore, increasing of the stiffness of the foundation layer causes smaller seismic soil pressures on the embedded structure. Based on the obtained results, the flexibility of the structure's base has a significant effect on the seismic soil pressures, as the variation of d_θ from 0 to 4 increases $\frac{\Delta P_E}{k_h \gamma_s H^2}$ and $\frac{\Delta M_E}{k_h \gamma_s H^3}$ for 166.29% and 121.22% for the rigid wall (d_w = 5), respectively. These increase percentages of the $\frac{\Delta P_E}{k_h \gamma_s H^2}$ and $\frac{\Delta M_E}{k_h \gamma_s H^3}$ are 96.28% and 101.27% for the flexible wall (d_w = 50), respectively.

Regarding the wall's relative displacement to its base, relatively bigger deflections are observed for higher values of d_θ, for both flexible and rigid structures which shows the importance

of this layer in the seismic behavior of underground structures. For the rigid wall, the increase of d_θ from 0 to 4, decreased the $\frac{\Delta h}{H}$ from 0.013 to 0.034. This ratio changes from 0.06 to 0.116 for the flexible wall.

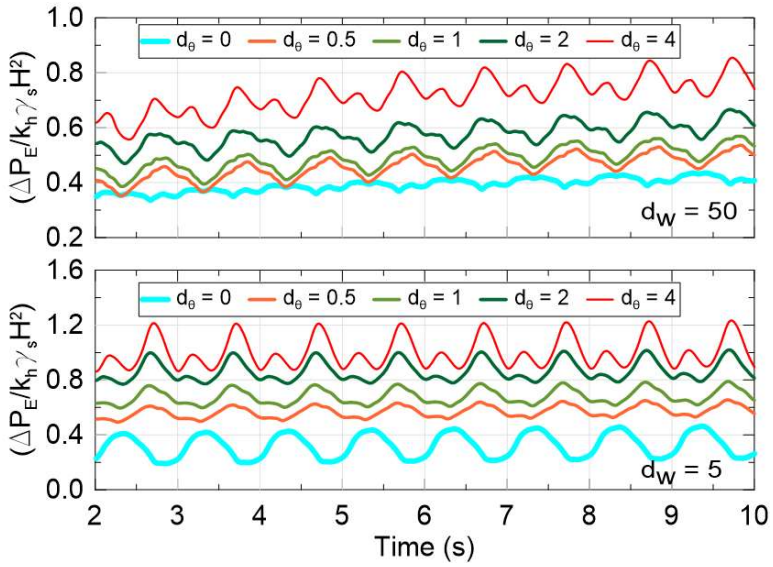

Figure 5.37. Normalized seismic resultant force time history for cases with different wall's base flexibilities

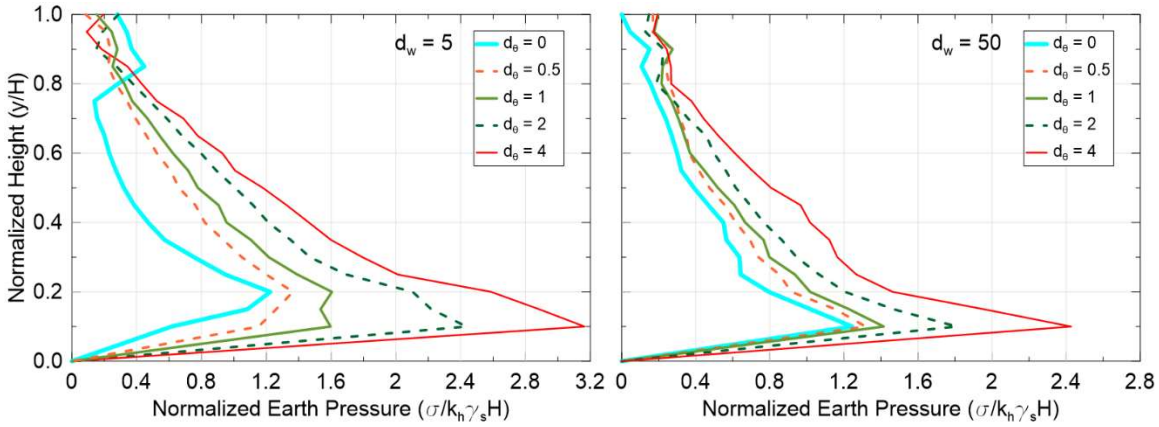

Figure 5.38. Normalized distribution of seismic soil pressures for cases with different wall's base flexibilities

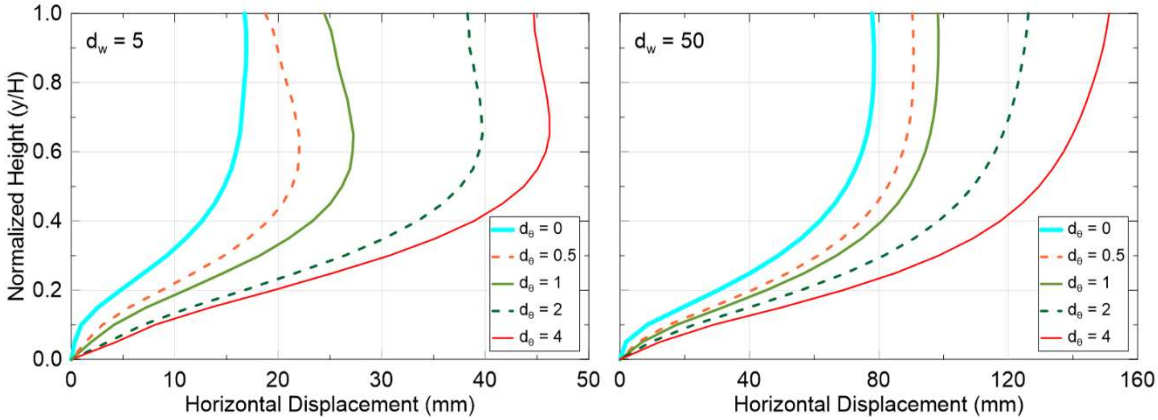

Figure 5.39. Wall and adjacent soil displacements for cases with different wall's base flexibilities

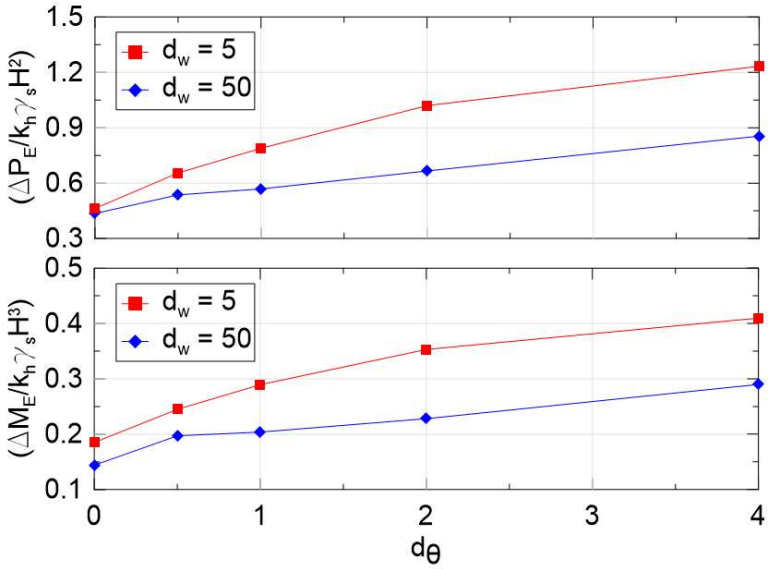

Figure 5.40. Normalized variation of the resultant seismic force and moment against the wall's base flexibility

Wall length/ wall height ratio

All of the previous models were performed for structures with the length to height ratio, $\frac{L}{H}$, of one. In order to investigate the 3D effects of structure's geometry on the seismic soil pressures, two more $\frac{L}{H}$ ratios of 1.5 and 2 were also analyzed for each of the extreme cases of (d_w = 50, d_θ = 4) and (d_w = 5, d_θ = 0). Figure 5.41 shows the distribution of the seismic soil pressures on the wall for the analyzed cases. The variations of the normalized seismic resultant force, $\frac{\Delta P_E}{k_h \gamma_s H^2}$, and

normalized corresponding resultant seismic moment, $\frac{\Delta M_E}{k_h \gamma_s H^3}$, against the $\frac{L}{H}$ ratio for two extreme cases of ($d_w = 50$, $d_\theta = 4$) and ($d_w = 5$, $d_\theta = 0$) are shown in Figure 5.42.

As it can be seen from Figure 5.41, the $\frac{L}{H}$ ratio does not affect the overall shape of the seismic soil pressure profiles for neither of the wall types but increases the magnitude of the seismically induced soil pressures. This is reasonable because by increasing of the $\frac{L}{H}$, the stiffening effect of the side walls, located along the width of the structure, reduces and higher pressures are expected. For the flexible wall on a soft soil, ($d_w = 50$, $d_\theta = 4$), the increase of the $\frac{L}{H}$ ratio from 1 to 2 slightly increases the amount of seismic soil pressures and the amount of $\frac{\Delta P_E}{k_h \gamma_s H^2}$ and $\frac{\Delta M_E}{k_h \gamma_s H^3}$ increase by 12.03% and 24.94%, respectively. This effect is higher for the wall with ($d_w = 5$, $d_\theta = 0$), as the increase of the $\frac{L}{H}$ ratio increases the amount of $\frac{\Delta P_E}{k_h \gamma_s H^2}$ and $\frac{\Delta M_E}{k_h \gamma_s H^3}$ by 65.09% and 46.03%, respectively.

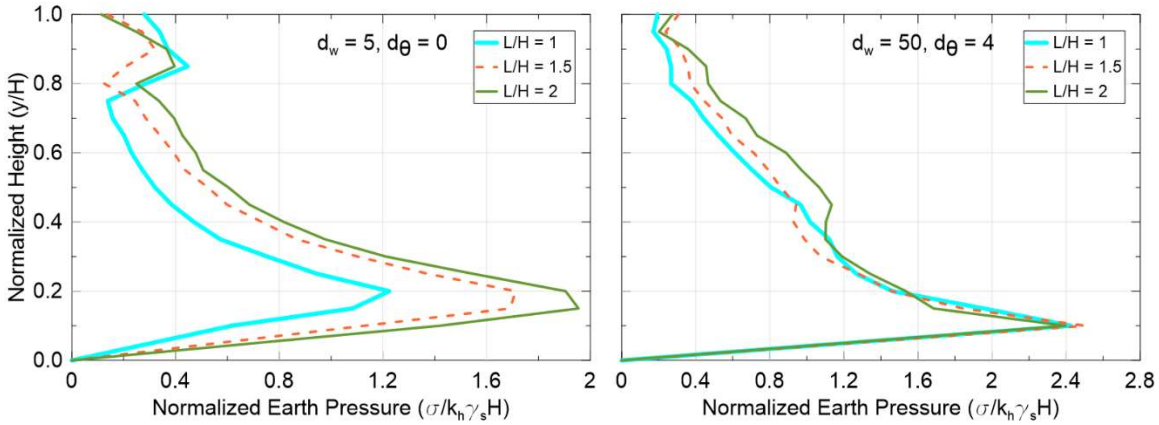

Figure 5.41. Normalized distribution of seismic soil pressures for cases with L/H ratios

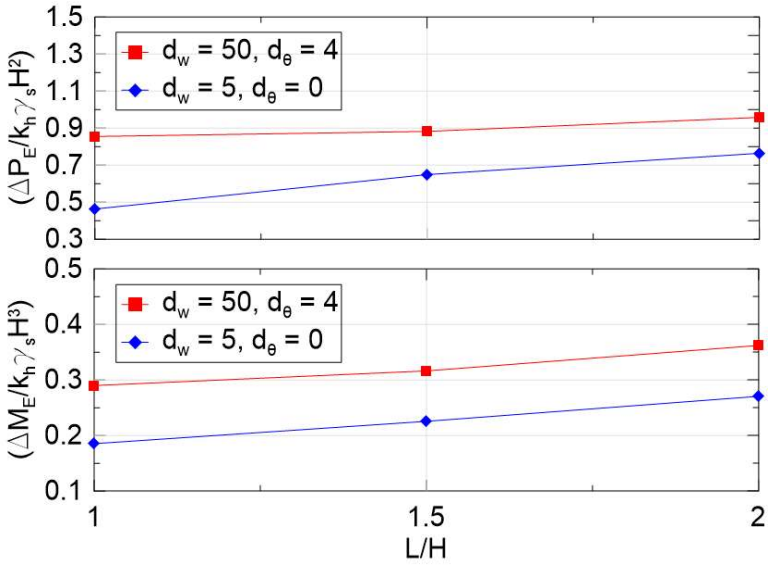

Figure 5.42. Normalized variation of the resultant seismic force and moment against the L/H ratio

Earthquake acceleration amplitude

The initial acceleration amplitude, $k_h = \frac{a_h}{g}$, which was used in the parametric studies was 0.4. In order to perform a more comprehensive study of the problem, the two extreme cases of (d_w = 50, d_θ = 4) and (d_w = 5, d_θ = 0) were analyzed under four other motions with k_h values of 0.2, 0.6, 0.8, and 1. Figure 5.43 presents the variation of $\frac{\Delta P_E}{k_h\gamma_s H^2}$ and $\frac{\Delta M_E}{k_h\gamma_s H^3}$ against the k_h. According to the 2D single-layer methods, the normalized $\frac{\Delta P_E}{k_h\gamma_s H^2}$ and $\frac{\Delta M_E}{k_h\gamma_s H^3}$ are not functions of the acceleration amplitude and for any wall-soil system with certain properties, these normalized values remain constant regardless of the k_h value. Results of the current numerical analyses showed that the $\frac{\Delta P_E}{k_h\gamma_s H^2}$ and $\frac{\Delta M_E}{k_h\gamma_s H^3}$ are not constant and vary with the change of k_h amount. As it can be seen from Figure 5.43, for the flexible wall on a soft soil, (d_w = 50, d_θ = 4), the normalized resultant force increases with the increase of k_h from 0.2 to 0.6 but reduces by further increase of the k_h values. For the rigid wall on a stiff soil, (d_w = 5, d_θ = 0), increase of the $\frac{\Delta P_E}{k_h\gamma_s H^2}$ continues up to k_h of 0.8 and slightly decreases for k_h of 1. It is worth mentioning that for both of the studied

wall-soil systems, the normalized seismic force approaches almost the same value for higher acceleration levels. The trend of $\frac{\Delta M_E}{k_h \gamma_s H^3}$ variation with respect to k_h values, is the same as the $\frac{\Delta P_E}{k_h \gamma_s H^2}$, for the flexible wall on a soft soil, (d_w = 50, d_θ = 4). For the rigid wall on a stiff soil, (d_w = 5, d_θ = 0), the normalized seismic moment is almost constant and its changes are negligible.

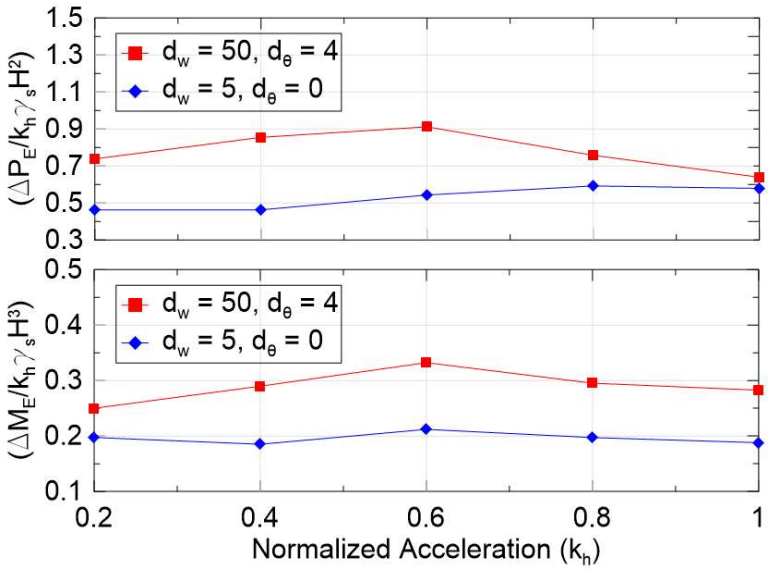

Figure 5.43. Normalized variation of the resultant seismic force and moment against the earthquake acceleration amplitude

5.3. Summary and conclusions

In this chapter of the dissertation, the seismic response of deep underground structures was evaluated through finite element modeling. First, results of the E-Defense tests under 50% and 80% scaled Kobe motions were used to validate the utilized numerical approach. Preserving the configuration of the modeled tests, a limited set of parametric studies was executed by changing the properties of the structures and soil material including the flexibility of the structure, cohesion and friction angle of the soil. It was concluded that in addition to soil mechanical properties, structure's flexibility plays an important role in the seismic behavior of deep underground

structures, and stiffer walls undergo more seismic soil pressures. A simplified 3D soil-structure model was then built and effects of the most important parameters which are believed to control the seismic response of deep underground structures were examined. These parameters included cohesion and friction angle of the adjacent soil, flexibility of the structure's wall and base (i.e., stiffness of the foundation soil stiffness), geometry of the structure, and the amplitude of the seismic motion. Summary of the parametric studies results in terms of normalized resultant seismic forces, $\frac{\Delta P_E}{k_h \gamma_s H^2}$, and their corresponding moments, $\frac{\Delta M_E}{k_h \gamma_s H^3}$, is presented in Table 5.11.

Moreover, to have a more complete set of data, two extreme cases of a flexible wall on a soft soil foundation ($d_w = 50$, $d_\theta = 4$) and a rigid wall on a stiff base ($d_w = 5$, $d_\theta = 0$) were also analyzed through a single-layer 2D plane-strain approach developed based on the Veletsos and Younan (1997) analytical solution and its more general numerical form by Psarropoulos et al. (2005). For the wall with ($d_w = 50$, $d_\theta = 4$), $\frac{\Delta P_E}{k_h \gamma_s H^2}$ and $\frac{\Delta M_E}{k_h \gamma_s H^3}$, were calculated to be 0.26 and 0.10, respectively. $\frac{\Delta P_E}{k_h \gamma_s H^2}$, and the $\frac{\Delta M_E}{k_h \gamma_s H^3}$ were 0.69 and 0.31 for the wall with ($d_w = 5$, $d_\theta = 0$), respectively. Following concluding remarks were obtained from the numerical results:

1) Improvement of the retained soil's strength parameters (i.e., cohesion, and friction angle) reduces the seismically induced soil pressures and wall's deflection regardless of the wall/base flexibility. Comparing to the friction angle, the cohesion has a more significant influence on the wall's seismic behavior and should not be neglected in the seismic analysis of earth retaining and underground structures.
2) Effect of the Wall's relative flexibility to the adjacent soil is dependent on the rigidity of the wall's base. Although the overall finding is that seismic soil pressures decrease with the increase of the wall's flexibility, it was shown that for structures located on a stiff

foundation soil layer, variation of the wall's flexibility does not affect the exerted seismic force considerably. On the other hand, for these walls the increase of the flexibility up a certain amount results in relatively lower seismic moments which is due to the movement of the maximum seismic soil pressure along the wall toward its base; after this point, the magnitude of the resultant seismic moment remains almost constant. Influence of the wall's flexibility is more recognizable for the walls which are located on soft soil foundations, and the increase of this parameter results in lower seismic soil pressures. Concerning the wall's deflection, as it is expected more flexible walls go under higher deflections.

3) The foundation soil's stiffness has a significant effect on the seismic pressures, and structures on stiffer soil materials experience less seismic soil pressures. The increase of the foundation soil's stiffness reduces the impedance ratio value between the retained soil medium and the foundation soil and consequently reduces the amplitude of the stresses transmitted to the retained material.

4) Increase of he length/height ratio of the structure, $\frac{L}{H}$, lowers the stiffening effect of the side walls, located along the width of the structure, and thus lower seismic pressures are observed for smaller $\frac{L}{H}$ values. This effect becomes more pronounced with the increase of wall's stiffness.

5) Contrary to what is suggested by single layer 2D approaches, the normalized resultant seismic force and its corresponding moment vary with the change of the acceleration amplitude, $k_h = \frac{a_h}{g}$. For both of the extreme cases analyzed, it was shown that the normalized seismic force increases with the increase of the acceleration amplitude up to a specific value; with the increase of the motion's acceleration to high levels, the normalized force approaches almost the same amount for both cases. Variation of the normalized

resultant seismic moment is the same as the normalized force, for the flexible wall on a soft soil; for the rigid wall on a stiff soil, the normalized seismic moment is almost constant, and its changes are negligible.

Table 5.11. Summary of the parametric studies

Changing Parameter	Varied Values	$d_w = 50$, $d_\theta = 4$		$d_w = 5$, $d_\theta = 0$	
		$(\Delta P_E)/(k_h \gamma_s H^2)$	$(\Delta M_E)/(k_h \gamma_s H^3)$	$(\Delta P_E)/(k_h \gamma_s H^2)$	$(\Delta M_E)/(k_h \gamma_s H^3)$
$c/\gamma_s H$	0	0.936	0.333	0.566	0.221
	0.05	0.855	0.290	0.463	0.185
	0.1	0.692	0.203	0.332	0.111
	0.2	0.479	0.110	0.171	0.038
	0.3	0.343	0.069	0.108	0.021
$\varphi°$	20	1.158	0.441	0.706	0.283
	30	0.995	0.349	0.510	0.204
	35	0.855	0.290	0.463	0.185
	40	0.775	0.265	0.426	0.172
	45	0.705	0.232	0.405	0.165
k_h	0.2	0.739	0.250	0.463	0.198
	0.4	0.855	0.290	0.463	0.185
	0.6	0.912	0.332	0.544	0.212
	0.8	0.758	0.295	0.592	0.197
	1	0.639	0.283	0.579	0.188
L/H	1	0.855	0.290	0.463	0.185
	1.5	0.883	0.316	0.649	0.226
	2	0.958	0.362	0.764	0.270
Changing Parameter	Varied Values	$d_\theta = 0$		$d_\theta = 4$	
		$(\Delta P_E)/(k_h \gamma_s H^2)$	$(\Delta M_E)/(k_h \gamma_s H^3)$	$(\Delta P_E)/(k_h \gamma_s H^2)$	$(\Delta M_E)/(k_h \gamma_s H^3)$
d_w	5	0.463	0.185	1.233	0.410
	10	0.441	0.140	1.047	0.357
	25	0.444	0.138	0.921	0.311
	40	0.454	0.146	0.893	0.305
	50	0.446	0.145	0.855	0.290
Changing Parameter	Varied Values	$d_w = 5$		$d_w = 50$	
		$(\Delta P_E)/(k_h \gamma_s H^2)$	$(\Delta M_E)/(k_h \gamma_s H^3)$	$(\Delta P_E)/(k_h \gamma_s H^2)$	$(\Delta M_E)/(k_h \gamma_s H^3)$
d_w	5	0.463	0.185	0.436	0.144
	10	0.655	0.245	0.537	0.197
	25	0.789	0.290	0.569	0.204
	40	1.020	0.353	0.666	0.228
	50	1.233	0.410	0.855	0.290

Chapter 6

Summary and conclusions

6.1. Summary and conclusions

The distribution and magnitude of seismically induced soil pressures on deep underground structures were studied through experimental, analytical, and numerical analyses. The results of a series of large-scale shake table tests executed at the E-Defense facility in Miki, Japan, were used as experimental reference for this study. In these tests, a densely instrumented system of large-scale underground structures consisting of two vertical shafts connected through a cut-and-cover tunnel and two independent shield tunnels was subjected to step-sine sweeps and scaled ground motion records (i.e., 50%, and 80%) of the Kobe (1995) earthquake. The surrounding soil strata consisted of cemented sand at the bottom of the structure, and a thick medium dense silica sand layer at the top. The soil-structure system was heavily instrumented with different types of sensors, including strain gauges, accelerometers, displacement transducers, bender elements, and pressure sensors. A new, large-area contact soil pressure sensor, developed by our research group, was also part of this instrumentation. A number of these pressure sensors were mounted on one of the vertical shafts, and their recordings were used to assess seismic soil pressures on underground structures during various earthquake motions. A detailed review of this newly developed pressure sensor, including its design, static and dynamic calibration procedures, its advantages compared to currently used contact pressure instrumentation in geotechnical applications (e.g., soil pressure cells, and tactile sensors) was presented in chapter 3 of this dissertation.

After a detailed review of the large-scale tests, seismic soil pressure records were compared with different limit-state and elastic-based analytical methods for retaining walls found in literature and weaknesses of each approach were investigated.

The elastic-based methods, originally designed for non-yielding rigid walls, consider the soil material as a visco-elastic medium and cannot capture the cyclic behavior of the soil, nor its failure. Moreover, the flexibility of deep underground structures which plays an important role in the distribution and magnitude of seismic soil pressures is usually ignored in these methods. Analysis of the experimental results showed that among the elastic-based methods, only Veletsos and Younan (1997) account for the structural flexibility, and could capture the trend and magnitude of seismic soil pressures observed in the experimental results.

The limit-state methods, primarily used for non-yielding walls, with either kinematic or stress solutions, treat the soil as a homogeneous perfectly plastic material. The limit-state methods under-predicted the measured seismic pressures for the 50% Kobe motion with a PBA of 0.38g. Results for the 80% Kobe motion (PBA 0.69g) showed a strong over-prediction of seismic soil pressures for all limit-state methods. Moreover, limit-state methods use the pseudo-static approach and ignore the frequency characteristics of the applied motion which has a significant influence on the distribution and magnitude of seismic soil pressures. Therefore, they could not capture the experimental location of the resultant force. It was concluded that none of the analytical methods take into account the important factors affecting the seismic behavior of deep underground structures (e.g., 3D effects, soil elastic-plastic behavior, and structure's flexibility) and therefore, can only serve as a rough preliminary estimate and should not be employed in performance-based geotechnical analyses.

The shake-table experiments results were then used to develop and calibrate three-dimensional finite element, FE, ABAQUS models. The purpose of the numerical analyses was to evaluate the effects of different mechanical and geometrical parameters on the seismic behavior of deep underground structures and to derive simple graphical solutions for predicting seismically induced soil pressures on this type of structure. The FE models were first calibrated against the large-scale shake table tests with scaled ground motion records (i.e., 50%, and 80%) of the Kobe (1995) earthquake. The results of numerical analyses were compared with the experimental data concerning induced seismic soil pressures and acceleration response of the soil material at different depths. A good agreement was observed between the computed results and experimental data which showed the reliability of the utilized FE method in the modeling of the problem. Preserving the configuration of the modeled tests, a limited set of parametric studies was executed by changing the properties of the structures and soil material including the flexibility of the structure, cohesion and friction angle of the soil. It was concluded that in addition to the soil's constitutive properties, the structure's flexibility plays an important role in the seismic behavior of deep underground structures, and stiffer walls undergo more seismic soil pressures.

In the final section of this research, a simplified three-dimensional soil-structure finite element model was developed and utilized in a set of parametric studies to investigate the effects of different parameters on the distribution and magnitude of seismic soil pressures. The studied parameters included cohesion and friction angle of the adjacent soil, flexibility of the structure's wall and base (i.e., stiffness of the foundation soil stiffness), geometry of the structure, and the amplitude of the seismic motion. In these models, the retained soil was treated as a nonhomogeneous viscoelastic-plastic material using the Mohr-Coulomb failure criteria, and the base excitation was introduced by a prescribed sinusoidal motion. For comparison purposes, a 2D

plane-strain FE model was also made based on the on the finite element method by Psarropoulos et al. (2005), a more general form of the analytical solution by Veletsos and Younan (1997), and analyzed. Parametric studies were performed for two extreme cases of a flexible wall on a soft soil foundation and a rigid wall on a stiff base. The following are the main conclusions obtained from the numerical results:

The distribution and magnitude of seismic soil pressures are significantly affected by the retained soil strength parameters and (i.e., cohesion, and friction angle), and the increase of these parameters reduces the seismically induced soil pressures and wall's deflection regardless of the wall/base flexibility. Comparing to the friction angle, the cohesion has more influence on the wall's seismic behavior and should not be neglected in the seismic analysis of earth retaining and underground structures.

Effect of the Wall's relative flexibility to the adjacent soil is dependent on the rigidity of the wall's base. Although the overall finding is that seismic soil pressures decrease with the increase of the wall's flexibility, it was shown that for structures located on a stiff foundation soil layer, variation of the wall's flexibility does not affect the exerted seismic force considerably. On the other hand, for these walls the increase of the flexibility up a certain amount results in relatively lower seismic moments which is due to the movement of the maximum seismic soil pressure along the wall toward its base; after this point, the magnitude of the resultant seismic moment remains almost constant. Influence of the wall's flexibility is more recognizable for the walls which are located on soft soil foundations, and the increase of this parameter results in lower seismic soil pressures. Concerning the wall's deflection, as it is expected more flexible walls go under higher deflections.

The foundation soil's stiffness has a significant effect on the seismic pressures, and structures on stiffer soil materials experience less seismic soil pressures. The increase of the foundation soil's stiffness reduces the impedance ratio value between the retained soil medium and the foundation soil and consequently reduces the amplitude of the stresses transmitted to the retained material.

Increase of he length/height ratio of the structure, $\frac{L}{H}$, lowers the stiffening effect of the side walls, located along the width of the structure, and thus lower seismic pressures are observed for smaller $\frac{L}{H}$ values. This effect becomes more pronounced with the increase of wall's stiffness.

Contrary to what was suggested by single layer 2D approaches (e.g., Veletsos and Younan 1997, Psarropoulos et al. 2005, Jung and Bobet 2008), the normalized resultant seismic force and its corresponding moment vary with the change of the acceleration amplitude, $k_h = \frac{a_h}{g}$. For both of the extreme cases analyzed herein, it was shown that the normalized seismic force increases with the increase of the acceleration amplitude up to a specific value; with the increase of the motion's acceleration to high levels, the normalized force approaches almost the same amount for both cases. Variation of the normalized resultant seismic moment is the same as the normalized force, for the flexible wall on a soft soil; for the rigid wall on a stiff soil, the normalized seismic moment is almost constant, and its changes are negligible.

The variations of the seismic soil pressures resultant force and its corresponding moment were plotted as normalized graphs against each of the studied parameters. These graphs could be used in the seismic analysis and design of deep embedded structures.

Chapter 7

References

7.1. References

ABAQUS 6.13 [Computer software]. Dassault Systèmes SIMULIA Corporation, Minneapolis.

Ahmed M. R. and Meguid, M. A. (2009). "Patents and techniques of contact pressure measurement in geotechnical engineering." *Recent Patents on Eng.*, Vol. 3, No. 3, 210-219.

Asakura, T., Shiba, Y., Matsuoka, S., Oya, T., and Yashiro, K. (2000). "Damage to mountain tunnels by earthquake and its mechanism." *Doboku Gakkai Ronbunshu*, 2000, 27–38.

Askegaard, V. (1963). "Measurement of pressure in solids by means of pressure cells." *Bulletin No. 17*, Structural Research Laboratory, Technical University of Denmark, Copenhagen.

Alampalli, S. and Elgamal A. (1990). "Dynamic response of retaining walls including supported soil backfill: A Computational Model." *4th U.S. National Conference on Earthquake Engineering*, Palm Springs, CA, Vol. 3, 623-632.

Al-Atik, L., and Sitar, N. (2010). "Seismic earth pressures on cantilever retaining structures." *Journal of Geotechnical and Geoenvironmental Engineering*, 136(10), 1324-1333.

Al-Homoud, A. S., and Whitman, R. V. (1999). "Seismic analysis and design of rigid bridge abutments considering rotation and sliding incorporating non-linear soil behavior." *Soil Dynamics and Earthquake Engineering*, 18(4), 247-277.

Bhatia, S. K. and Blaney, G. W. (1991). "Recent advances in instrumentation, data acquisition and testing in soil dynamics." *ASCE Proc. of Sessions Sponsored by the Geotech. Eng. Division*, Orlando, Florida.

Bolt, B. A. (1969). "Duration of strong motion." *Proceedings of the 4th World Conference on Earthquake Eng.*, Santiago, Chile, 1304-1315.

Bolton, M. D., and Steedman, R. S. (1982). "Centrifugal testing of microconcrete retaining walls subjected to base shaking." *Proceedings, Conference on Soil Dynamics and Earthquake Engineering*, Southhampton.

Bolton, M. D., and Steedman, R. S. (1985). "The behavior of fixed cantilever walls subject to lateral loading." *Application of Centrifuge Modeling to Geotechnical Design*, Craig Ed., Balkema, Rotterdam.

Brandenberg, S. J., Mylonakis, G., and Stewart, J. P. (2015). "Kinematic framework for evaluating seismic earth pressures on retaining structures." *Journal of Geotechnical & Geoenvironmental Engineering*, 141, No. 7.

Brandenberg, S. J., Mylonakis, G., and Stewart, J. P. (2017) "Approximate solution for seismic earth pressures on rigid walls retaining inhomogeneous elastic soil." *Soil Dynamics and Earthquake Engineering,* Vol. 97, 468-477.

Building Seismic Safety Council. (2010). "NEHRP recommended provisions for seismic regulations for new buildings and other structures." *(FEMA 750)*, 2009 Edition, Part 1 – Provisions. BSSC, Washington, DC.

Büscher, G.H., Kõiva, R., Schürmann, C., Haschke, R., and Ritter, H.J. (2015). "Flexible and stretchable fabric-based tactile sensor." *Robotics and Autonomous Systems*, Vol. 63, Part 3, Pages 244-252. https://doi.org/10.1016/j.robot.2014.09.007

Chen, J., Jiang, L., Li, J., and Shi, X. (2012). "Numerical simulation of shaking table test on utility

tunnel under non-uniform earthquake excitation." *Tunnelling and Underground Space Technology*, Vol. 30, 205-216.
Cilingir, U., and Madabhushi, S. P. G. (2011). "Effect of depth on the seismic response of square tunnels." *Soils & Foundations*, 51, 449–457.
Clough, G. W. and Fragaszy, R. F. (1977). "A study of earth loadings on floodway retaining structures in the 1971 San Fernando valley earthquake." *Proc. of the 6th World Conf. on Earthquake Eng.*, 3, 2455-2460.
Correia, R., Li, J., Staines, S., Chehura, E., James, S. W., Kutner, J., Dewhurst, P., Ferreira, P., and Tatam, R. P. (2009). "Fibre bragg grating based effective soil pressure sensor for geotechnical applications." *20th International Conf. on Optical Fibre Sensors*, Edinburgh, United Kingdom, SPIE, Bellingham, WA.
Coulomb, CA. (1776). "Essai sur une application des regies des maximis et minimis a quelques problemes de statique relatifs a 1'architecture." *Memoires de I'Academie Royale pres Divers Savants*, Vol. 7, 1776.
Coyle, H. M. and Bartoskewitz, R. E. (1976). "Earth pressure on precast panel retaining wall." *ASCE Journal of Geotech. Eng. Division*, Vol. 102, No. GT5, 441-456.
Dewoolkar, M. M., Ko, H., and Pak, R. Y. S. (2001). "Seismic behavior of cantilever retaining walls with liquefiable backfills." *Journal of Geotechnical and Geoenvironmental Engineering*, 127(5), 424-435.
DiBiagio, E. (1977). "Field instrumentation- a geotechnical tool." *Norwegian Geotech. Institute*, Pub. No. 115, 29-40.
Doebelin, E. O. (1990). "Measurement systems: application and design." 4th Ed., McGraw-Hill, New York, NY, 992p.
Dunnincliff, J. (1988). "Geotechnical instrumentation for monitoring field performance." John Wiley and Sons, New York, New York, 577p.
Durante, M.G., Brandenberg, S. J., Stewart, J.P., and Mylonakis, G. (2018) "Winkler stiffness intensity for flexible walls retaining inhomogeneous soil." *5th Geotechnical Earthquake Engineering and Soil Dynamics Conference (GEESD 2018)*, Austin, Texas.
Fatahi, B., Basack, S., Ryan, P., Zhou, W. H., and Khabbaz, H. (2014). "Performance of laterally loaded piles considering soil and interface parameters." *Geomechanics and Engineering*, 7(5), 495-524.
Felio, G. Y. and Bauer, G. E. (1986). "Factors affecting the performance of a pneumatic earth pressure cell." *ASTM Geotech. Testing Journal*, Vol. 9, No. 2, 102-106.
Fox, P. J., Sander, A. C., Elgamal, A., Greco, P., Isaacs, D., Stone, M., and Wong, S. (2014). "Large soil confinement box for seismic performance testing of geo-structures." *Geotechnical Testing Journal*, 38, 72–84.
Geraili Mikola, R. G., Sitar, N. (2013). "Seismic earth pressures on retaining structures in cohesionless soils." *California Department of Transportation (Caltrans)*, Report No. UCB GT 13-01.
Ghosh, S., Dey, G. N., and Datta, B. (2008). "Pseudo-static analysis of rigid retaining wall for dynamic active earth pressure." *12th International Conf. of International Association for Computer Methods and Advances in Geomechanics*, Goa, India, 2008, 4122 – 4131.
Ghosh, S. and Saran, S. (2007). "Pseudo-static analysis of rigid retaining wall for dynamic active earth pressure." *International Conf. on Civil Eng. In the New Millennium: Opportunity and Challenges (CENeM-2007),* Bengal Eng. And Science University, Shibpur, West Bengal.
Gillis, K. M., Dashti, S., Hashash, Y. M. A., and Romero Arduz, M. I. (2014). "Seismic response

of a cut-and-cover underground structure in dry sand: centrifuge modelling." *Physical Modelling in Geotechnics (Gaudin and White, Editors)*, Taylor and Francis Group, London.
Gillis, K., Dashti, S., and Hashash, Y. (2015). "Dynamic calibration of tactile sensors for measurement of soil pressures in centrifuge." *ASTM Geotech. Testing Journal*, Vol. 38, No. 3, 261-274.
Guzman, J., and Ryan, K. (2015). "Data from the network for earthquake engineering simulation/ E-Defense collaborative test program on innovative isolation systems and non-structural components." *Earthquake Spectra*, 31, 1195–1209.
Ha, D., Abdoun, T. H., O'Rourke, M. J., Symans, M. D., O'Rourke, T. D., Palmer, M. C., and Stewart, H. E. (2008). "Centrifuge modeling of earthquake effects on buried high-density polyethylene (HDPE) pipelines crossing fault zones." *ASCE Journal of Geotech. and Geoenviron. Eng.*, Vol. 134, No. 10, 1501–1515.
Hardin, B. O., and Drnevich, V. P., (1972). "Shear modulus and damping in soils: design equations and curves." *Journal of Soil Mechanics and Foundations Division*, SM7, 667-692.
Hardin B. O., and Richart, F. E. J., (1963). "Elastic wave velocities in granular soils." *Journal of Soil Mechanics and Foundations Division*, 89, 33-65.
Helm, J. and Suleiman, M. (2012). "Measuring soil-structure interaction on laterally loaded piles with digital image correlation." *Procedia IUTAM*, Vol. 4, 2012, 66-72.
Hokmabadi, A. S., Fatahi, B., and Samali, B. (2014). "Assessment of soil-pile-structure interaction influencing seismic response of mid-rise buildings sitting on floating pile foundations." *Computers and Geotechnics*, Vo. 55, 172-186.
Huntington, W. C. (1957). "Earth pressures and retaining walls." John Wiley and Sons, New York, NY.
Hushmand, A., Dashti, S., Zhang, M., McCartney, J. S., Ghayoomi, J., Hushmand, M., Mokarram, B., Davis, N., Davis, C., Lee, Y., and Hu, J. (2014). "Seismic soil-structure interaction and lateral earth pressures on buried reservoir structures." *Geo-Congress 2014 Technical Papers*, 1215–1224.
Hushmand, A., Dashti, S., Davis, C., Hushmand, B., Zhang, M., Ghayoomi, M., McCartney, J. S., Lee, Y., and Hu, J. (2016). "Seismic performance of underground reservoir structures: insight from centrifuge modelling on the influence of structure stiffness." *Journal of Geotechnical and Geoenvironmental Engineering*, 142, No. 7.
Hvorslev, M. J. (1976). "The changeable interaction between soils and pressure cells: tests and reviews at the waterway experiment station." *Technical Report*, No. 5-76-5, U.S. Army Corps of Eng., Waterway Experiment Station, Vicksburg, MS, 278p.
Ishibashi, I., and Fang, Y. S. (1987). "Dynamic earth pressures with different wall movement modes." *Soils and Foundations*, 27(4), 11-22.
Ishii, Y., Arai, H., and Tsuchida, H. (1960). "Material earth pressure in an earthquake." *Proceedings, 2nd Conference on Earthquake Engineering*, Tokyo, Japan.
Iskander, M., Zhibo, C., Omidvar, M., Guzman, I., and Elsherif, O. (2013). "Active static and seismic earth pressure for c-φ soils." *Soils and Foundations*, 53(5), 639-652.
Iwatate, T., Kobayashi, Y., Kusu, H., and Rin, K. (2000). "Investigation and shaking table tests of subway structures of the Hyogoken-Naby earthquake." *Proceedings of the 12th World Conference on Earthquake Engineering*, Auckland, New Zealand.
Jacobsen, L. S. (1939). Described in Appendix D of "The Kentucky project." *Technical Report No. 13*, Tennessee Valley Authority, 1951.
Janoyan, K. D. and Whelan, M. J. (2004). "Interface stresses between soil and large diameter

drilled shaft under lateral loading." *ASCE GeoSupport Conf.*, Orlando, FL.
Jennings, J. E. and Burland, J. B. (1960). "Rand soil-pressure cell for low pressures, high accuracy and long-term stability." *Journal of Scientific Instruments*, Vol. 37, 193–195.
Jung, C. and Bobet, A. (2008). "Seismic earth pressures behind retaining walls: effects of rigid body motions," Zeng, D., Manzari, M., and Hiltunen, D., Eds., Proceedings, *Geotechnical Earthquake Engineering and Soil Dynamics IV*, ASCE, Sacramento, CA.
Kapila, I. P. (1962). "Earthquake resistant design of retaining walls." *Second Earthquake Symposium*, University of Roorkee, India, 97-108.
Kawamata, Y., Nakayama, M., Towhata, I., Yasuda, S., and Tabata, K. (2012). "Large-scale experiment using E-Defense on dynamic behaviors of underground structures during strong ground motions in urban areas." *15th World Conference of Earthquake Engineering*, Lisbon.
Kawamata, Y., Nakayama, M., Towhata, I., and Yasuda, S. (2016). "Dynamic behavior of underground structures in E-Defense shaking experiments." *Soil Dynamics and Earthquake Engineering*, 82, 24–39.
Keykhosropour, L., and Lemnitzer, A. (2019). "Experimental studies of seismic soil pressures on vertical flexible, underground structures and analytical comparisons." *Soil Dynamics and Earthquake Engineering*, Vol. 118, 166-178.
Keykhosropour, L., Lemnitzer, A., Star, L., Marinucci, A., Keowen, S. (2019). "Closure to discussion of implementation of soil pressure sensors in large-scale soil structure interaction studies." *ASTM Geotechnical Testing Journal*, Vol. 42, No. 5.
Keykhosropour, L., Lemnitzer, A., Star, L., Marinucci, A., Keowen, S. (2018). "Implementation of soil pressure sensors in large-scale soil structure interaction studies." *ASTM Geotechnical Testing Journal*, Vol. 41, No. 4, 730-746.
Kim, Y., Jeong, S., and Lee, S. (2011). "Wedge failure analysis of soil resistance on laterally loaded piles in clay." *Journal of Geotechnical and Geoenvironmental Engineering*, Vol. 137(7), July.
Klapperich, H. (1983). "Untersuchungen zwn dynamischen erddruck." *Varoeff des Grundbau Institutes*, TU Berlin, Heft 14.
Kogler, F. and Scheidig, A. (1927). "Druck veiteilung im Baugrunde." *Die Bautechnik*, No. 31, July 15.
Kramer, S. L. (1996). "Geotechnical earthquake engineering." Prentice-Hall, Upper Saddle River, New Jersey, NJ.
Kuhlemeyer, R. L., and Lysmer, J. (1973). "Finite element method accuracy for wave propagation problems." *Journal of Soil Mechanics and Foundations Division*, ASCE, 99(SM5), 421-427.
Kurata, S., Arai, H., and Yokoi, T. (1965). "On the earthquake resistance of anchored sheet pile bulkheads." *Proceedings, 3rd World Conference on Earthquake Engineering*, New Zealand.
Lambe, T. W., and Whitman, R. V. (1979). "Soil mechanics." SI Version, John Wiley and Sons, New York, NY.
Lazebnik, G. E. and Tsinker, G. P. (1997). "Monitoring of soil-structure interaction: instruments for measuring soil pressures." Chapman and Hall, New York, NY, 224p.
Legge, T. F. H., Swart, P. L., Zyl, G. V., and Chtcherbakov, A. A. (2006). "A fibre bragg grating stress cell for geotechnical engineering applications." *Measurement Science and Technology*, Vol. 17, 1173-1179.
Lemnitzer, A., Hilson, C., Taciroglu, E., Wallace, J. W., and Stewart, J. P. (2012). "Effect of backfill relative density on lateral response of a bridge abutment wall." 1*5th World Conference on Earthquake Engineering, Lisbon*, Portugal.

Lemnitzer, A., Keykhosropour, L., Kawamata, Y., and Towhata, I. (2016). "E-Defense shake table experiments." *Network for Earthquake Engineering Simulation (publisher)*, Data Set, doi: 10.17603/DS21C78.

Lemnitzer, A., Keykhosropour, L., Kawamata, Y., and Towhata, I. (2017). "Dynamic response of underground structures in sand: experimental data." *Earthquake Spectra*, Vol. 33, No. 1, 347-372.

Lemnitzer, A., and Luu, A. (2013). "Development of soil pressures under lateral loading." *10th International Conference on Urban Earthquake Engineering*, Tokyo Institute of Technology, Tokyo, Japan.

Lin, H., Ni, L., Suleiman, M. T., and Raich, A. (2015). "Interaction between laterally loaded pile and surrounding soil." *Journal of Geotech. and Geoenviron. Eng.*, Vol. 141, No. 4.

Loh, Y. C. (1954). "Internal stress gauges for cementitious materials." *Proceedings of the Society for Experimental Stress Analysis*, 21(2), 13-28.

Luo, C., Yang, X., Zhan, C., Jin, X., and Ding, Z. (2016). "Nonlinear 3D finite element analysis of soil-pile-structure interaction system subjected to horizontal earthquake excitation." *Soil Dynamics and Earthquake Engineering,* 84, 145-156.

Luzhen, J., Jun, C., and Jie, L. (2010). "Seismic response of underground utility tunnels: shaking table testing and FEM analysis." *Earthquake Eng. and Eng. Vibration*, Vol. 9, No. 4, 555-567.

Lysmer, J., and Kuhlemeyer, R. L. (1969). "Finite dynamic model for infinite media." *Journal of the Engineering Mechanics Division*, ASCE, 95(4), 859-877.

Lysmer, J., Udaka, T., Tsai, C. F., and Seed, H. B. (1975). "FLUSH: a computer program for approximate 3-D analysis of soil-structure interaction problems." *Report EERC 75-30*, Earthquake Engineering Research Center, University of California, Berkeley.

Maalej, Y., Dormieux, L., Canou, J., and Dupla, J. C. (2007). "Strength of a granular medium reinforced by cement grouting." *C. R. Mecanique*, 335, 87-92.

Mason, H. G. (1965). "Effects of Structural Compressibility on Active and Passive Arching in Soil-Structure Interaction." *DASA 1718*, Defense Atomic Support Agency, URS 645-8.

Matlock, H. and Reese, L. C. (1963). "Generalized solution for laterally loaded piles." *Journal of Soil Mechanics and Foundations Division*, ASCE, Vol. 86, No. SM5, Part I, 63-91.

Matsui, J., Ohtomo, K., and Kawai, I. (2001). "Research on streamlining seismic safety evaluation of underground reinforced concrete duct-type station – part 3 – analytical simulation by RC macro-model and simple soil model." *Transactions*, SMiRT 16, Paper No. 1296, Washington DC, August.

Matsuo, H. (1941). "Experimental study on the distribution of earth pressure acting on a vertical wall during earthquakes." *Journal of the Japanese Society of Civil Engineers*, Vol. 27, No. 2.

Matsuo, M., and Ohara, S. (1960). "Lateral earth pressures and stability of quay walls during earthquakes." *Proceedings, 2nd world conference on Earthquake Engineering*, Tokyo, Japan.

Mayne, P.W., (2007). "In-situ test calibrations for evaluating soil parameters." *Characterization & Engineering Properties of Natural Soils*, Vol. 3, Taylor & Francis Group, London: 1602-1652.

Meyerhof, G. G. (1963) "Some recent research on the bearing capacity of foundations." *Canadian Geotechnical Journal*, Vol. 1, No. 1, 16-26.

Misawa, T., Kameda, S., Unjo, S., Hosikuma, J., Nagaya, K., and Suzuki, T. (1998). "Shake table test on seismic isolation at tunnel-shaft joint." *Proceedings of the 53th JSCE Annual Conference*.

Monfore, G. E. (1950). "An analysis of the stress distribution in and near stress gauges embedded in elastic soils." *Structural Laboratory Report No. SP 26*, U.S. Bureau of Reclamation, Denver, CO.

Mononobe, N., and Matsuo, M. (1929). "On the determination of earth pressures during earthquakes." *Proceedings of World Engineering Congress*, Vol. 9, 179-187.

Moss, R.E.S., and Crosariol, V. (2013). "Scale model shake table testing of an underground tunnel cross section in soft clay." *Earthquake Spectra*, Vol. 29, No. 4, pp. 1413-1440.

Murphy, V. A. (1960). "The effect of ground characteristics on the seismic design of structures." Proceedings, *2nd World Conference on Earthquake Engineering*, Tokyo, Japan.

Mylonakis, G., Kloukinas, P., Papantonopoulos, C. (2007). "Alternative to the Mononobe–Okabe equations for seismic earth pressures." *Soil Dynamics and Earthquake Engineering*, Vol. 27, 957–969.

Nagae, T., Ghannoum, W. M., Kwon, J., Tahara, K., Fukuyama, K., Matsumori, T., Shiohara, H., Kabeyasawa, Kono, S., Nishiyama, M., Sause, R., Wallace, J. W., and Moehle, J. P. (2015). "Design implications of large-scale shake-table test on four-story reinforced concrete building." *ACI Structural Journal*, 112, 135–146.

Nakamura, Y., Uehan, F., and Inoue, H. (1996). "Waveform and its analysis of the 1995 Hyogoken-Nanbu earthquake (II)." *JR Earthquake Information*, 23d., Railway Technical Research Institute.

Nakamura, S. (2006). "Re-examination of Mononobe-Okabe theory of gravity retaining walls using centrifuge model tests." *Soils and Foundations*, 46(2), 135-146.

Nandkumaran, P. (1973). "Behavior of retaining walls under dynamic loads." *Ph.D. Thesis*, Roorkee University, Roorkee, India.

Nguyen, Q. V., Fatahi, B., and Hokmabadi, A, S. (2017). "Influence of size and load-bearing mechanism of piles on seismic performance of buildings considering soil-pile-structure interaction." *ASCE International Journal of Geomechanics*, Vol. 17, Issue 7.

NIST. (2012). "Soil-structure interaction for building structures." Rep. NIST Grant/Contract Rep. (GCR) 12-917-21, J. P. Stewart, ed., Gaithersburg, MD.

Niwa, S. (1960). "An experimental study of oscillating earth pressures acting on a quay wall." Proceedings, *2nd World Conference on Earthquake Engineering*, Tokyo, Japan.

Ohara, S. (1960). "Experimental studies of seismic active and seismic passive earth Pressure." Proceedings, *2nd world Conference on Earthquake Engineering*, Tokyo, Japan.

Ohtani, K., Ogawa, N., Katayama, T., and Shibata, H. (2003). "Construction of E-Defense (3-D full-scale earthquake testing facility), *2nd International Symposium on New Technologies for Urban Safety of Mega Cities in Asia*, 69–76.

Okabe, S. (1924). "General theory on earth pressure and seismic stability of retaining walls and dams." *Journal of Japanese Society of Civil Engineers*, Vol. 10, No.6, 1277–1323.

O'Rourke, T. D. and Bonneau, A. (2007). "Lifeline performance under extreme loading during earthquakes." *Earthquake Geotech. Eng.*, ed. K. D. Pitilakis., 407–432, Springer, New York, NY, 407-432.

O'Rourke, T. D., Jezerski, J. M., Olson, N. A., Bonneau, A. L., Palmer, M. C., Stewart, H. E., O'Rourke, M. J., and Abdoun, T. H. (2008). "Geotechnics of pipeline system response to earthquakes." *Proc. of 4th Decennial Geotech. Earthquake Eng. and Soil Dynamics Conf. (GEESD IV)*, ASCE, Sacramento, California.

Ostadan, F. (2004). "Seismic soil pressure for building walls- an updated approach." *11th International Conference on Soil Dynamics and Earthquake Engineering (11th ICSDEE) and*

the 3rd International Conference on Earthquake Geotechnical Engineering (3rd ICEGE), University of California, Berkeley, January.

Otsubo, M., Towhata, I., Hayashida, T., Shimura, M., Uchimura, T., Liu, B., Taeseri, D., Cauvin, B., and Rattez, H. (2016). "Shaking table tests on mitigation of liquefaction vulnerability for existing embedded lifelines." *Soils & Foundations*, 56, 348–364.

Paikowsky, S. G., Palmer, C. J., and Rolwes, L. E. (2006). "The use of tactile sensor technology for measuring soil stress distribution." *Proc. of Geo-Congress—Geotech. Eng. in Information Technology Age*, ASCE, Atlanta, GA.

Palmer, M. C., O'Rourke, T. D., Olson, N. A., Abdoun, T., Ha, D., and O'Rourke, M. J. (2009). "Tactile pressure sensors for soil–structure interaction assessment." *ASCE Journal of Geotech. and Geoenviron. Eng.*, Vol. 135, No. 11, 1638–1645.

Prakash, S., and Basavanna, B. M. (1968). "Earth pressure distribution behind retaining wall during earthquake." *Proceedings, IV World Conference on Earthquake Engineering*, Chile.

Prakash, S., and Nandkumaran, P. (1979). "Earth pressures during earthquakes." *Proceedings, 2nd U.S. National Conference on Earthquake Engineering*, 613-622, Stanford, U.S.A.

Prakash, S. and Saran, S. (1966). "Static and dynamic earth pressures behind retaining walls." *Proc., 3rd Symposium on Earthquake Eng.*, University of Roorkee, India, Vol. 1, 277-288.

Prasad, S. K., Towhata, I., Chandradhara, G. P., and Nanjundaswamy, P. (2004). "Shaking table tests in earthquake geotechnical engineering." *Current Science*, Vol. 87, No. 10, 1398-1404.

Psarropoulos, P.N., Klonaris, G. and Gazetas, G. (2005). "Seismic earth pressures on rigid and flexible retaining walls." *Soil Dynamics and Earthquake Engineering*, Elsevier, No. 25, 795-809.

Rankine, W. (1857). "On the stability of loose earth." *Philosophical Transactions of the Royal Society of London*, Vol. 147, 1857.

Richards, R., Huang, C., and Fishman, K. (1999). "Seismic earth pressure on retaining structures." *Journal of Geotechnical and Geoenvironmental Engineering*, 125(9), 771-778.

Richards, R., and Shi, X. (1994). "Seismic lateral pressures in soils with cohesion." *J. Geotech. Eng.*, 120(7), 1230–1251.

Rovithis, E. N., Parashakis, H., and Mylonakis, G. (2011). "1D harmonic response of layered inhomogeneous soil: analytical investigation." *Soil Dynamics and Earthquake Engineering*, 31(7), 879-890.

Saito, K., Yamene, K., and Koizumi, A. (2006). "A study on seismic behavior of shield tunnel including shaft in longitudinal direction." *JSCE Tunnel Engineering*, 16, 121–132.

Saran, S., and Gupta, R. P. (2003). "Seismic earth pressures behind retaining walls." *Indian Geotechnical J.*, 33(3), 195–213.

Saran, S. and Prakash, S. (1968). "Dimensionless parameters for static and dynamic earth pressures behind retaining walls." *Indian Geotechnical Journal*, Vol. 7, No. 3, 295–310.

Scott, R. F. (1973). "Earthquake-induced earth pressures on retaining walls." *Proceedings, Earthquake Engineering*, 5th World Conference, Rome, Italy, 2.

Seed, H. B., and Whitman, R. V. (1970). "Design of earth retaining structures for dynamic loads." *ASCE Specialty Conf.*, *Lateral Stresses in the Ground and Design of Earth Retaining Structures*, Cornell Univ., Ithaca, NY, 103-147.

Seed, H. B., Wong, R. T., Idriss, I. M., and Tokimatsu, K. (1986). "Moduli and damping factors for dynamic analyses of cohesionless soils." *Journal of Geotechnical Eng.*, 112(11), 1016-1032.

Selig, E. T. (1964). "A review of stress and strain measurement in soil." *Proc. of the Symposium on Soil-Structure Interaction*, University of Arizona, Tucson, Arizona.
Selig, E. T. (1980). "Soil Stress Gage Calibration," *Geotechnical Testing Journal*, Vol. 3, No. 4, 153–158.
Shamsabadi, A., Xu, S-Y, and Taciroglu, E. (2013). "A generalized log-spiral-Rankine limit equilibrium model for seismic earth pressure analysis." *Soil Dynamics Earthquake Eng.*, 49, 197-209.
Sherif, M. A., and Fang, Y. S. (1984). "Dynamic earth pressures on walls rotating about the top." *Soils and Foundations*, 24(4), 109-117.
Sherif, M. A., Ishibashi, I., and Lee, C. D. (1982). "Earth pressure against stiff retaining walls." *Journal of Geotechnical Engineering*, ASCE 108: 679-695.
Shukla, S. K., and Bathurst, R. J. (2012). "An analytical expression for the dynamic active thrust from c-φ soil backfill on retaining walls with wall friction and adhesion." *Geomechanics and Eng.*, 4(3), 209-218.
Shukla, S. K., Gupta, S. K. and Sivakugan, N. (2009). "Active earth pressure on retaining wall for c-φ soil backfill under seismic loading condition." *J. of Geotechnical and Geoenvironmental Eng.*, 135(5), 690-696.
Sitar, N., Geraili Mikola, R. G., and Candia, G. (2012). "Seismically induced lateral earth pressures on retaining structures and basement walls." *GeoCongress 2012, Geotechnical Engineering State of the Art and Practice*, Oakland, CA, 335-358.
Springman, S., Nater, P., Chikatamarla, R., and Laue, J. (2002). "Use of flexible tactile pressure sensors in geotechnical centrifuges." *Presented at the International Conf. on Physical Modeling in Geotech. Eng.*, St. Johns, NL, Canada.
Stadler, A. T. (1996). "Dynamic centrifuge testing of cantilever retaining walls." *Ph.D. Thesis*, University of Colorado at Boulder, CO.
Star, L. (2011). "Seismic vulnerability of structures: demand characteristics and field testing to evaluate soil-structure interaction effects." *PhD Thesis*, University of California, Los Angeles, Los Angeles, CA, USA.
Star, L. M., Givens, M. J., Nigbor, R. L., and Stewart, J. P. (2015). "Field testing of structure on shallow foundation to evaluate soil-structure interaction effects." *Earthquake Spectra*, Vol. 31, 2511–2534.
Steedman, R. S. (1984). "Modelling the behavior of retaining walls in earthquakes." *Ph.D. Thesis*, Engineering Department, Cambridge University, UK.
Steedman, R. S., and Zeng, X. (1990). "The influence of phase on the calculation of pseudo-static earth pressure on a retaining wall." *Geotechnique*, 40(1), 103-112.
Stewart, J. P., Taciroglu, E., Wallace, J., Lemnitzer, A., Hilson, C., Nojoumi, A., Keowen, S., Nigbor, R. L., and Salamanca, A. (2011). "Nonlinear load deflection behavior of abutment walls with Varying Height and Soil Density." *Research Report No. UCLA 2011- SGEL-01*, http://repositories.cdlib.org/cee_ucla/geotechnical/.
Stewart, J.P., and Fenves, G.L. (1998). "System identification for evaluating soil–structure interaction effects in buildings from strong motion recordings." *Earthquake Engineering and Structural Dynamics*, Volume 7, Issue 8, 869–885.
Suleiman, M. T., Ni, L., Helm, J. D., and Raich, A. (2014). "Soil-pile interaction for a small diameter pile embedded in granular soil subjected to passive loading." *Journal of Geotech. and Geoenviron. Eng.*, Vol. 140, No. 5.
Suzuki, H., Tokimatsu, K., Sato, M., and Tabata, K. (2008). "Soil-pile-structure interaction in

liquefiable ground through multi-dimensional shaking table tests using E-Defense facility." *Proceedings of the 14th World Conference on Earthquake Engineering*, 04-01-0177, October.
Talesnick, M. (2005). "Measuring soil contact pressure on a solid boundary and quantifying soil arching." *ASTM Geotech. Testing Journal*, Vol. 28, No. 2, 171-179.
Talesnick, M., Horany, H., Dancygier, A. N., and Karinski, Y. S. (2008). "Measuring soil pressure on a buried model structure for the validation of quantitative frameworks." *ASCE Journal of Geotech. and Geoenviron. Eng.*, Vol. 143, No. 6, 855-865.
Talesnick, M., Ringel, M. and Avraham, R. (2014). "Measurement of contact soil pressure in physical modeling of soil-structure interaction." ICE, *International Journal for Physical Modeling in Geotechnics*, Vol. 14, No. 1, 3-12.
Tamari, Y., and Towhata, I. (2003). "Seismic soil-structure interaction of cross sections of flexible underground structures subjected to soil liquefaction." *Soils & Foundations*, 43, 69–87.
Taylor, D. W. (1945). "Review of pressure distribution theories, Earth pressure cell investigations, and pressure distribution data." *Contract Report W22-053 eng-185*, U.S. Army Engineer Waterways Experiment Station, Vicksburg, MS.
Terzaghi, K. (1943). "Theoretical Soil Mechanics." John Wiley and Sons Inc., New York, NY.
Tory, A. C. and Sparrow, J. W. (1967). "The influence of diaphragm flexibility on the performance of an earth pressure cell." *Journal of Scientific Instruments*, 44(9), 781-785.
Tokimatsu, K., Suzuki, H., Tabata, K., and Sato, M. (2007). "Three-dimensional shaking table tests on soil-pile-structure models using E-Defense facility." *4th International Conference on Earthquake Geotechnical Engineering*.
Towhata, I., Kawamata, Y., Nakayama, M., and Yasuda, S. (2014). "E-Defense shaking test on large model of underground shafts and tunnels." *8th International Symposium on Geotechnical Aspects of Underground Construction in Soft Ground*, Seoul, South Korea.
Tsinidis, G., Rovithis, E., Pitilakis, K., and Chazelas, J. L. (2016). "Seismic response of box-type tunnels in soft soil: experimental and numerical investigation." *Tunnelling and Underground Space Technology*, 59, 199–214.
Veletsos, A. S., and Younan, A. H. (1994). "Dynamic soil pressure on rigid vertical walls." *Earthquake Engineering and Soil Dynamics*, Vol. 23, 275-301.
Veletsos, A. S., and Younan, A. H. (1997). "Dynamic response of cantilever retaining walls." *Journal of Geotechnical and Geoenvironmental Eng.*, (123) 2, 161-172.
Wagner, N., Sitar, N. (2016). "On seismic response of stiff and flexible retaining structures." *Soil Dynamics and Earthquake Engineering*, 91, 284-293.
Weiler, W. A. and Kulhawy, F. H. (1978). "Behavior of stress cells in soils." *Report 78-2*, School of Civil and Environmental Eng., Cornell University, Ithaca, New York, NY, 290p.
Weiler, W. A. and Kulhawy, F. H. (1982). "Factors affecting stress cell measurement in soil." *ASCE Journal of Geotech. Eng. Division*, Vol. 108, No. GT12, 1529-1548.
Whitman, R. V. (1991). "Seismic design of earth retaining structures." *Proceedings, 2nd International Conference on Recent Advances in Geotechnical Earthquake Engineering and Soil Dynamics*, 1767-1778, St. Louis, MO.
Wilson P. (2009). "Large scale passive force-displacement and dynamic earth pressure experiments and simulations." *Ph.D. thesis*, University of California, Sand Diego.
Wilson, P., and Elgamal, A. (2015). "Shake table lateral earth pressure testing with dense c-φ backfill." *Soil Dynamics and Earthquake Engineering*, 71, 13-26.
Wood, J. H. 1973. "Earthquake induced soil pressures on structures." *Ph.D. Thesis*, California Institute of Technology, Pasadena, CA.

Wood, J. H. (1975). “Earthquake-induced pressures on a rigid wall structure.” *Bulletin of the New Zealand National Society for Earthquake Engineering*, Vol. 8, No. 3, 175-186.

Wu, G., and Finn, W. D. L. (1999). “Seismic lateral pressures for design of rigid walls.” *Canadian Geotechnical Journal*, 36, 509–522.

Xu, S-Y, Shamsabadi, A., and Taciroglu, E. (2015). “Evaluation of active and passive seismic earth pressures considering internal friction and cohesion.” *Soil Dynamics and Earthquake Eng.*, 70, 30-47.

Yamada, S., Hyodo, M., Orense, R. P., and Dinesh, S. V. (2008). “Initial shear modulus of remolded sand-clay mixtures.” *Journal of Geotechnical and Geoenvironmental Engineering*, ASCE, 134(7), 960-974.

Yang, J., Li, J. B., and Lin, G. (2006). “A simple approach to integration of acceleration data for dynamic soil–structure interaction analysis.” *Soil Dynamics and Earthquake Eng.*, 26, 725-734.

Yashiro, K., Tachibana, N., Kojima, Y., Nonomura, M., and Asakura, T. (2007). “Model tests on behavior of tunnels under deformation of the ground upon earthquake.” *JSCE Proc. Tunnel Eng.*, 17, 195–202.

Zeghal, M., and Elgamal, A. W. (1994). “Analysis of site liquefaction using earthquake records.” *Journal of Geotechnical and Geoenvironmental Eng.,* ASCE, 120, 71–85.

Zhang, J., and Yuchuan, T. (2007). “Radiation damping of shallow foundations on nonlinear soil medium.” *4th International Conference on Earthquake Geotechnical Engineering*, Paper No. 1150.